

# **Additively manufactured permeable-dense composites and its applications in microstructured reactors**

zur Erlangung des akademischen Grades eines  
DOKTORS DER INGENIEURWISSENSCHAFTEN (DR.-ING.)

von der KIT-Fakultät für Chemieingenieurwesen und Verfahrenstechnik des  
Karlsruher Instituts für Technologie (KIT)  
genehmigte

DISSERTATION

von  
M. Sc. Dongxu Xie  
aus Heilongjiang, China

Tag der mündlichen Prüfung: 11.10.2021

Erstgutachter: Prof. Dr.-Ing. Roland Dittmeyer

Zweitgutachter: Prof. Dr. Matthias Franzreb



# Kurzfassung

Die additive Fertigung (auch als 3D-Druck bekannt) ist eine neuartige Fertigungstechnologie, mit der Objekte gemäß einem 3D-Modell aus formlosem Material schichtweise aufgebaut werden können. Das Laserstrahl-Pulverbettenschmelzen (Laser Beam Powder Bed Fusion, LB-PBF) ist ein wichtiges Verfahren der additiven Fertigung für metallische Werkstoffe, das mittlerweile in zahlreichen Branchen weit verbreitet ist. Biomedizinische Implantate mit komplexen Porenstrukturen werden häufig mittels LB-PBF hergestellt. Diese Porenstrukturen werden normalerweise in einem CAD-Modell entworfen, so dass man von geometrisch definierter Gitterstrukturporosität (GDLSP) spricht. Die Porengröße von durch GDLSP hergestellten porösen Materialien ist jedoch häufig größer als 100  $\mu\text{m}$ . Eine andere Art von 3D-gedrucktem porösem Material wird als Material mit geometrisch undefinierter Porosität (GUP) bezeichnet. Die Porenstrukturen von GUP-Materialien werden durch Variation der Parameter des LB-PBF-Verfahrens gesteuert und die Porengröße liegt im Bereich von 1  $\mu\text{m}$  bis 100  $\mu\text{m}$ . Aufgrund der im Vergleich zu GDLSP-Materialien geringeren Porengröße und der Möglichkeit in einem Arbeitsgang poröse Bereiche mit unporösen Bereichen in einem Bauteil zu verbinden besteht ein zunehmendes Interesse an GUP-Materialien.

In dieser Dissertation wurde die Beziehung zwischen den Parametern des LB-PBF-Verfahrens wie Schraffurabstand, Laserfokusdurchmesser und Scanstrategie und den resultierenden porösen Struktureigenschaften systematisch untersucht. Die experimentellen Ergebnisse zeigen, dass das GUP-Material zwei Arten von Poren enthält. Die Poren innerhalb der Laserspuren sind größer und instabil. Die Poren zwischen den Laserspuren können leicht durch die Laserparameter gesteuert werden. Wenn der Schraffurabstand zunimmt, nehmen Porosität, Porengröße, Permeabilität und Oberflächenrauigkeit zu. Wenn der Laserfokusdurchmesser zunimmt, ändert sich die Porosität nicht wesentlich, die Rauigkeit nimmt zu, Porengröße und Permeabilität nehmen ab. Der entscheidende Punkt ist das Balling-Phänomen. Eine größerer Laserfokusdurchmesser führt zu mehr Pulver, das auf der porösen Oberfläche versintert wird. Die Wirkung verschiedener Scanstrategien, einschließlich unidirektionaler Scanvektoren (USV), Rotations-Scanvektoren (RSV)

und Vier-Richtungs-Scanvektoren (FDSV) auf die Oberflächenmorphologie wurde auf rohrförmigen Proben untersucht.

Basierend auf dem 3D-gedruckten porösen Material wurden porös-dichte Verbundbauteile gedruckt. Ein Testmodul auf dieser Basis wurde für die nachfolgende Beschichtung mit einer permeablen keramischen Zwischenschicht vorbereitet. Ein 2 mm dickes Testmodul wurde dazu mit einer Fräsmaschine geglättet. Die Rauigkeit des geglätteten Testmoduls beträgt  $1,36 \mu\text{m}$ , was das Potenzial als neuartiges Membransubstrat zeigt. Ferner wurden poröse Membransubstratplatten (PMS-Platten) und poröse Membransubstratrohre (PMS-Rohre) für Mikroreaktoren hergestellt.

In der Forschung lässt sich ein zunehmendes Interesse an 3D-gedruckten mikrostrukturierten Apparaten für verfahrenstechnische Anwendungen beobachten. Für die Herstellung von 3D-gedruckten Mikroreaktoren wurde eine  $90^\circ$  - Designstrategie und eine  $45^\circ$  - Druckstrategie vorgeschlagen. Mikroreaktoren mit Temperatursperre und internen Kanälen wurden als beispielhafte Anwendung konzipiert und gedruckt.

Parts of this dissertation have already been published in Xie, D., & Dittmeyer, R. (2021). Correlations of laser scanning parameters and porous structure properties of permeable materials made by laser-beam powder-bed fusion. *Additive Manufacturing*, 102261 (DOI: 10.1016/j.addma.2021.102261).

## Abstract

Additive manufacturing (also known as 3D printing) is a novel manufacturing technology to make objects from a shapeless material according to a 3D model by a layer-by-layer manufacturing method. Laser-beam powder bed fusion (LB-PBF) is an important metal additive manufacturing method which is widely used in numerous industries. Biomedical implants with complex pore structures are often made by LB-PBF. Their pore structure is usually defined by a computer-aided design (CAD) model; the resulting materials are therefore named geometrically defined lattice structure porosity (GDLSP) materials. However, the pore size of GDLSP-materials is often larger than 100  $\mu\text{m}$ . Another kind of additively manufactured porous material are geometrically undefined porosity (GUP) materials. The pore structure of GUP-materials is controlled by the LB-PBF scanning parameters, and their pore size ranges from 1  $\mu\text{m}$  to 100  $\mu\text{m}$ . Due to the smaller pore size compared to GDLSP and the opportunity to create permeable-dense composites, there has been an increasing interest in GUP materials, recently.

In this dissertation, the relation between the scanning parameters including hatch distance, laser spot size and scan strategy and the resulting properties of the permeable structure was systematically studied. The experimental results show that there are two kinds of pores in GUP materials. The pores within the laser tracks have a larger size and are unstable. The pores between the laser tracks are easily controlled by the laser parameters. When the hatch distance is increased, the porosity, pore size, permeability and surface roughness all increase. When the laser spot size is increased, the porosity has no significant changes, the roughness is increasing and pore size and permeability are both decreasing. The key point is the balling phenomenon. A larger laser spot size leads to more powder sintered on the permeable surface. The effect of different scan strategies including unidirectional scan vectors (USV), rotation scan vectors (RSV) and four direction scan vectors (FDSV) on the surface morphology was studied on tubular samples.

Based on the additively manufactured porous material, permeable-dense composites were printed. A test module made on that basis was prepared for coating with a permeable ceramic interlayer. A 2 mm thick test module was smoothed by high precision milling. The roughness of the smoothed test module is 1.36  $\mu\text{m}$  which shows the potential as novel membrane substrate. Further, permeable membrane

substrate plates (PMS plates) and permeable membrane substrate pipes (PMS pipes) were prepared for use in microreactors.

Recently, researchers have shown increasing interest in additively manufactured devices for process engineering applications. A 90° design strategy and a 45° printing strategy were proposed for additively manufactured microreactors. Microreactors with temperature barrier module and internal channels were designed and printed as an exemplary application.

# Contents

Kurzfassung .....	i
Abstract.....	iv
Abbreviations .....	viii
1. Introduction .....	1
1.1 Motivation .....	1
1.2 State of the art .....	3
1.2.2 Metal additive manufacturing .....	13
1.2.3 Microstructured reactors and other process units .....	19
1.3 Objectives of this dissertation .....	23
2. Additively manufactured permeable metal .....	25
2.1 Materials and methods .....	25
2.1.1 System and material .....	25
2.1.2 Determination of porosity and pore size distribution .....	26
2.1.3 Determination of permeability .....	28
2.1.4 Sand blasting .....	29
2.1.5 Morphology.....	29
2.2 Scan strategy.....	30
2.2.1 Scan vector rotation .....	30
2.2.2 Scan vectors shift position between individual layers .....	31
2.2.3 Unidirectional scan vectors in different direction.....	32
2.3 Laser parameter .....	36
2.3.1 Laser spot size .....	36
2.3.2 Hatch distance .....	41
2.4 Permeable-dense composite .....	44
2.5 Summary and Conclusion .....	46
3. Additively manufactured permeable metal parts with curved surfaces.....	47
3.1 System and material .....	47
3.2 Scan strategy.....	48
3.2.1 Permeable tubes printed by unidirectional scan vectors (USV). .....	48
3.2.2 Permeable tubes printed by rotation scan vectors (RSV). .....	50
3.2.3 Permeable tubes printed by four direction scan vectors (FDSV). .....	55

3.3 Laser parameters .....	60
3.3.1 Hatch distance .....	60
3.3.2 Laser spot size .....	61
3.4 Permeable-dense composite with bending surface .....	62
3.5 Summary and Conclusion .....	63
4. Preliminary research on additively manufactured components for a microstructured membrane steam reformer .....	65
4.1 Palladium membrane substrate .....	65
4.1.1 Test module preparation .....	65
4.1.2 Ceramic coating .....	67
4.1.3 Palladium membrane substrate plate (PMS plate) .....	71
4.1.4 Tubular palladium membrane substrates (PMS pipe) .....	79
4.2 Additively manufactured microstructured reactor .....	83
4.2.1 Additively manufactured micro channels .....	83
4.2.2 Additively manufactured microstructured reactor design .....	86
4.3 Summary and Conclusion .....	91
5. Summary and Outlook .....	93
References .....	95
Appendix .....	114
List of figures .....	116
List of tables .....	120

# Abbreviations

LB-PBF	Laser-beam powder bed fusion
GDLSP	Geometrically defined lattice structure porosity
GUP	Geometrically undefined porosity
SEM	Scanning electron microscopy
SCR	Self-catalytic reactors
USV	Unidirectional scan vectors
RSV	Rotation scan vectors
FDSV	Four direction scan vectors
FDCSV	Four direction vectors and connection scan vectors
FDOSV	Four direction overlap scan vectors
IMVT	Institute for Micro Process Engineering
KIT	Karlsruhe Institute of Technology
CAD	Computer-aided design
IUPAC	International Union of Pure and Applied Chemistry
CNC	Computerized Numerical Control
BJ	Binder jetting
PBF	Powder bed fusion
LOM	Laminated object manufacturing
DED	Direct energy deposition
EBM	Electron beam melting
SLS	Selective laser sintering
SLM	Selective laser melting
EBF <sup>3</sup>	Electron beam freeform fabrication
LENS	Laser engineered net shaping

---

LC	Laser consolidation
DLF	Directed light fabrication
WAAM	Wire and arc additive manufacturing
3DP	Powder bed and inkjet 3D printing
UC	Ultrasonic consolidation



# 1. Introduction

## 1.1 Motivation

Porous metallic materials have the characteristics of large specific surface area, low density and good permeability [1]. Due to the features of porous metallic materials, porous metallic materials are widely used as wear-resistant tools [2], biomedical implants [3], vibration reduction components [4]. In process engineering applications, porous metals often need to be welded to a dense body. E.g., Bai et al. presented heat sinks with microchannels, and the copper particles were coated by solid-state sintering on the microchannels [5]. Oak Ridge National Laboratory presented a metallic filter for particulates and water purification. Both ends of a porous tube were composed of solid material by laser welding [6]. The high temperature during the welding process leads to residual stress and may cause weld distortion [7]. Moreover, the weld seam may influence the function of the porous material. Boeltken et al. presented a new method of palladium membrane coating on planar porous substrates. Their palladium membrane module was composed of a metallic porous substrate, a ceramic diffusion barrier layer and a palladium membrane [8]. The porous substrate was welded to a dense frame for reliable sealing and easy assembly. However, the weld seam between the porous substrate and the dense frame is prone to the formation of defects in the ceramic layer and the palladium membrane and to low adhesion of coatings [9]. In view of this, permeable-dense composites made by LB-PBF could be a feasible solution. With the layer by layer working principle of LB-PBF, permeable-dense composites could be printed in one step without additional welding steps [10]. A smooth transition from porous regions to dense regions can be expected. However, the properties of additively manufactured porous materials determine the application of permeable-dense composites.

Additively manufactured porous materials with CAD-designed porous structures are named geometrically defined lattice structure porosity (GDLSP) materials. The pore size of GDLSP materials is generally larger than 100  $\mu\text{m}$  [11]; GDLSP materials are widely used as orthopaedic implants [12][13]. Another type of additively manufactured porous material is called geometrically undefined porosity (GUP) materials. The porosity and pore size of GUP materials are determined by the LB-

PBF laser parameters and scan strategies [14]. The pore size range of GUP materials is generally from 1  $\mu\text{m}$  to 100  $\mu\text{m}$  [11]. Recently, GUP has been attracting increasing attention because of the smaller pore size. Cherry et al. studied the relation between laser energy density and porosity [15]. Li et al. studied the relation between scan speed and porosity [16]. Yet, most studies in the field of GUP have only focused on laser energy density and porosity. GUP materials have not yet been extensively studied, in particular not regarding the possibility of fabricating permeable-dense composites. Therefore, in this study the relation between pore structure and surface properties and the LB-PBF laser parameters and scan strategy were studied in detail and systematically.

## 1.2 State of the art

### 1.2.1 Fabrication and applications of macro porous metals

The International Union of Pure and Applied Chemistry (IUPAC) classifies porous materials into microporous, mesoporous and macro porous materials by the pore diameter. The pore diameter of a microporous material is smaller than 2 nm, the pore diameter of a mesoporous material is between 2 nm and 50 nm, and the pore diameter of a macro porous material is larger than 50 nm [17]. The pore diameter of additively manufactured porous materials is highly related to the resolution of the LB-PBF machine used which depends on the particle size of the powder, the layer thickness and the laser beam diameter [18]. For most of the commercial LB-PBF systems, the resolution is of similar level as the laser beam diameter [19]. A ReaLizer SLM 125 LB-PBF machine was used in this study, and the diameter of the laser beam here is between 30  $\mu\text{m}$  and 60  $\mu\text{m}$ , which is obviously much larger than 50 nm. Therefore, this study focuses on macro porous materials rather than microporous or mesoporous materials. In order to evaluate the prospects of 3D printing of porous materials, it is important to understand the characteristics of different processes of porous metal preparation.

As shown in Fig. 1.1, Banhart classified porous metal preparation methods into four categories according to the state of the metal process in [20]. Some typical fabrication technologies and applications of macro porous metals are discussed in this section.

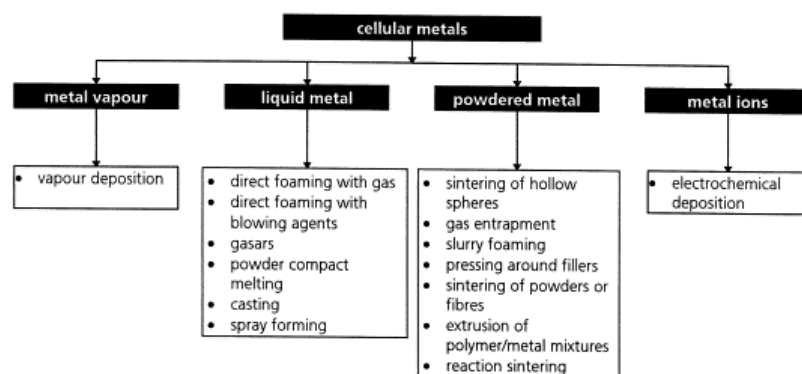


Figure. 1.1. Fabrication technologies of macro porous metals [20].

#### 1.2.1.1 Direct foaming of metals

The liquid processing route introduces porosity to the molten metal by foaming. The methods of foaming molten metal can be classified into several groups.

The first one is direct foaming of porous metal. Usually, there are two methods to foam the porous metal directly. One is the molten metal is foamed by gas injection from an external source. The other method is that metal is foamed by admixing a blowing agent into the liquid metal.

Foaming by gas injection is widely used in porous aluminum and aluminum alloys [21]. The schematic of foaming by gas injection is shown in fig. 1.2. Specially designed rotating impellers or vibrating nozzles are used to inject gas (gas, nitrogen, argon) into the molten metal. Due to the high buoyancy force in high density molten metals, the gas bubbles tend to rise quickly to the surface. To hamper the rise of bubbles, fine ceramic powders or alloying elements like SiC, Al<sub>2</sub>O<sub>3</sub>, MgO are added to the molten metal to increase the viscosity of the liquid [22]. To keep the high viscosity, the temperature of the foaming process is chosen close to the melting point of the metal. With cooling down by the injected gas, the bubbles are trapped in the molten metal which solidifies to yield a porous metal [23].

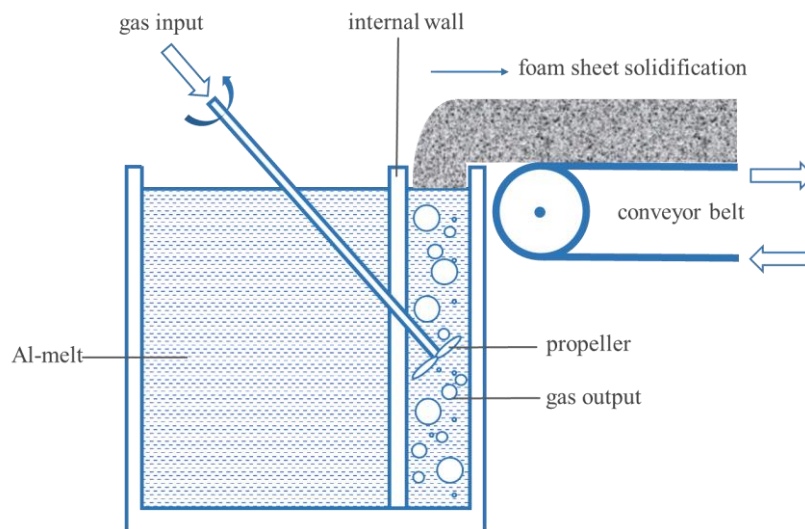


Figure. 1.2. Schematic of foaming by gas injection [24].

Foaming with blowing agents is another direct foaming method. Metal powder and blowing agent are mixed and densified to a precursor [25]. During the heating process of the precursor, the blowing agent builds an internal pressure for the porous structure formation [26]. In the foaming process, the melting point of the metal should match the decomposition temperature range of the blowing agent [27]. If the decomposition temperature range is lower than the melting point of the metal, the solid metal will yield cracks. If the decomposition temperature range is higher than melting point, the viscosity of the molten metal is too low to generate stable porous

structures [27]. Due to the low melting point, aluminum and zinc alloys are suitable for foaming with blowing agents and  $\text{TiH}_2$ ,  $\text{ZrH}_2$ , Mg were used as blowing agents for these alloys [28].

#### 1.2.1.2 Solid–gas eutectic solidification

Solid-gas eutectic solidification is another method to introduce porosity to the molten metal. These materials are also called “gasars” which means “gas-reinforced” [29]. Generally, the molten phase of a metal has a higher gas solubility than the solid phase. During the solidification of the metal, the solubility decreases and shrinkage phenomena cause pore formation. High porosity causes a decrease in the mechanical properties. One of the most effective ways to reduce the pore content is to remove as much gas as possible from the molten metal. However, gas supersaturation in the molten metal is a precondition of solid-gas eutectic solidification [29]. The metals are molten in hydrogen atmosphere under high pressure (up to 50 atm) to obtain a homogenous hydrogen-metal mixture. After lowering the temperature, the melt will eventually undergo an eutectic transformation into a solid gas two-phase system [30]. A schematic of an apparatus for fabrication of gasars can be seen in Fig. 1.3.

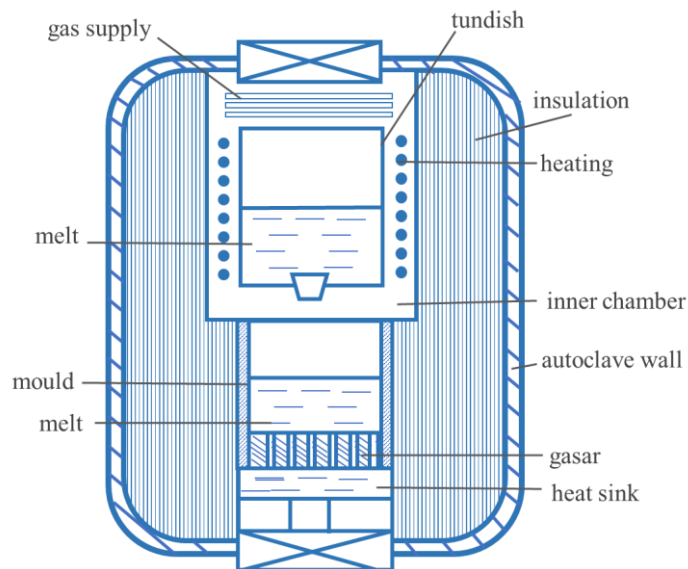


Figure. 1.3. Schematic of an apparatus for fabrication of gasars [31].

#### 1.2.1.3 Sintering of metal powders and fibers

Sintering of metal powders is a kind of solid state processing of porous metals. Liquid state processing requires a metal of relatively low melting point like aluminum and aluminum alloys while many high melting point metals like superalloys, stainless steel, or titanium can be sintered to porous metals [32]. The sintering process only requires heat to drive, and basic heat treatment equipment is

enough for sintering [33]. The bonding of particles can be improved by compacting the powder and increasing the sintering temperature [34]. However, compaction results in a loss of total porosity [35].

#### 1.2.1.4 Sacrificial (fugitive) template

In the sintering of metal powders a sacrificial template is a way to increase porosity. As shown in fig. 1.4, metal powder can be added to the sacrificial template after or during the sacrificial template foaming process.

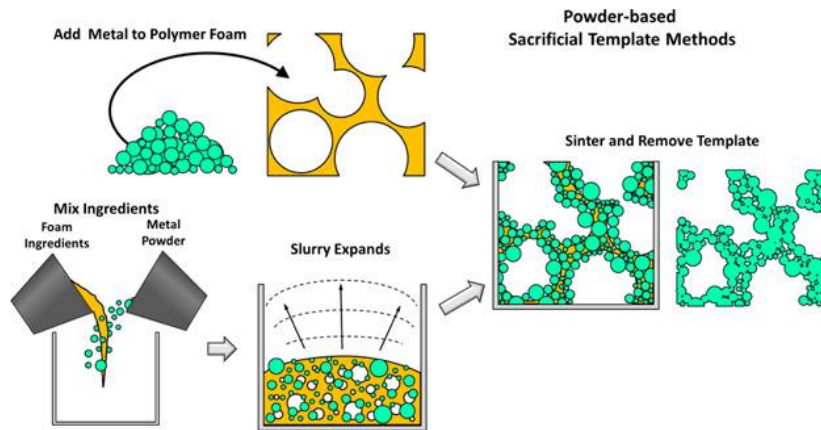


Figure. 1.4 Porous sintered metals based on a sacrificial template [36].

After the powders are placed on or around the scaffold template material e.g., polyurethane, the scaffold template material is removed by a liquid solvent [37,38] or during sintering [39,40]. To make the polymer surface become “tracky”, Kupp et al. immersed the polymer template in a mixture of approximately 2-5 wt % PVA or PEG in alcohol [41]. Then they covered the polymer template by adding the metal powder. Excess powder was shaken out, and the polymer scaffold template was removed by sintering.

Another method of coating metal powder on a scaffold template is vapor or ion deposition. Paserin et al. heated Ni tetra carbonyl ( $\text{Ni}(\text{CO})_4$ ) to a modest temperature in vacuum. Then the Ni carbonyl vaporizes and decomposes to yield a Ni coating on the scaffold template [42].

#### 1.2.1.5 Space holder

As shown in fig. 1.5, the space holder technique introduces porosity by mixing the metal powder with a second phase, e.g., NaCl [43,44]. After compaction or sintering, the metal matrix has sufficient strength to maintain the shape. Then the second phase is removed by dissolution [45] or vaporization [46]. This technique is very

simple. But depending on the materials and removal conditions, the dissolution may take hours, days [44], or even weeks [45].

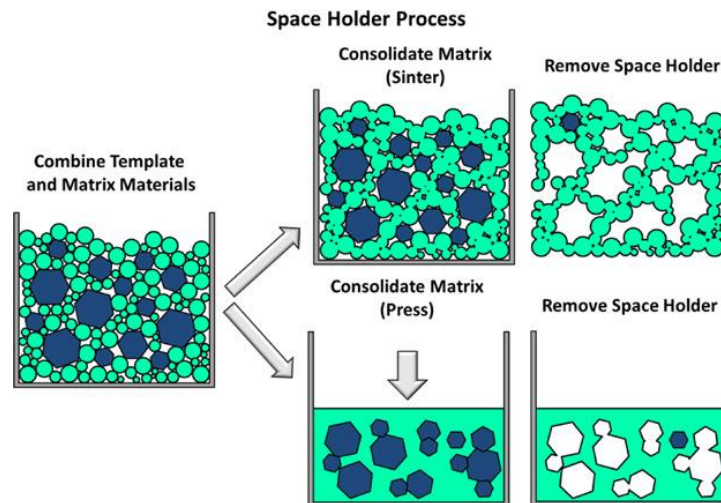


Figure. 1.5. Illustration of the space holder process to fabricate porous metals [36].

### 1.2.1.6 Additive manufacturing

Additive manufacturing, also called 3D printing, is a novel technology to manufacture components by allowing direct replication of the computer-aided design (CAD) model [47]. Different from other porous metal fabrication technologies, the geometry of components can be printed directly by additive manufacturing. However, the additive manufacturing metal equipment requires a lot of investment and the printing process is often time consuming compared to other porous metal fabrication technologies. This limits the application of additive manufacturing. Fig. 1.6 shows the categories of additive manufacturing. Porous materials manufactured by additive manufacturing will be discussed in detail in chapter 1.2.2.

Additive Manufacturing (AM) Processes							
Process	Laser Based AM Processes			Extrusion Thermal	Material Jetting	Material Adhesion	Electron Beam
	Laser Melting	Laser Polymerization					
Process Schematic							
Name Material	SLS	DMD	SLA	FDM	3DP	LOM	EBM
	SLM	LENS	SGC	Robocasting	IJP	SFP	
	DMLS	SLC	LTP		MJM		
		LPD	BIS		BPM		
			HIS		Thermojet		
Bulk Material Type							
	Powder	Liquid	Solid				

Figure. 1.6. Classification of additive manufacturing processes [48].

### 1.2.1.7 Potential applications of additively manufactured permeable-dense composite

Table. 1.1 shows the fabrication technologies, properties, and applications of

different porous metal alloys. The applications of porous metals depend on many conditions. The most important properties are listed below [20]:

**Morphology:** open porosity, closed porosity, pore size and pore size distribution, and specific surface area.

**Metallurgy:** microstructure of porous metals or alloys.

**Processing:** possibilities for shaping porous metals and for fabricating connection structures between the porous metal and conventional sheets or profiles.

**Economy:** cost and ability for large volume production.

Table 1.1 Properties and applications of porous metals [36]

Metal	Melting Point (°C)	Yield Strength (MPa)	Common Method(s) of Foaming	Typical Foam Application(s)	Examples
Aluminum	660	34	Liquid State	Lightweight Structural	[49–52]
Copper	1085	69	Solid State – Electrodeposition, Powder	Thermal, Electrical	[53–56]
Gold	1064	-	Solid State – Dealloying, Electrodeposition	Catalysis, Actuators	[57–60]
Iron	1538	210	Solid State – Powder	High-Strength Structural	[61–65]
316L SS	1375	205-310			
Magnesium	649	97-150	Solid State – Powder Liquid State – Controlled Atmosphere	Ultralight Structural, Bioactive	[66–71]
Nickel	1455	148	Solid State – CVD, Electrodeposition	Electrodes, Biomedical, Superalloys	[43,72–76]
Titanium	1668	170	Solid State – Gas Entrapment, Powder, Additive	Lightweight Structural, Biomedical	[77–83]
Ti-6Al-4V	1604	880			
Zinc	420	-	Liquid State – Alporas	Solid State – Electrodeposition	[84–87]

In many claimed applications, porous metals have better properties than their competitors [20]. However, often the price of a component is the key point for successful industrialization [88]. For additively manufactured porous metals, the investment and low printing efficiency of metal 3D printers undoubtedly push up the cost. Therefore, the use of additively manufactured metallic porous materials often focuses on high-demanding applications such as orthopaedic implants [36]. The pore structure of additively manufactured orthopaedic implants is often of GDLSP-type. Usually, the pore size of GDLSP is larger than  $100\ \mu\text{m}$ . The additively manufactured metallic porous material with a pore size lower  $100\ \mu\text{m}$  is often of GUP-type. Different with GDLSP, the porosity and pore size of GUP is determined by laser parameters rather than CAD model. Therefore, the pore structure of GUP is not a determined geometry like GDLSP. Compared with GDLSP, the pore structure of GUP is more like cellular metal. This feature of GUP must be considered for different applications. As shown in fig. 1.7, GDLSP-type materials are widely used for artificial bones manufacturing.

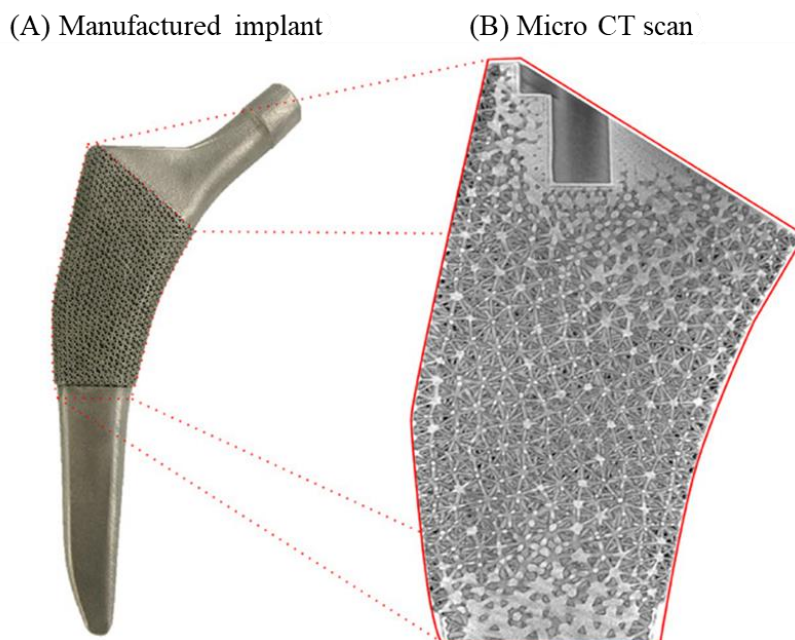


Figure 1.7. (a) Implants printed by LB-PBF; (b) Micro CT assessment of the implant [89].

However, if the application requires the pore size of a material to be smaller than about  $100\ \mu\text{m}$ , GDLSP-type materials are not applicable anymore [90]. Moreover, by controlling the printing parameters, parts with GUP-type regions and dense regions can be printed in one step by LB-PBF. Such permeable-dense composite materials shows great potential in process engineering. Generally, the porosity of a

GUP-type material is controlled by the laser energy density. However, the dimensions of parts with GUP-type structure are limited. Abele et al. presented a porous thin wall by laser energy controlling. When the wall got thicker than 175  $\mu\text{m}$ , it was no longer gas permeable [14]. Hence the relation between the laser parameters, i.e., hatch distance, laser spot size, and scan strategy and the resulting pore structure needs further study.

Recently, researchers have shown an increased interest in additively manufactured molding tooling [91,92]. On the one hand, additive manufacturing can help to reduce the time-to-market. On the other hand additively manufactured injection molds with cooling channels parallel to the surface could increase the cooling performance [93]. As shown in fig. 1.8, Antonio et al. presented die-casting dies with conformal cooling channels for zinc alloy casting [94]. The upper part includes the cores, and the conformal cooling channels were printed by LB-PBF. The lower part includes the inlet and outlet of the coolant which was created after the printing by a Computerized Numerical Control (CNC) machine.



Figure 1.8. Die-casting dies with conformal cooling channels manufactured by a LB-PBF printer and a CNC machine [94].

Moreover, injection molds made of breathable mold steel has benefits such as decreased injection pressure, reduced gloss levels, scrap and reject rates [95]. Breathable mould steel requires a pore size of the steel smaller than 80  $\mu\text{m}$  diameter. However, the smallest pore size of GDLSP-type porous metals is 100  $\mu\text{m}$  to 200  $\mu\text{m}$ , which is not suitable for breathable mould steel [11]. Zeng et al. introduced the foaming agent  $\text{CrN}_x$  (3% and 5%) to the AISI 420 steel powder to manufacture breathable molding tooling steel. The  $\text{CrN}_x$  is composed of CrN and  $\text{Cr}_2\text{N}$ . The chemical compositions of  $\text{CrN}_x$  is 0.2% O, 14.6% N and 85.2% Cr (wt. %) [96]. Fig. 1.9 shows the cross section and pore size distribution of breathable steel. However, dense materials cannot be printed by metal powder with a foaming agent. Therefore, conformal cooling channels in molds made from breathable mould steel are not possible with this method.

Additively manufactured permeable-dense composites could offer a potential method for manufacturing of advanced tools for molding manufacturing. The benefits of additively manufactured permeable-dense composites are listed below:

**Morphology:** the pore size range of permeable-dense composites is lower than 100  $\mu\text{m}$  which fits the requirement of breathable steel molding tooling.

**Processing:** the geometry of additively manufactured porous materials can be designed directly by CAD model.

**Composite structure:** the dense and porous structures of permeable-dense composites can be combined flexibly.

Based on the advantages of permeable-dense composites, additively manufactured breathable steel molding tooling with conformal cooling channels could be expected in the future.

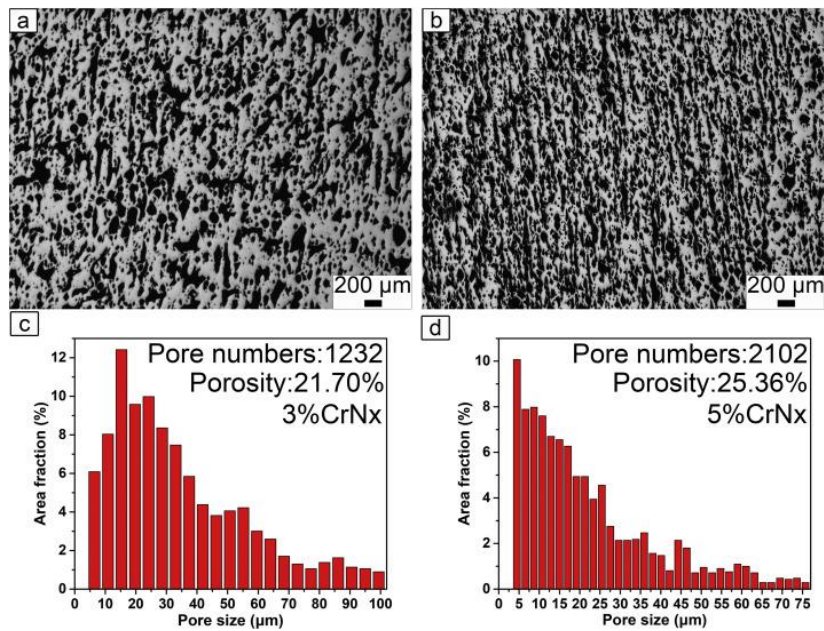


Figure 1.9. Optical microscopy graphs and pore size distribution of breathable steel [96].

Bi-functional or even multifunctional applications are another way to increase the benefits at given costs of a porous material [20,97]. Today, renewable energy plays a more and more important role in our daily life. To reduce the emission of CO<sub>2</sub> in transport, battery electric vehicles are attracting increasing interest [98]. For such vehicles, due to the high weight of the battery, lightweight structures become mandatory [99]. In addition, safety is another important factor. In case of reduced size, a lightweight but still effective collision protection system is required. Fig. 1.10 shows three application fields of porous metals in the automotive industry. Multifunctional applications are ideal but difficult to establish. However, additively manufactured permeable-dense composites present novel properties, and multifunctional applications can be expected. E.g., Siemens presented a rotating component with porous structures to counteract vibrations, which is clearly a typical multifunctional application [100].

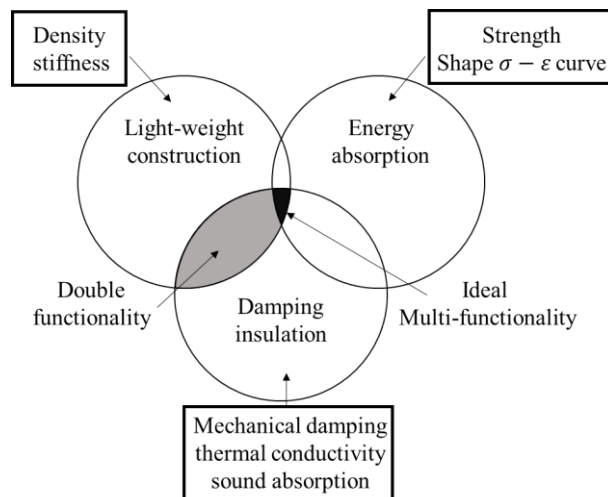


Figure 1.10. Application fields of porous metals in the automotive industry [20].

### 1.2.2 Metal additive manufacturing

Additive manufacturing is an important and rapidly emerging manufacturing technology. With layer-by-layer deposition of metallic material, metallic components with complex geometry can be easily manufactured [101]. As shown in table. 1.2, according to the working principle, metal additive manufacturing includes binder jetting (BJ), powder bed fusion (PBF), laminated object manufacturing (LOM) and direct energy deposition (DED).

Table. 1.2 Classification of metal additive manufacturing methods [102].

Classification	Terminologies	Ref.	Material
Powder bed fusion	Direct metal laser sintering (DMLS)	[103]	Metal powder
	Electron beam melting (EBM)	[104]	
	Selective laser sintering (SLS)	[105]	
	Selective laser melting (SLM)	[106]	
Directed energy deposition	Electron beam freeform fabrication (EBF <sup>3</sup> )	[107]	Metal powder, Metal wire
	Laser engineered net shaping (LENS)	[108]	
	Laser consolidation (LC)	[109]	
	Directed light fabrication (DLF)	[110]	
	Wire and arc additive manufacturing (WAAM)	[111]	
Binder jetting	Powder bed and inkjet 3D printing (3DP)	[112]	Metal powder
Sheet lamination	Laminated object manufacturing (LOM)	[113]	Metal laminate, metal foil
	Ultrasonic consolidation (UC)	[114]	

### 1.2.2.1 Laminated object manufacturing (LOM)

Different from other metal additive manufacturing technologies, in LOM the raw material is metal sheets rather than metal powder or wire [115]. According to the sliced CAD model data, metal sheets are cut by a laser beam or on a CNC machine [116]. Then the sheets are stacked and bonded orderly by alloys of low melting points [117,118], or bolting then arc welding [119], or diffusion bonding [120,121]. Solid-state diffusion bonding is used to produce integral parts with mechanical properties comparable to bulk materials. The diffusion process performed at 80-90% of the melting range of the material calculated in Kelvin, and is always accompanied by deformation [122,123]. Considering the strength and efficiency of the component, metal sheets of 0.2 to 0.5 mm thickness are often used in the LOM process. Fig. 1.11 shows a reactor prepared by IMVT for methanation of CO/CO<sub>2</sub> mixtures [124]. The reactor body is produced by the diffusion bonding of thin metal sheets. Although the walls between the different compartments are very thin, it still has high mechanical strength [125].

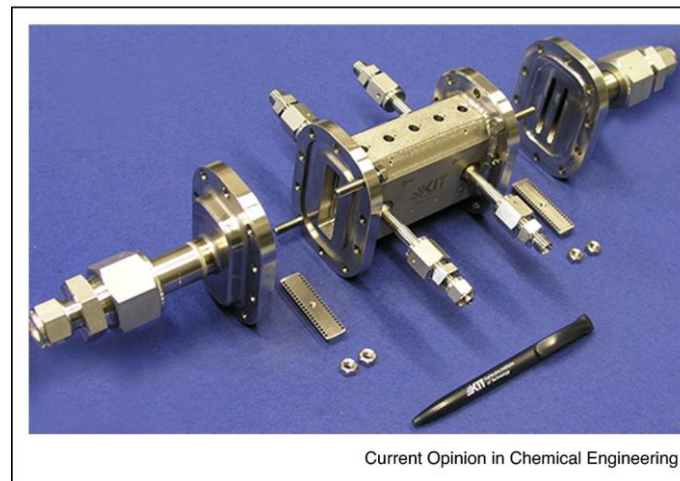


Figure 1.11. Reactor manufactured for methanation of CO/CO<sub>2</sub> mixtures [124].

### 1.2.2.2 Binder jetting (BJ)

Binder jetting is a powder bed-based fabrication process developed at the Massachusetts Institute of Technology (MIT) in the early 1990s [126]. Nowadays, BJ has successfully processed a variety of materials, including polymers, metals and ceramics [127]. Due to the advantages of high densities metallic components similar to LB-PBF and ability to produce components without support structure with a relatively high build speed than LB-PBF, BJ attracting more attention [128]. The print speed of a printer with a 100-nozzle print head is approximately 200 cm<sup>3</sup>/min. Fig. 1.12 shows the general principle binder jetting process. The CAD model is

sliced to sheets with a certain thickness. For each layer, a layer of powder is spread by parallel deposit/powder bed or hopper recoater [129], then the ink print head deposits liquid droplets on the powder bed to create 2D slices. When one layer is printed, the powder bed is lowered by a predefined height, and new powder is deposited by a roller or wiper for the printing of the next layer. After the printing process, the excess powder on the printed part is removed, e.g., by compressed air gas. Then the printed part is moved into heat treatment equipment for de-binding and sintering. According to the sintering temperature, totally dense or porous 316 stainless steel components could be achieved [17]. However, permeable-dense composites are difficult to be made this way. Generally, due to the lack of compaction force during the printing process, the powder bulk density of the green part is low [130]. Therefore, obtaining high-density parts is challenging and means that the parts will shrink greatly during the post-sintering process. Therefore, developing printing and post-processing methods that maximize part performance remains a challenge [127]. The shrinkage during post-sintering must be considered in part design.

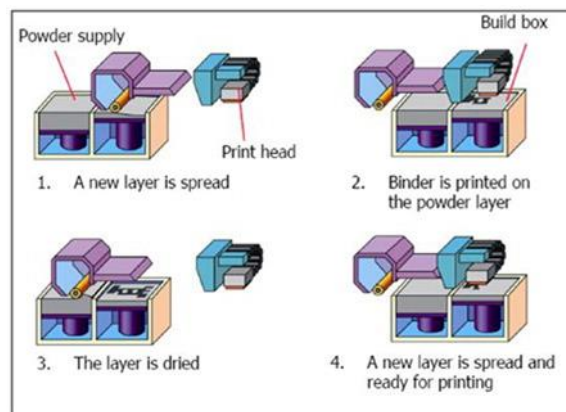


Figure 1.12. Schematic of binder jetting process [17].

### 1.2.2.3 Selective laser sintering and melting (SLS/SLM)

SLS/SLM and BJ are applicable to powder-based material systems. Typically, nozzles are used in BJ for binder spraying to bind the powder in a solid part. In SLS, a laser beam is used to heat and fuse the powder. The laser power ranges from 7 W (for plastic) to 200 W [131,132]. SLM is similar to SLS. In the SLM process, the powder is melted to form a part rather than sintered. Therefore, the laser beam power is usually higher than SLS (approximately 400 W) [133]. The high precision

and surface quality of SLS and SLM make them widely used in many areas e.g., dental implants. However the printing process is relatively slow (5-20 cm<sup>3</sup>/h) and the non-uniform thermal field distribution may cause the deformation and cracks on the components [134,135].

As shown in fig. 1.13, similar with binder jetting, the CAD model in the SLS/SLM process is sliced with predefined thickness. The 2D slices are created by local melting of powder particles with the laser beam rather than by fixing powder particles with liquid binder droplets. After each layer is printed, the powder bed controlled by an elevator is lowered by a certain height, then new powder is deposited by a roller or wiper for the printing of the next layer [48]. During the printing process, the chamber of the SLS/SLM machine is filled with inert gas (argon or nitrogen) to prevent oxidation.

According to the raw material, SLS can be further classified into direct selective laser sintering and indirect laser sintering process. In indirect laser sintering process, the metal powder is immersed in a photopolymer resin to coat polymer binder on the surface of the metal particles. Then the laser beam sinters the polymer binder to create the component. After the printing process, a thermal treatment is required to reduce the porosity and increase the strength. In direct selective laser sintering, there is no polymer binder. The metal powder is sintered directly by a high-power laser beam [136,137]. In direct SLS, the porosity of a printed part is highly related to the hatch distance, local powder bed temperature, layer thickness and laser power. The laser energy density and porosity are inversely proportional [138]. The volumetric laser energy density is defined as:

$$Ev = \frac{P}{Vs \cdot hd \cdot S} \quad (1)$$

Where  $Ev$  is volumetric energy density,  $P$  is the laser power,  $Vs$  is the scan speed,  $hd$  is the hatch distance, and  $S$  is the layer thickness [12]. Low laser power, high scan speed, high hatching distance and layer thickness lead to partial melting of the metal powder and cause porosity of the printed part. The volumetric energy density is a combined value to predict the porosity in direct SLS/SLM [14].

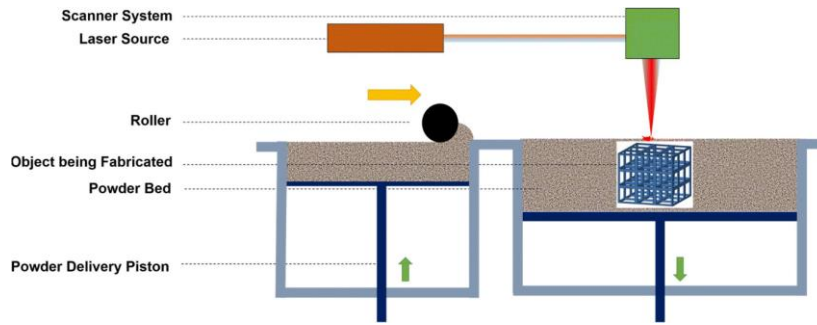


Figure 1.13. Schematic of the SLS/SLM process [139].

#### 1.2.2.4 Direct energy deposition (DED)

Direct energy deposition (DED) is also known as laser metal deposition (LMD), laser engineered net shaping (LENS) or laser cladding [140–145]. Different from BJ, SLS and SLM, there is no powder bed in the DED processes. According to the material fed, DED could be classified into powder feeding and wire feeding types [146,147]. Fig. 1.14 shows the schematic of laser metal deposition. The powder supplied by a powder feeding nozzle is fully melted by the laser beam. The completely dense printed part is printed without any post treatment. Based on this working principle, LMD can build a material layer directly on the surface of a 3D component along an arbitrary trajectory [148]. Therefore, LMD can be used for applications of repair and wear/corrosion protection [149].

The melting process of wire type DED systems is contributed either by a laser beam, an arc, or an electron beam [150,151]. The building speed of wire type DED machines is significantly higher than for powder type DED systems. The maximum building speed of a powder type DED process is around 70 cm<sup>3</sup>/h, while the maximum building speed of a wire type DED process is around 2500 cm<sup>3</sup>/h [135,152]. More information on the comparison of metal additive manufacturing methods are provided in table. 1.3.

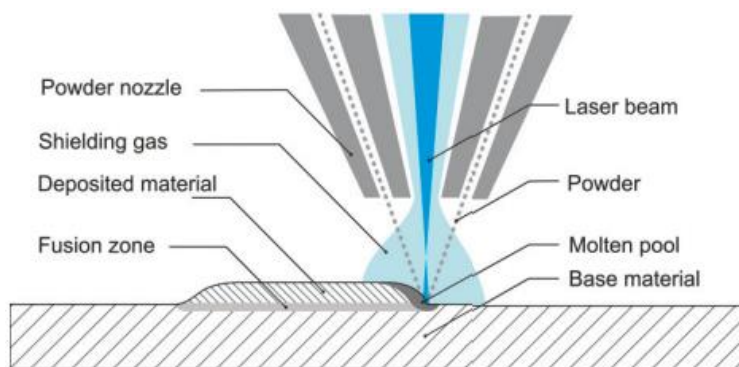


Figure 1.14. Schematic of powder-based laser metal deposition [153].

Table. 1.3 Comparisons of different metal additive manufacturing methods [102]

Process	SLM	SLS	DED (powder)	DED (wire)
Additive materials	Powder			Wire
Layer thickness ( $\mu\text{m}$ )	20–100	75	200	N/A
Deposition rate (g/min)	N/A	$\sim 0.1$	10	Up to 330
Dimensional accuracy (mm)	$\pm 0.04$	$\pm 0.05$	$\pm 0.13$	Low
Surface roughness ( $\mu\text{m}$ )	9–10	14–16	$\sim 20$	High
Ref.	[154,155]	[156]	[157]	[158]

### 1.2.3 Microstructured reactors and other process units

Micro process engineering is one of many micro techniques that apply the fundamentals and knowledge of physics/reaction engineering to the implementation of processes/chemical reactions in structures with a lateral size of 50 to 2000  $\mu\text{m}$ . Micro reactors are structured in the micrometer range inside while the external dimensions can reach meters [159,160]. This characteristic setup generally leads to large specific wall area and short distance for transport from the bulk fluid to the wall and therefore good heat and mass transfer. As a new tool for process engineering, micro process engineering increases process reliability, reduces environmental impact, and lowers raw material and energy requirements [161–165]. From an industrial perspective, micro process engineering allows more flexible production and can reduce the time-to-market [166,167].

According to the fabrication methods of components/products for micro process engineering shown in table 1.4, the manufacturing process can be divided into steps including subtractive or additive forming, joining, and hybrid processes. Compared to the manufacturing of conventional size devices, micro-manufacturing faces the following challenges [168,169].

Factors negligible in conventional machining: factors such as vibration, tool-offset, temperature control, rigidity of the tools and chip removal that are negligible in

conventional machining become important in micro-manufacturing due to the requirements for high precision [170].

Table. 1.4 Typical methods/processes in micro-manufacturing [168]

Subtractive processes	Micro-Mechanical Cutting (milling, turning, grinding, polishing, etc.); Micro-EDM; Micro-ECM; Laser Beam Machining; Electro Beam Machining; Photo-chemical-machining; etc.
Additive processes	Surface coating (CVD, PVD); Direct writing (inkjet, laser-guided); Micro-casting; Micro-injection molding; Sintering; Photo-electro-forming; Chemical deposition; Polymer deposition; Stereolithography; etc.
Deforming processes	Micro-forming (stamping, extrusion, forging, bending, deep drawing, incremental forming, superplastic forming, hydro-forming, etc.); Hot embossing; Micro/Nano-imprinting; etc.
Joining processes	Micro-Mechanical-Assembly; Laser-welding; Resistance, Laser, Vacuum Soldering; Bonding; Gluing; etc.
Hybrid processes	Micro-Laser-ECM; LIGA and LIGA combined with Laser-machining; Micro-EDM and Laser assembly; Shape Deposition and Laser machining; Laser-assisted-micro-forming; Micro assembly injection molding; Combined micro-machining and casting; etc.

Volume production and automation: Another problem in micro-manufacturing is process automation. Many time-consuming processes such as material loading and unloading, tool positioning and aligning are manually configured [170].

Tooling dimension: milling and drilling tools down to 25-50  $\mu\text{m}$  are commercially available today. However, for such small dimensions the aspect ratio is limited to 5-10 as deeper plunging and drilling usually will destroy the tool. This feature limits the application of such structures in aerospace and automotive industries [171–173].

Nowadays, additive manufacturing is attracting increasing interest also in micro-manufacturing. Compared to conventional methods, additive manufacturing enables high aspect ratios and is suitable for volume production. Moreover, due to the layer-by-layer working principle, components with complex structures could be fabricated easily [174–176]. As shown in fig. 1.15, Arenas et al. presented an additively manufactured porous electrode. The electrode was printed by a LB-PBF equipment, then a nickel layer was coated on the electrode surface by electrodeposition. Compared to planar electrodes, the additively manufactured porous electrode has a larger surface area [177]. This electrode was printed following the GDLSP concept. However, electrodes printed according to the GUP approach may have even larger surface area [178].

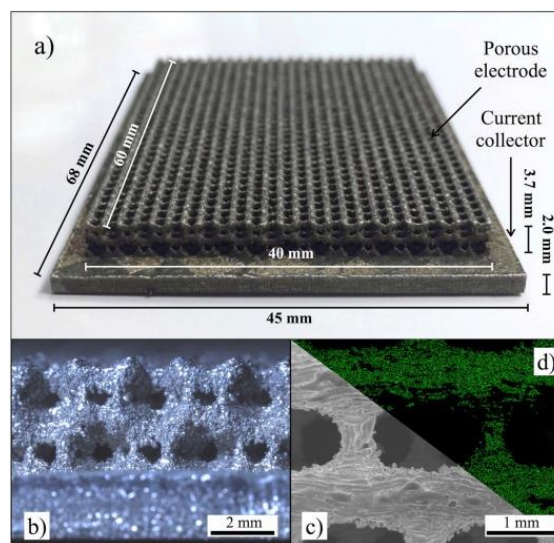


Figure 1.15. (a) additively manufactured stainless steel porous electrode after nickel coating; (b) Side view of the electrode; (c) micrograph of the pore structure; (d) nickel EDS mapping of the electrode [177].

Wei et al. presented a novel additively manufactured reactor named self-catalytic reactor (SCR). As shown in fig. 1.16, three kinds of SCRs (Fe-SCR, Co-SCR, and Ni-SCR) were designed and manufactured for Fischer-Tropsch synthesis,  $\text{CO}_2$

hydrogenation and  $\text{CO}_2$  reforming of  $\text{CH}_4$  [179]. To increase the surface area of the SCR, internal channels and semispherical bulges were designed. The Fe-SCR successfully catalyzed the synthesis of liquid fuels according to the Fischer-Tropsch route. Note that an SCR fabricated from the same material by conventional (subtractive) manufacturing did not show any catalytic activity for Fischer-Tropsch synthesis. One possible reason is the low active surface area. This would imply that an SCR fabricated according to the GUP approach may be more efficient due to the higher surface area. However, it should be noted that in conventional catalysts for Fischer-Tropsch synthesis, the active metal, i.e., Fe, Co or Ru, is present in the form of nanoparticles usually smaller than 20 nm on a porous support with sufficiently large surface area, e.g., alumina or carbon. This particle size range is not accessible with current methods for additive manufacturing. Therefore, the SCR is still a lab concept. But it is still a potential 3D printing reactor development direction to print catalyst and reactor at same time. Especially, a dual-metal LB-PBF printer has been published in 2020.

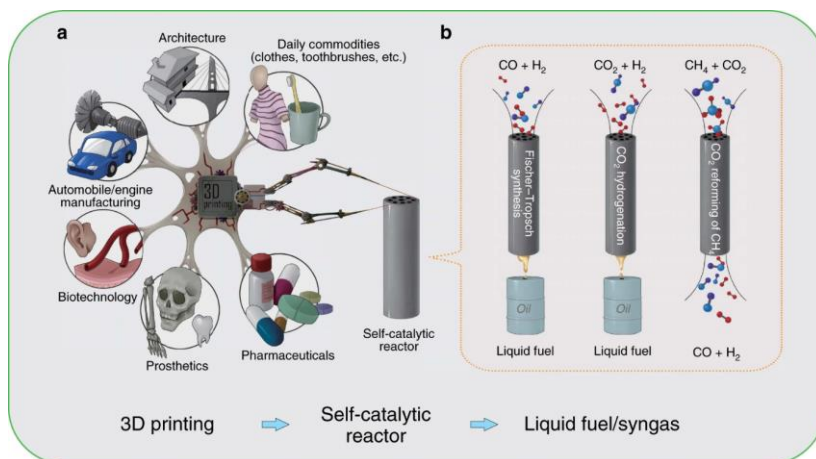


Figure 1.16. 3D printed self catalytic reactors (SCR) for Fischer–Tropsch (FT) synthesis,  $\text{CO}_2$  hydrogenation, and dry reforming of  $\text{CH}_4$  (DRM) [179].

## 1.3 Objectives of this dissertation

Nowadays, additive manufacturing is getting more and more attention. However, different applications may have different requirements on the technique. In last decades, many research focus on producing material with high density. However, a defined porosity, pore size and permeability are desired in some applications e.g., membrane substrate, filter components.

The objectives of this dissertation are to investigate the relation between scanning parameters and pore structure properties of porous materials made by LB-PBF, and to use this knowledge for additive manufacturing of permeable-dense composites. Further, exemplary applications of such composites should be developed.

To characterize the pore structure properties, the pore size distribution of permeable material is measured by a bubble point test. The surface roughness is measured by a 3D optical profilometer. The surface morphology is characterized by scanning electron microscopy (SEM). The permeability is measured by a flow cell system. Samples with different scanning parameters are prepared for the property characterization. The hatch distance of samples ranges from 0.1 mm to 0.15 mm, the laser spot size ranges from 30  $\mu\text{m}$  to 60  $\mu\text{m}$ , the scan strategies of permeable samples include scan vectors oriented in parallel and vertical to the surface. Considering that some applications may have a complex 3D shaped geometry, permeable samples with curved surface should be prepared by different scan strategies, including unidirectional scan vectors (USV), rotation scan vectors (RSV), and four direction scan vectors (FDSV).

To investigate exemplary applications of permeable-dense composites, additively manufactured test modules and conventional test modules had to be prepared for ceramic coating. The samples surfaces before and after ceramic coating had to be characterized by SEM. For further applications, e.g., palladium membrane coating, palladium membrane substrate plates (PMS plate) and palladium membrane substrate tubes (PMS tubes) should be prepared for microreactors with different geometry.

To investigate the additively manufactured microreactor prototype, a plate with microchannels had to be prepared for microstructure characterization. A 90° design strategy and a 45° printing strategy was proposed for microreactor design and printing. Microreactors with internal channels and temperature barrier modules were

designed and printed.

In this dissertation: *chapter 2* investigates the relation between pore structures properties and scanning parameters; *chapter 3* studies the scan strategies of permeable samples with curved surface; *chapter 4* investigates the exemplary applications of permeable-dense composites and reports the designs and printing of the microreactor prototype.

## 2. Additively manufactured permeable metal

The results presented in this chapter have already been published in Xie, D., & Dittmeyer, R. (2021). Correlations of laser scanning parameters and porous structure properties of permeable materials made by laser-beam powder-bed fusion. Additive Manufacturing, 102261.

### 2.1 Materials and methods

#### 2.1.1 System and material

316L stainless steel powder with a size of 10-45  $\mu\text{m}$  provided by LPW Technology Ltd (United Kingdom) and a ReaLizer SLM125 (Germany) LB-PBF machine were used in this study. As shown in figure 2.1, parameters including hatch distance  $hd$ , laser spot size  $d_{LS}$ , scanning direction, etc., can be controlled in the ReaLizer SLM125 operating system. For all samples, the laser power was 80 W, the layer thickness 50  $\mu\text{m}$ , the scan speed 1000 mm/s (laser point distance: 40  $\mu\text{m}$ , exposure time: 40  $\mu\text{s}$ ). In the conventional approach, the laser will first scan the outer line of each layer, which is the external boundary shown in figure 2.1. In this study, in order to prepare permeable materials and to investigate the influence of different parameters on the material properties, all samples were made without external boundary scanning. To make it easier for discussion, as shown in Fig. 2.1, all micrographs were taken from the front surface of the respective specimen.

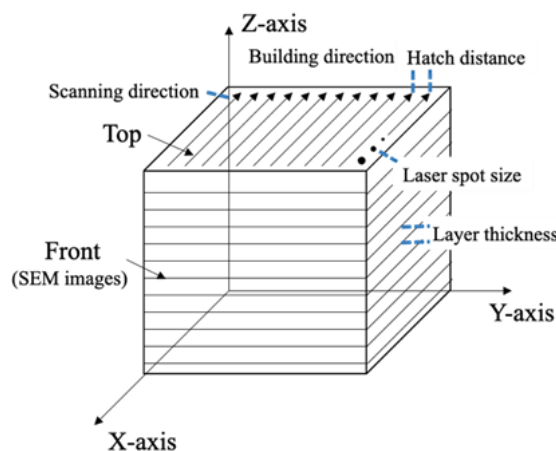


Figure 2.1. Basic scanning parameters. Coordinates refer to the printer's coordinate system. Figure reproduced from Ref. [180].

### 2.1.2 Determination of porosity and pore size distribution

The porosity was calculated following Eqs. (1).

$$\varepsilon = \left( 1 - \frac{m_{s,\text{por}} \cdot \rho_{\text{met}}^{-1}}{A_{\text{por}} \cdot s_{s,\text{por}}} \right) \times 100\% \quad (1a)$$

with

$$m_{s,\text{por}} = m_{s,\text{tot}} - m_{s,\text{den}} \quad (1b)$$

Where  $m_{s,\text{por}}$  is the mass of the permeable part only, as calculated by Eq. (1b) with  $m_{s,\text{tot}}$  being the total mass measured for each individual test sample (via precision balance,  $\pm 1$  mg) and  $m_{s,\text{den}} = 2.565$  g is the mass of the dense part only, determined from a reference sample printed without the permeable part. The dense part of the test samples was smoothed by laser treatment (*TruCell 3010 Trumpf*) for better sealing (see Fig. 2.2). In order to avoid the influence of laser smoothing on weight, all test samples were weighed before laser smoothing. The thickness of the permeable part  $s_{s,\text{por}} = 890$   $\mu\text{m}$  was measured via a 3D optical profilometer (*Sensofar S-neox*, resolution: 0.31  $\mu\text{m}$ ). Its area  $A_{s,\text{por}}$  was defined by the dimensions given in the CAD model ( $l_{\text{por},y} \times l_{\text{por},z}$ : 22 mm  $\times$  10 mm). The density  $\rho_{\text{met}}$  is the bulk density of the metal (316L stainless steel, 8 g  $\text{cm}^{-3}$  [181]).

The pore size distribution of the permeable samples was measured by capillary flow porometry with a *Porometer 3G*. Disk-shaped samples of 25 mm diameter and 1 mm thickness fabricated with different parameters were investigated. In this method, the sample is first immersed in a dedicated measuring liquid characterized by good wetting ability, low surface tension, and low vapour pressure (*i.e.* *POROFIL Quantachrome* for the 316L samples investigated in this study) for 10 minutes to fill all pores of the sample completely. Then the sample is placed in the porometer, and the air is gradually pressurized to displace the liquid from the pores starting from the largest to the smallest pores present in the sample. This results in a gas pressure *vs.* flow curve (wet curve). Subsequently, the gas pressure is gradually decreased to determine the corresponding gas pressure *vs.* flow curve of the dry sample (dry curve). Per sample 256 data points of pressure  $\Delta p_n$  and corresponding gas flow  $\dot{V}_n$  were acquired for both, wet and dry curve. According to the Washburn formula, different pressures correspond to different pore sizes as shown in Eq. (2) [182]:

$$\Delta p \cdot r_{\text{pore}} = 2\gamma_f \cos \theta_f \quad (2)$$

Where  $\Delta p$  is the pressure difference over the sample,  $r_{\text{pore}}$  is the radius of the pore,  $\gamma_f$  is surface tension of the fluid,  $\theta_f$  is the contact angle between the fluid and the solid surface (for gases penetrating a pore ( $\theta_f = 0^\circ$ ), Eq. (2) reduces to  $\Delta p \cdot r_{\text{pore}} = 2\gamma_f$ ). From the measured data  $\dot{V}_{n,\text{wet}}(\Delta p_n)$  resp.  $\dot{V}_{n,\text{dry}}(\Delta p_n)$  for the 256 data points, a flow-based pore size distribution  $v_{\text{diff}}(r_{\text{pore}} = f(\Delta p))$  can be deduced from the cumulative flow values at distinct ( $n$ ) pressure values according to Eqs. (2), (3), and (4) [183].

$$v_{\text{cum},n} = \frac{\dot{V}_{n,\text{wet}}(\Delta p_n)}{\dot{V}_{n,\text{dry}}(\Delta p_n)}; \quad n = 1 \dots 256 \quad (3)$$

$$v_{\text{diff},n} = \frac{(v_{\text{cum}})_{n+1} - (v_{\text{cum}})_{n-1}}{2}; \quad n = 1 \dots 255 \quad (4)$$

Note that  $n$  refers to a distinct pressure difference at which all pores of the size defined by Eq. (2) (or larger) will be opened for the gas flow when starting from a liquid-filled state. Note also that this method always detects the narrowest cross-section of a through pore and reflects a flow-based pore size distribution rather than a volume or number-based pore size distribution.

For determination of the porosity and for permeation tests (chapter 2.2.2 and 2.2.3) permeable-dense composite test samples with a dense frame surrounding the permeable part were printed. For measurement of the pore size distribution, disk-shaped completely permeable test samples were used – exemplary photographs and dimensions are shown in Fig. 2.2.

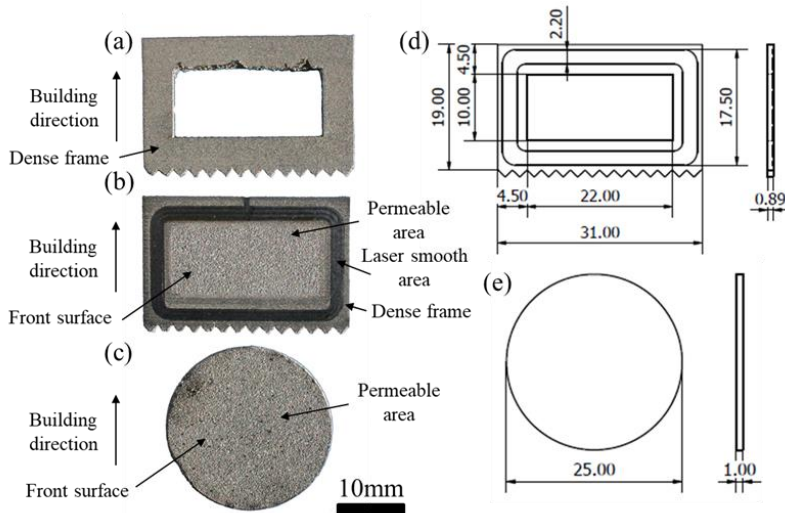


Figure 2.2. (a) Dense frame for porosity measurements; (b) Permeable-dense composite sample for permeability and porosity measurements; (c) Disk-shaped permeable sample for pore size distribution measurements; (d) Schematic of Permeable-dense composite sample; (e) Schematic of disk-shaped permeable sample for pore size distribution. Figure reproduced from Ref. [180].

### 2.1.3 Determination of permeability

The permeability was tested using a flow cell system by measuring the pressure loss at variable flow rates of water permeating through the test sample (see Fig. 2.3). The dense part was first smoothed by laser treatment (see Fig. 2.2), then sealing via the dense part of the test sample was achieved using polymer O-rings. The pressure was measured using a *Baumer PBSN* pressure sensor (range from 0 to 2.5 bar absolute, standard error of measurement:  $\pm 0.03\%$  FSP). The water flow rate was controlled by a *Verdergear VG 1000* basic gear pump. The flow rate was varied from 30 % to 80 % of the maximum rating of 4000 rpm with 10 % intervals and precisely determined for each setting by measuring the amount of water (balance) permeating over 2 minutes. At the beginning of each permeation test, the flow cell system was run for 30 minutes to guarantee stable conditions (sample completely wetted, constant flow rate and pressure loss). During the measurement procedure, the system was allowed to equilibrate for at least 5 minutes after setting a higher flux before measuring the corresponding pressure loss. Based on the amount of water permeating within 120 seconds, the superficial velocity was calculated based on Eq. (5) with  $\rho_{\text{H}_2\text{O}} = 998 \text{ kg m}^{-3}$  and  $A_{\text{s,por}} = 2.2 \text{ cm}^2$  (see also section 2.2.2).

$$u_{sf} = \frac{m_{H_2O}}{\Delta t} \cdot \rho_{H_2O}^{-1} \cdot A_{s,por}^{-1} \quad (5)$$

A linear dependency of the pressure drop on the superficial velocity of a fluid permeating a porous medium can be described by Darcy's law:

$$\Delta p = u_{sf} \cdot \frac{\mu \cdot s}{K} \quad (6)$$

Where  $K$  is the permeability of the porous medium (in  $m^2$ ),  $\Delta p$  is the pressure loss from inlet to outlet (in Pa, absolute numbers),  $\mu$  is the dynamic viscosity of the fluid (here: water 20 °C, 1.01 mPa · s) and  $s$  is the thickness of the porous medium (here:  $s$  equals the thickness of the porous part  $s_{s,por} = 890 \mu m$ ).

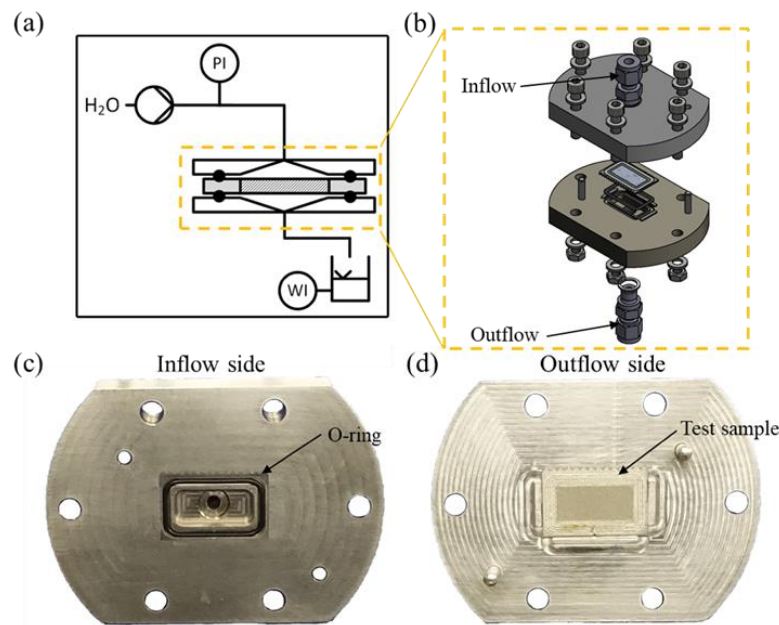


Figure 2.3. Flow cell system for permeability measurements. Figure reproduced from Ref. [180].

#### 2.1.4 Sand blasting

Sand blasting was used to remove the powder sintered on the samples' surface to see the pore structure below. The system pressure during sand blasting was 2.5 bar, and a F150 corundum grit was used.

#### 2.1.5 Morphology

The surface roughness (arithmetic mean height of the surface:  $S_a$ ) was investigated by a 3D optical profiler (S-neox, Sensofar with ISO 25178), and the surface

morphology was studied by scanning electron microscopy (SEM, JSM 6300, Jeol with a 10 kV beam). 3D structure characterization was done by  $\mu$ -CT measurements (ZEISS, Xradia 520 Versa) at the Institute of Mechanical Process Engineering and Mechanics (MVM) of the Karlsruhe Institute of Technology (KIT).

## 2.2 Scan strategy

The relation between different scan strategies and the resulting surface morphology is discussed in this section. Fig. 2.4 shows the schematic of rotation scan vectors. The direction of the scan vectors rotates layer by layer.

### 2.2.1 Scan vector rotation

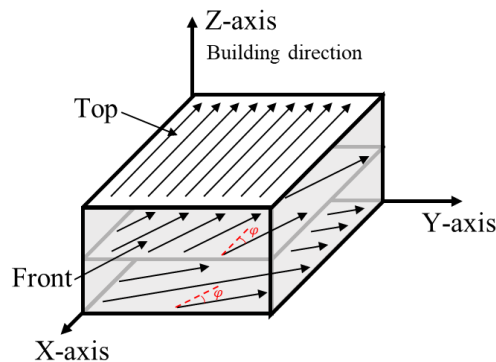


Figure 2.4. Schematic of rotation scan vectors. Coordinates refer to the printer's coordinate system.

Fig. 2.5 shows micrographs of samples produced by different rotation scan vectors ( $12^\circ$ ,  $20^\circ$ ,  $30^\circ$ ). There, many porous lines can be seen on the surface of the samples. With increasing rotation angle, the distance between the porous lines is decreasing. Note that for  $12^\circ$  rotation of the scan vectors per layer, they will return to the initial orientation after 30 layers. This means every 15 layers the scan vectors will be parallel or vertical to the surface. Due to the layer thickness of  $50\ \mu\text{m}$ , every  $700\ \mu\text{m}$  the scan vectors will be parallel or vertical to the surface. Many melting pools can be seen near the porous lines. As shown in fig. 2.9, these melting pools often appear when the scan vectors are parallel to the surface. Therefore, the porous lines are caused by the direction of the scan vectors. The area above the porous line is composed of the initial points of the scan vectors, the area below is composed of the terminal points. The position of the initial and terminal points do not match perfectly, which leads to the formation of a porous line. For  $20^\circ$  rotation per layer, every 450

$\mu\text{m}$  the scan vectors will be parallel to the surface. As shown in fig. 2.5 (b), the distance between two porous lines is  $450\ \mu\text{m}$  in this case.

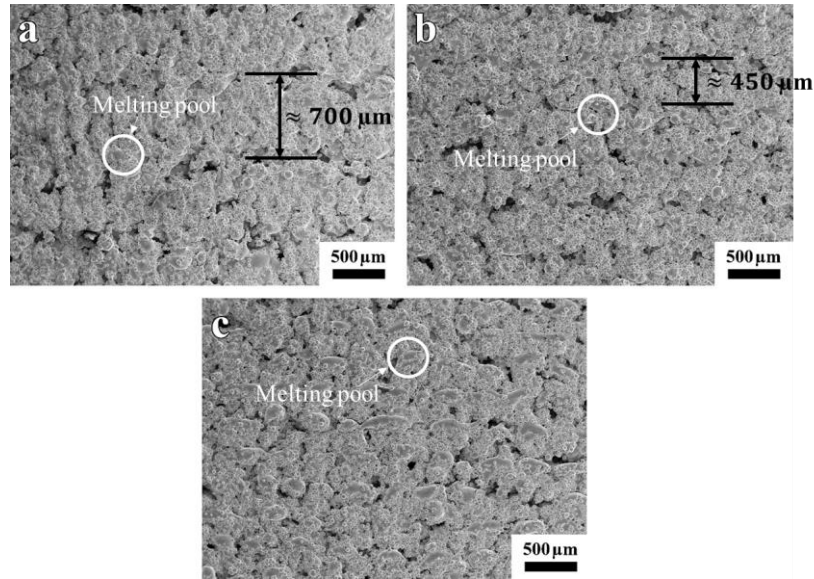


Figure 2.5. SEM micrographs of the front surface for different rotation of the scan vectors per layer: (a) Scan vectors rotate  $12^\circ$  each layer; (b) Scan vectors rotate  $20^\circ$  each layer; (c) Scan vectors rotate  $30^\circ$  each layer.

### 2.2.2 Scan vectors shift position between individual layers

Fig. 2.6 (a) shows the schematic of scan vectors shifting position between individual layers. Every two layers the scan vectors will come back to the initial position. As opposed to this, Fig. 2.6 (b) shows the case where the scan vectors in different layers always keep the same position.

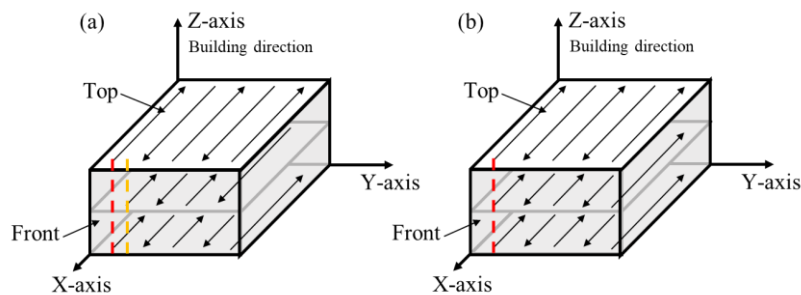


Figure 2.6. (a) Schematic of scan vectors shifting position between individual layers; (b) schematic of scan vectors always keeping the same position between individual layers.

Fig. 2.7. (a) shows micrographs of samples produced by scan vectors shifting position among alternating layers. Since the aim of this thesis is to produce

permeable materials with pore sizes well below  $100\ \mu\text{m}$ , pores larger than  $100\ \mu\text{m}$  are defined as defects. Many defects can be seen on the surface shown in Fig. 2.7 (a). One possible reason is that continuous printing is interrupted by the position shift. Compared to Fig. 2.7 (a), the sample produced by maintaining the position of the scan vectors in each layer shows better surface quality as can be seen in Fig. 2.7. (b). “Step structures” are visible on the surface. As shown in Fig. 2.6. (b), the front surface is composed of initial and terminal points of the individual tracks. There are two reasons which may cause these step structures. First, lack of powder may cause the position of a terminal point to differ from that of the corresponding initial point. Second, the printing program also may be responsible for the position of an initial point not perfectly matching the terminal point position.

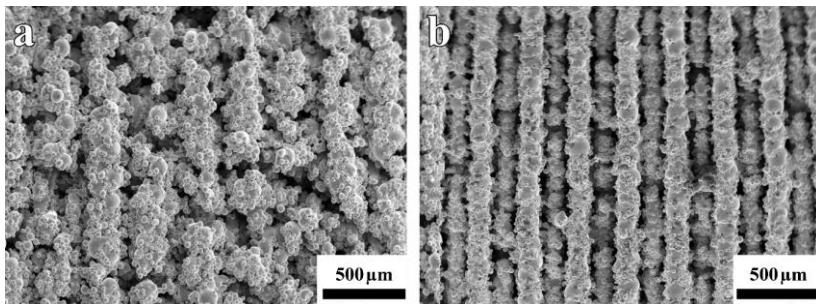


Figure 2.7. SEM micrographs of the front surface with and without shifting of the scan vectors in alternating layers: (a) Scan vectors shifting position between alternating layers; (b) Scan vectors keep the same position for all layers.

### 2.2.3 Unidirectional scan vectors in different direction

Fig. 2.8 shows the schematic of unidirectional scan vectors. As shown in Fig. 2.8 (a), the front surface of a sample printed with unidirectional scan vectors in X direction is composed of the initial points of the scan vectors. As shown in Fig. 2.8 (b), the front surface of a sample printed with unidirectional scan vectors in Y direction is composed of the side faces of the scan vectors.

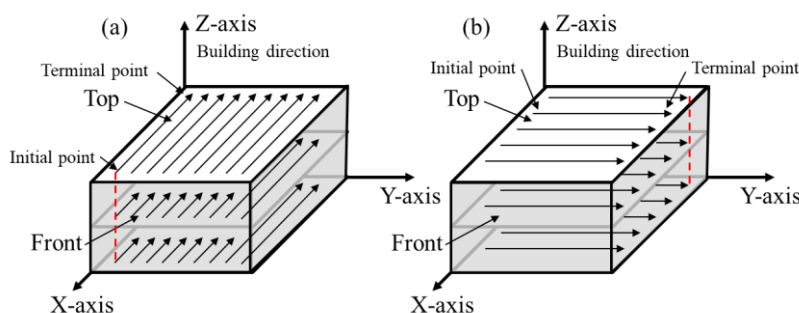


Figure 2.8. (a) Schematic of unidirectional scan vectors in X direction; (b)

Schematic of unidirectional scan vectors in Y direction.

When the scan vectors are parallel to the surface, as shown in Fig. 2.9 (a), melting pools can be seen on the surface. There are two kinds of pores in the additively manufactured permeable material. The first one, as shown in Fig. 2.9 (a), is pores within laser tracks. The second one, as shown in Fig. 2.9 (b), is pores between laser tracks. Comparing Figs. 2.9 (a) and (b), the pores within laser tracks have a larger size, and the formation of pores within laser tracks is random.

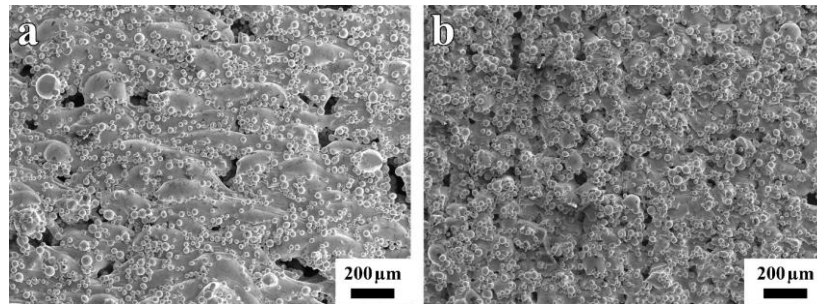


Figure 2.9. (a) Front surface of a sample produced by unidirectional scan vectors in Y direction with 50  $\mu\text{m}$  laser spot diameter; (b) The front surface of a sample produced by unidirectional scan vectors in X direction with 50  $\mu\text{m}$  laser spot diameter.

Fig. 2.10. shows the  $\mu\text{-CT}$  scan results of the sample printed with unidirectional scan vectors with 50  $\mu\text{m}$  laser spot diameter. The through-pores visible in outlines in the top and front views have a small pore size and a direction parallel to the laser tracks. The porosity is mainly contributed by voids in the material which are randomly distributed along these through pores. The cross-sectional images indicate that parts of the laser tracks sintered with each other. Defects on the side face of the scan vectors can be seen in the left view which look similar to defects in Fig. 2.11. (a). In fact, defects found at the faces formed by the terminal points of the laser tracks and defects found on the side faces of the samples originate from the same process. Basically, the reason is lack of powder locally when placing two parallel laser tracks close to each other [184].

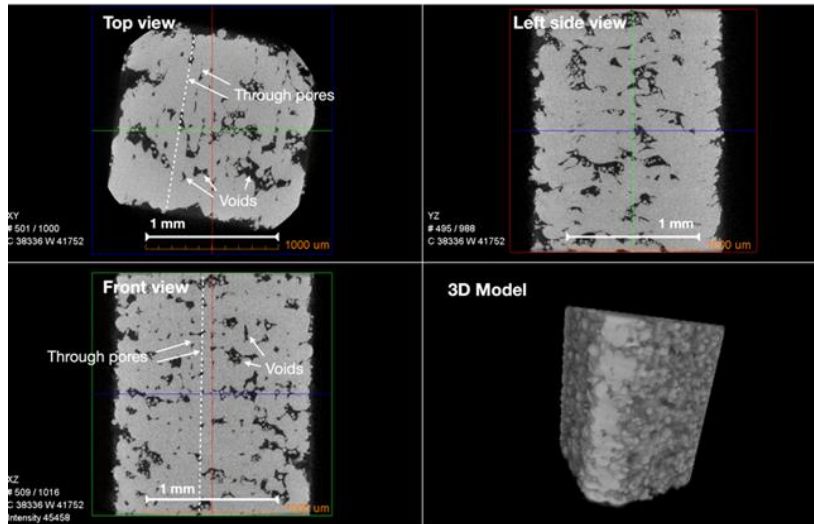


Figure 2.10.  $\mu$ -CT scan model of a sample printed with unidirectional scan vectors with  $50\ \mu\text{m}$  laser spot diameter. Note that the front of the sample produced by unidirectional scan vectors in X direction shown in Fig. 2.9 (b) is the same face as the left (or right) side of sample produced by unidirectional scan vectors in Y direction shown in Fig. 2.9 (a).

Fig. 2.11 shows again samples printed by unidirectional scan vectors, but this time with  $30\ \mu\text{m}$  laser spot size instead of  $50\ \mu\text{m}$  as in Fig. 2.11. Although the laser power was the same, the surfaces of the two types of samples are different. Fig. 2.11 (a) shows a surface with less powder sintered on, Fig. 2.11 (b) shows a surface without pores. In fact, the pores in Fig. 2.11 (a) are defects caused by not fully melted powder in single tracks. Therefore, the pore size and pore distribution of the permeable material made by unidirectional scan vectors in Y direction are quite random. Note that the laser power of the samples in Fig. 2.11 is the same as for the samples in Fig. 2.11. Better single track quality with smaller laser spot size apparently caused the pores to disappear.

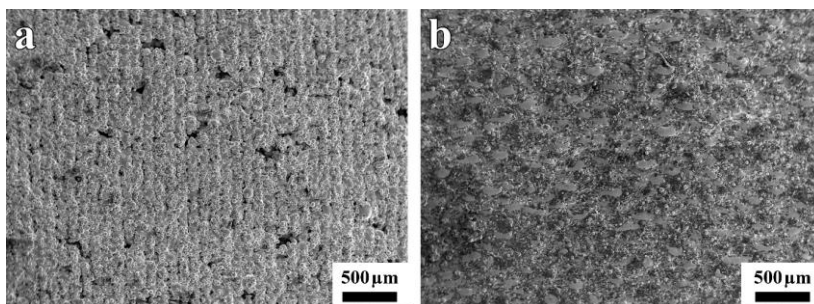


Figure 11(a) Front surface of a sample produced by unidirectional scan vectors in X direction with  $30\ \mu\text{m}$  laser spot diameter; (b) Front surface of a sample produced by

unidirectional scan vectors in Y direction with 30  $\mu\text{m}$  laser spot diameter.

Fig. 2.12 shows front and back surfaces of samples produced again by unidirectional scan vectors. With the same hatch distance, the back surface often has more defects than the front surface. As shown in Fig. 2.10. (a), the front surfaces are composed of the initial points of the scan vectors, and the back surfaces are composed of the terminal points of the scan vectors. During printing, the powder will shrink with laser scanning. Therefore, at the end of a track, there is less powder compared to the onset of the track. The lack of powder makes the back surface have larger size pore structures. With increasing hatch distance, e.g., 0.2 mm instead of 0.1 mm, the terminal points have more powder left around. Therefore, as shown in Fig. 2.12 (b)(d)(f), with increasing hatch distance there are fewer defects on the back surface.

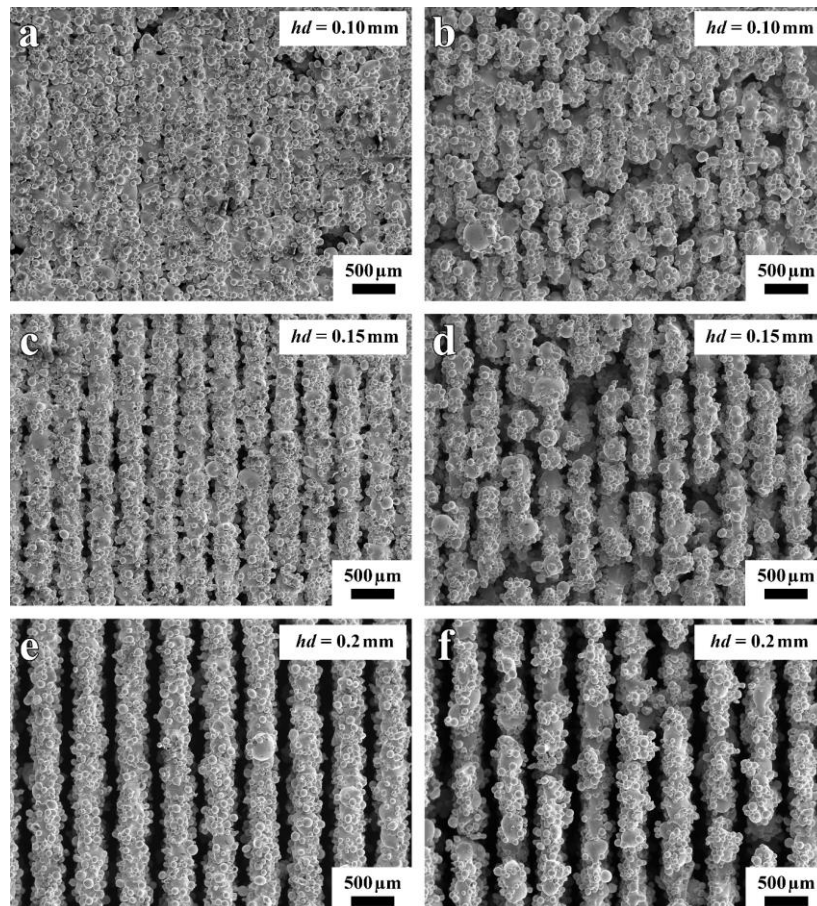


Figure 12 (a) Front surface of hatch distance 0.1 mm specimen; (b) Back surface of hatch distance 0.1 mm specimen; (c) Front surface of hatch distance 0.15 mm specimen; (d) Back surface of hatch distance 0.15 mm specimen; (e) Front surface of hatch distance 0.2 mm specimen; (f) Back surface of hatch distance 0.2 mm specimen.

## 2.3 Laser parameter

### 2.3.1 Laser spot size

As discussed in section 2.3, the front surface of a sample printed by unidirectional scan vectors shows best surface quality. If not otherwise stated all samples in section 2.4 were printed by unidirectional scan vectors. Moreover, the hatch distance of all samples described in section 2.4.1 was 0.1 mm.

The laser spot size of the sample shown in Fig. 2.13 is 50  $\mu\text{m}$ . As shown in Fig. 2.8, the front surface of the sample is composed of the initial points of the individual tracks. Fig. 2.13 (b) shows the front surface of the sample after sand blasting treatment. Pores distribute between tracks, and sand from sand blasting can also be seen on the surface. Comparing Fig. 2.13 (a) and Fig. 2.13 (b), many pores in Fig. 2.13 (a) were covered by surface balling particles.

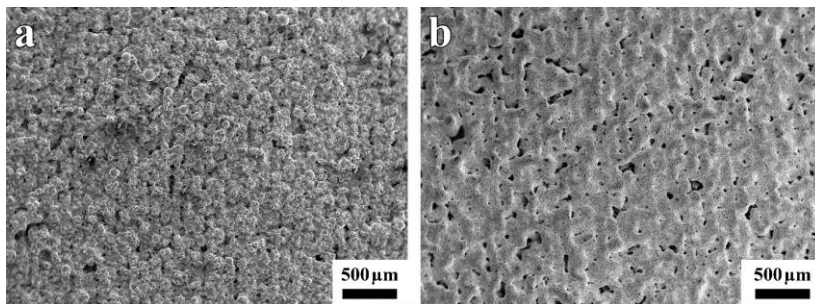


Figure 2.13. (a) T-50 before sand blasting; (b) T-50 after sand blasting

Fig. 2.14 shows the surface structure of samples produced with different laser spot size (30  $\mu\text{m}$ , 40  $\mu\text{m}$ , 50  $\mu\text{m}$ , 60  $\mu\text{m}$ ). The corresponding samples are named T-30, T-40, T-50, and T-60, respectively. Fig. 2.14 (a) shows that there are many defects and gaps present on the front surface of T-30. Fig. 2.14 (b) shows that the powder attached on the surface covers the defects and gaps between the tracks on the front surface of T-40. Figs. 2.14 (c) and (d) show that powder attached on the surface is more obvious on the front surfaces of T-50 and T-60.

When the laser spot size is 30  $\mu\text{m}$ , laser energy is more concentrated. Powder consolidation causes a lot of defects on the surface of the sample, and gaps between adjacent tracks are more obvious [184]. As the laser spot size increases, laser energy gets increasingly dispersed, and so the powder attached on the surface causes defects to be covered and to disappear [185].

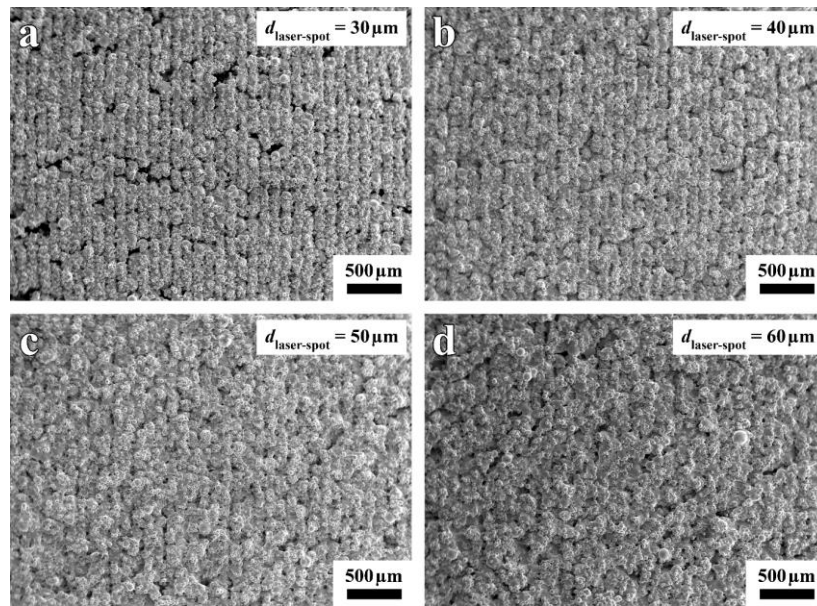


Figure 2.14. (a) Front surface of sample printed by laser spot size 30  $\mu\text{m}$ ; (b) Front surface of sample printed by laser spot size 40  $\mu\text{m}$ ; (c) Front surface of sample printed by laser spot size 50  $\mu\text{m}$ ; (d) Front surface of sample printed by laser spot size 60  $\mu\text{m}$ .

Fig. 2.15 (a) shows the pressure drop during permeation tests on samples obtained with different laser spot size. The linear relation between pressure drop and superficial velocity again confirms the applicability of Darcy's law. The permeability of T-30 is 7.52 times higher than that of T-60. Fig. 2.15 (b) displays the pore size distribution of samples with different laser spot size. The pore size range of T-30 is from 7.2 to 120.3  $\mu\text{m}$  whereas the pore size of T-60 ranges from 2.8 to 17.1  $\mu\text{m}$ .

Fig. 2.15 illustrates that as the laser spot size increases, the permeability and pore size of the samples decrease. However, the data in Table 2.1 shows that the porosity of each sample is almost the same. One possible reason is powder attached on the surface covering the defects and impeding the liquid flow as discussed in the context of Fig. 2.13. The independence of pore size and permeability on porosity is a special feature of additively manufactured permeable materials.

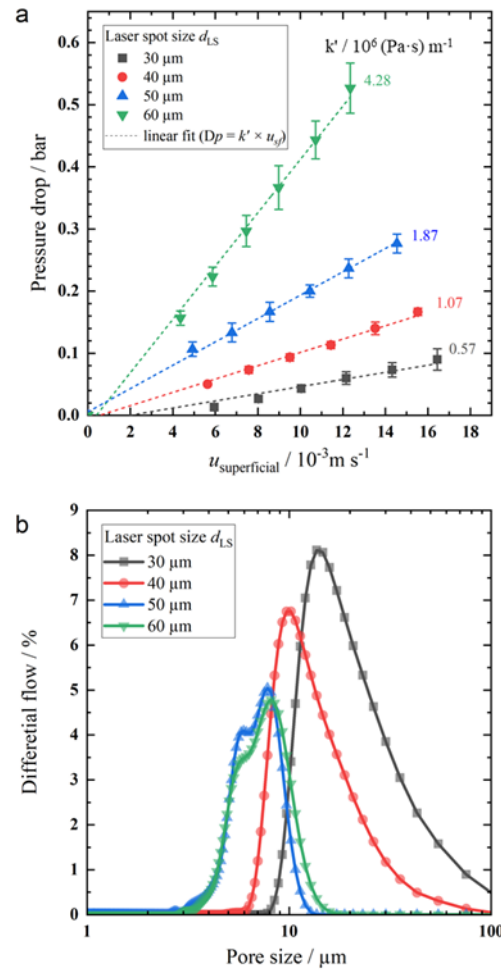


Figure. 2.15. (a) Permeation testing of samples produced with different laser spot size; (b) Pore size distribution of samples with different laser spot size.

When the laser spot size is 30  $\mu\text{m}$  or 40  $\mu\text{m}$ , the laser energy is more concentrated. There is less powder attached on the surface. Therefore, the roughness increases with increasing laser spot size. Usually, roughness will also increase with larger hatch distance but the principle is different.

Table. 2.1. Roughness, porosity, permeability and calculated permeability of samples with different laser spot size

Laser spot size	30 $\mu\text{m}$	40 $\mu\text{m}$	50 $\mu\text{m}$	60 $\mu\text{m}$
Roughness ( $\mu\text{m}$ )	19.66 $\pm$ 0.99	19.04 $\pm$ 0.41	20.37 $\pm$ 0.72	24.01 $\pm$ 0.62
Porosity	21 %	15 %	17 %	16 %
Permeability ( $\text{m}^2$ )	1.58 $\pm$ 0.11E-12	8.4 $\pm$ 0.23E-13	4.81 $\pm$ 0.14E-13	2.1 $\pm$ 0.07E-13

A larger hatch distance will generate higher porosity which comes along with higher

roughness. Increasing the laser spot size will cause more powder attached on the surface and this way increase the roughness. With different laser spot size, there should be more or less particle sintering on the surface.

Figure 2.16 shows a micrograph of the front surface of a sample produced by unidirectional scan vectors with alternately opposite direction, which is named T-A. As shown in Fig. 2.9, the front surface is combined by initial and terminal points of individual tracks. Step structures formed by combining initial and terminal points can be seen in the micrograph. There are two reasons which may cause these step structures. First, like discussed before, lack of powder may cause the position of a terminal point to differ from that of the corresponding initial point. Second, the printing program also may be responsible for the position of an initial point not perfectly matching the terminal point position.

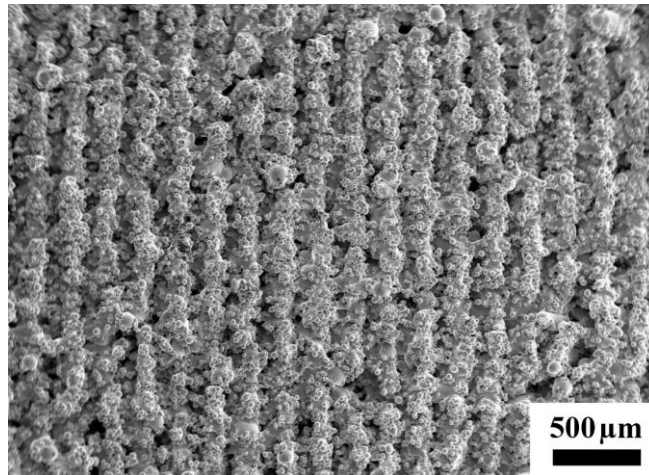


Figure. 2.16. SEM micrograph of the front surface of a sample produced by unidirectional scan vectors arranged alternately opposite.

Fig. 2.17 (a) shows the pressure drop and superficial velocity of samples T-50 and T-A. The linear relation between pressure drop and superficial velocity confirms the applicability of Darcy's law. The permeability of the sample produced with an alternately opposite laser path is 1.81 times higher than for the sample with one direction laser path. Fig. 2.17 (b) is the pore size distribution of T-50 and T-A. The pore sizes of T-50 range from 2.6  $\mu\text{m}$  to 13.7  $\mu\text{m}$ , while T-A shows a broader range from 4.2  $\mu\text{m}$  to 75.2  $\mu\text{m}$ . As discussed above, balling particles cover the pores on the surface of sample T-50. As shown in Fig. 2.16 the pores on the surface of sample T-A cannot be fully covered due to the "step structure". Hence the pore narrowing effect is largely absent. This could be one reason why sample T-A shows

a higher permeability and a wider pore size range.

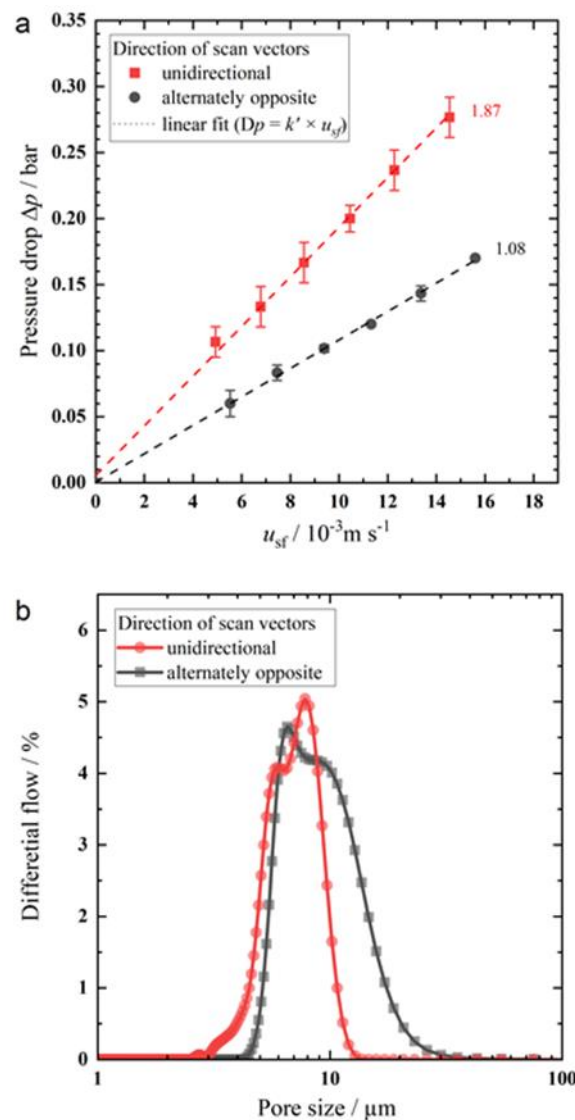


Figure. 2.17. (a) Pressure drop during permeation testing of T-A and T-50; Fig. 2.17 (b) Pore size distribution of T-A and T-50

Table. 2.2 shows that different scanning paths didn't cause a drastic change in porosity. However, the roughness of T-A is 1.52 times higher than that of T-50. As discussed, the reasons could be the effect of powder attached on the surface and the staircase structure.

Table. 2.2. Roughness and porosity of samples made by unidirectional scan vectors arranged alternately opposite and unidirectional scan vectors arranged in the same direction.

Scanning strategy	unidirectional scan vectors	unidirectional scan vectors arranged alternately opposite
Roughness ( $\mu\text{m}$ )	$20.37 \pm 0.72$	$30.88 \pm 0.73$
Porosity	17 %	18 %
Permeability ( $\text{m}^2$ )	$4.81 \pm 0.14\text{E-}13$	$8.32 \pm 0.16\text{E-}13$

### 2.3.2 Hatch distance

In order to make it easier to discuss the effects of the hatch distance, the laser spot size of all samples in section 2.4.2 was fixed to 50  $\mu\text{m}$ . Fig. 2.18 shows micrographs of samples with different hatch distance (0.1mm, 0.11mm, 0.12mm, 0.13mm, 0.14mm, 0.15mm). The corresponding samples are named T-10, T-11, T-12, T-13, T-14, and T-15. With an increase of the hatch distance, the gaps between the tracks in Figs. 2.18 (d), (e), and (f) are more obvious than in Figs. 2.18 (a), (b), and (c). Powder attached on the surface is observed in all figures. However, due to the small gap width, powder attached on the surface is more effective in covering the gaps and generating smaller pores on the surface in case of Figs. 2.18 (a), (b), and (c). Whereas in Figs. 2.18 (e), (f) and (g), the effect of powder attached on the surface is not so obvious.

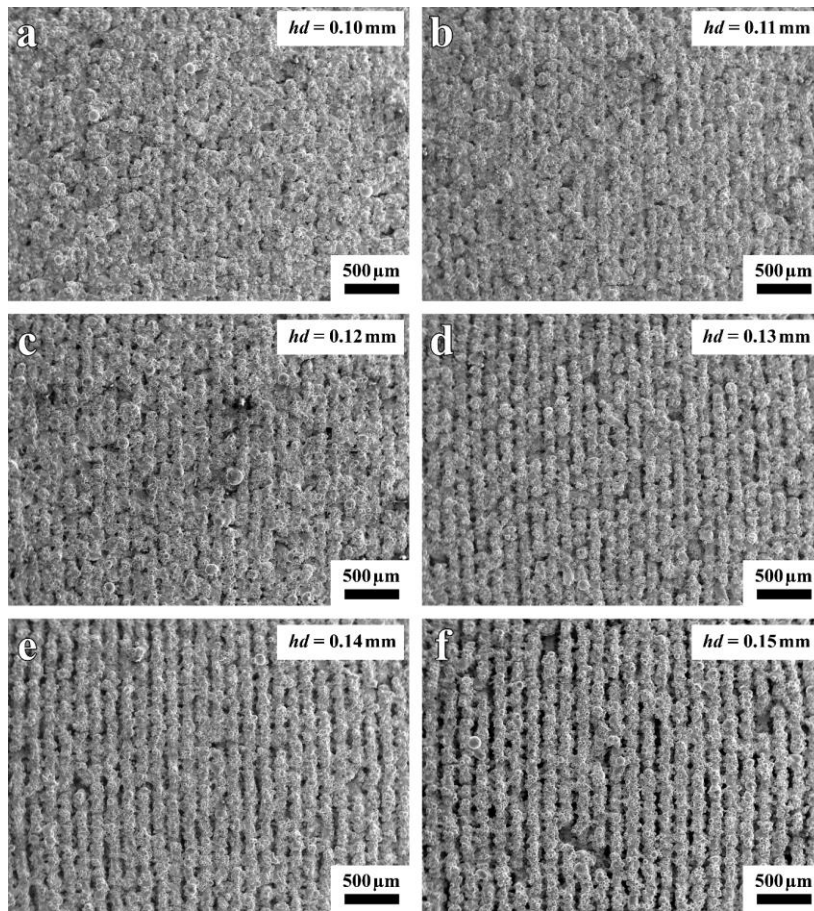


Figure 2.18. (a)(b)(c)(d)(e)(f) Front surface of sample printed by hatch distance 0.1 mm, 0.11mm, 0.12mm, 0.13mm, 0.14mm, 0.15mm;

Fig. 2.19 (a) shows the pressure drop during permeation testing on samples with different hatch distance. The linear relation between pressure drop and superficial velocity once more complies with Darcy's law. The permeability of T-14 (hatch distance: 0.14 mm) is 10.4 times higher than that of T-10 (hatch distance: 0.1 mm). Sample T-15 is not included because the pressure drop was too low to be measured accurately with the present setup. Fig. 2.19 (b) shows the pore size distribution of samples with different laser spot size. The pore size range of T-14 is from 32.4  $\mu\text{m}$  to 84  $\mu\text{m}$ . The pore size range of T-10 is from 2.5  $\mu\text{m}$  to 13.7  $\mu\text{m}$ . With an increase of the hatch distance, permeability and pore size of the samples are gradually increased as shown in Figs. 2.19 (a) and (b). Comparison to the analysis reported in sections 2.4.1 and 2.4.2 yields that increasing the hatch distance is the most effective way to increase the permeability and the pore size. The factor by which the permeability is increased when increasing the hatch distance stepwise from 0.1 mm to 0.14 mm is: 1.23, 1.30, 2.63, 2.44. For a hatch distance higher than 0.13 mm, the rate of increase of the permeability accelerates significantly. According to the above

analysis, an increase of the hatch distance weakens the effect of powder attached on the surface.

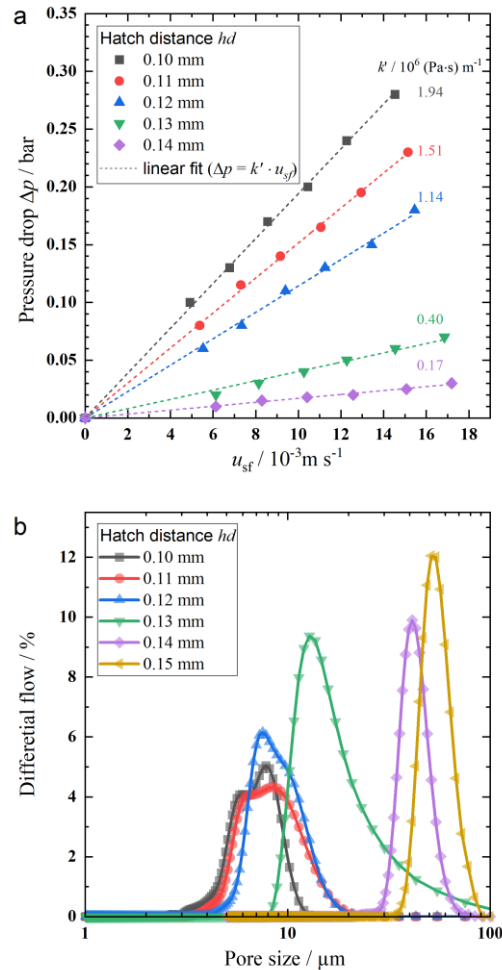


Figure. 2.19. (a) Permeability of samples printed by different hatch distance; (b) Pore size distribution of samples printed by different hatch distance.

Table 2.3 shows the roughness, porosity, permeability and pore to throat size ratio of samples obtained with different hatch distance. From this table it is clear that with increasing hatch distance, roughness, porosity, and permeability all increase. The permeability and pore size distribution of samples with hatch distances of 0.1 mm, 0.11 mm, and 0.12 mm are closer to each other than for the other samples. As discussed, balling covering the defects on the surface could be the reason.

Table 2.3. Roughness, porosity and permeability of samples with different hatch distance.

Hatch distance	0.1 mm	0.11 mm	0.12 mm	0.13 mm	0.14 mm
Roughness ( $\mu\text{m}$ )	20.58	22.53	23.96	26.28	28.61
Porosity	17 %	15 %	19 %	24 %	26 %
Permeability ( $\text{m}^2$ )	4.63E-13	5.95E-13	7.88E-13	2.25E-12	5.29E-12

## 2.4 Permeable-dense composite

By controlling the hatch distance, the porosity and pore size of the material can be changed in a wider range. As shown in Figure 2.20 (a) a KIT logo was fabricated by controlling the scanning direction and the hatch distance. The triangle in the logo is made up by a large pore size material, while the other letters in the logo are formed by small pore size material. The remaining part of the logo is composed of dense material. Fig. 2.20 (b) shows a QR code of IMVT website. The QR code is printed by permeable material and the remaining part of QR code is composed of dense material.

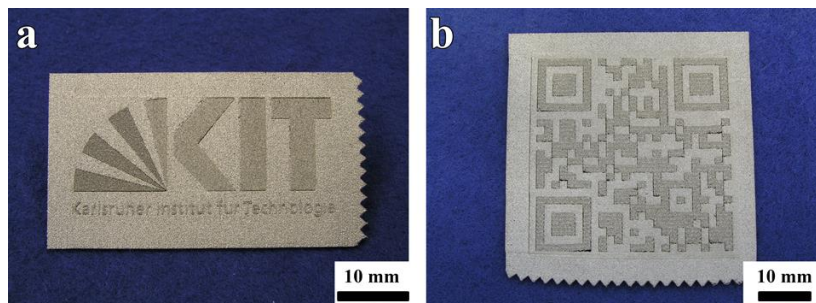


Figure 2.20. (a) additively manufactured KIT logo; (b) additively manufactured QR code

Fig. 2.21 shows the schematic of permeable material with different pore size on different surfaces. The permeable material is printed by two kinds of scan vectors. The front surface is composed of scan vectors with larger hatch distance. The back surface is composed of scan vectors with smaller hatch distance.

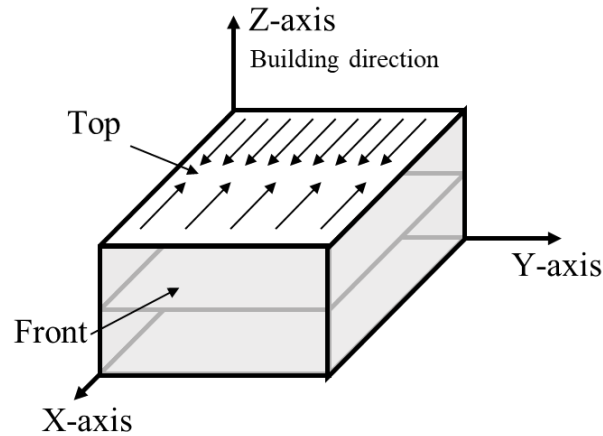


Figure 2.21. Schematic of a permeable material with different pore size on different surfaces.

The hatch distance of the scan vectors at the front surface is 0.13mm, and it is 0.09mm on the back surface. As shown in Fig. 2.22 (a) and (b), the front surface has larger pores than the back surface. Both surfaces are composed of initial points of scan vectors. Therefore, there is no defects on these surfaces caused by a lack of powder. Fig. 2.22 (c) shows the cross section of permeable material with different pore size surface. The difference between the two surfaces can be seen clearly. There is a gap between the two surfaces. The lack of powder at the terminal points of the vectors is one reason of the formation of this gap. Another reason is that the position of the terminal points of the two surfaces did not match perfectly.

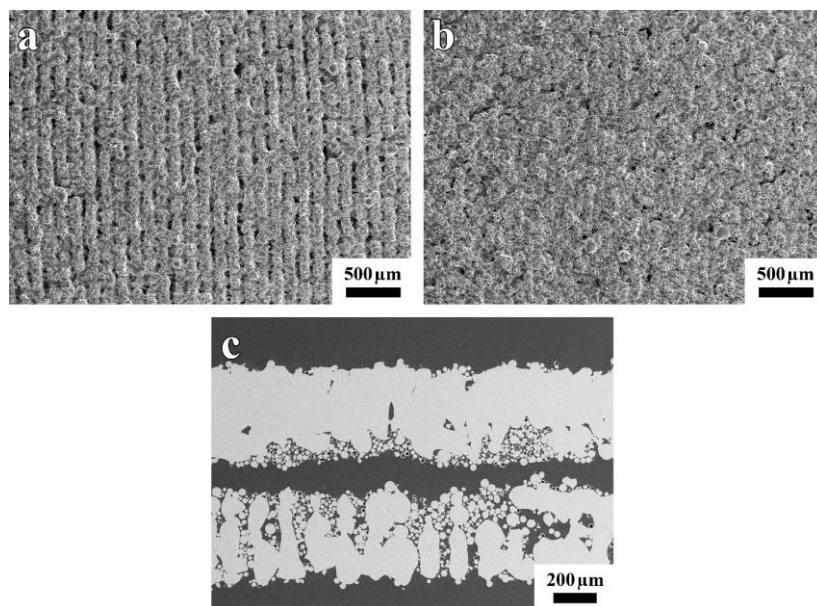


Figure 2.22. Surfaces of a sample printed with different hatch distance. (a) Front surface printed with 0.13 mm hatch distance; (b) Back surface printed with 0.09 mm hatch distance; (c) Cross section of the sample.

## 2.5 Summary and Conclusion

The effect of scan strategies including rotation, position shifting, and unidirectional orientation of the scan vectors on the surface morphology of permeable materials are described and analysed in this chapter. Two kinds of pores in additively manufactured permeable materials are discussed. The pores within laser tracks are unstable and sensitive to the laser parameters. The pores between the tracks are easier to control, e.g., the direction of the pores can be controlled by altering the scanning direction of the laser. On this basis, the effect of different scanning strategies and parameters on the performance of the materials was systematically studied. The permeability of materials with similar porosity can be changed by using different scanning strategies or adjusting the laser spot. The key point of this method is the control of the balling effect. When balling particles cover defects and pores on the samples' surface, the permeability and pore size will be decreased without changing the porosity. If the balling particles do not cover defects or pores, the permeability and pore size will increase while the porosity is the same. By controlling the hatch distance, the porosity and pore size of the material can be changed in a wider range. To provide illustrative examples, a KIT logo, a QR code and a permeable material with different pore size on adjacent surfaces were printed via dense-permeable structures in a flat plate. By accurately manipulating the parameters for permeable and dense structures, materials with various pore structure and dense structure can be printed in one go through LB-PBF. Based on this study, many interesting applications could be expected. Concrete systems under development at the Institute for Micro Process Engineering include engineered supports for palladium composite membranes as key parts of an ultracompact modular membrane reactor system, internals for catalytic reactors with built-in product condensation and phase separation as well as structured parts in compact systems for distillation.

### **3. Additively manufactured permeable metal parts with curved surfaces**

The correlations of laser scanning parameters and porous structure properties of permeable materials was systematically studied in chapter 2. However, all the research in chapter is developed on flat surface and many applications e.g., candle filter requires permeable material with a curved surface. Different with flat surface, curved surface requires the porous structure properties is isotropic. Therefore, a suitable scan strategy needs to be developed. Based on this scan strategy the correlations of laser scanning parameters and porous structure properties of permeable materials on curved surface need to be studied. From the former research, relatively high porosity and roughness can be easily get from the high hatch distance. The main challenge is produce permeable curved material with relatively low roughness.

#### **3.1 System and material**

316L stainless steel powder ( $D_v(50): 31.2 \mu\text{m}$ ) provided by *Carpenter Technology Corporation (United States)* and a *ReaLizer SLM125 (Germany)* LB-PBF machine were used for this study. As shown in Figure 3.1, diameter 30.2 mm, wall thickness 2mm, height 20mm tubes were printed for scanning strategies research. Parameters including hatch distance, layer thickness, and scanning direction can be controlled by the ReaLizer SLM125 operating system. In this study, all samples were printed by the same parameters, i.e., laser power was 80W, hatch distance 0.1mm, layer thickness 50  $\mu\text{m}$ , laser spot size 50  $\mu\text{m}$ , and scan speed 1000mm/s. With front, back, left, and right, four directions were marked for the study of isotropy. In order to avoid the influence of boundary tracks on the surfaces of the permeable materials, all samples were printed without outer and inner boundary scanning.

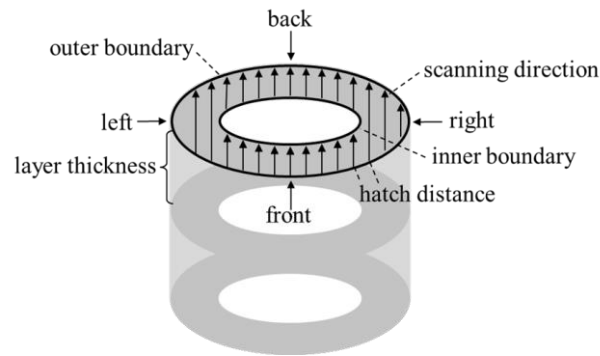


Figure 3.1. Scanning parameters of tubular samples.

## 3.2 Scan strategy

### 3.2.1 Permeable tubes printed by unidirectional scan vectors (USV).

Fig. 3.2 shows the schematic of permeable tubes printed by USV. In the former research, discussed in chapter 2, flat samples printed by USV show the smallest roughness compared to other scanning strategies. However, samples with curved surfaces printed by USV have not yet been studied.

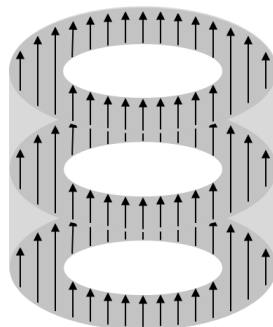


Figure. 3.2. Schematic of permeable tubes printed by USV.

As shown in Fig. 3.3 (a), a staircase structure appeared on the left surface of the sample. From the magnified image, the appearance of a staircase structure is highly related to the position of the sample. When the scan direction is parallel to the sample surface, the staircase structures are more visible. As shown in Fig. 3.3 (b), there was no staircase structure on the front surface of the sample. As the front surface of the sample is composed of the starting points of the vectors, and the left surface is composed of the sides of the vectors, the permeable tube shows different surface morphology at different angular positions.

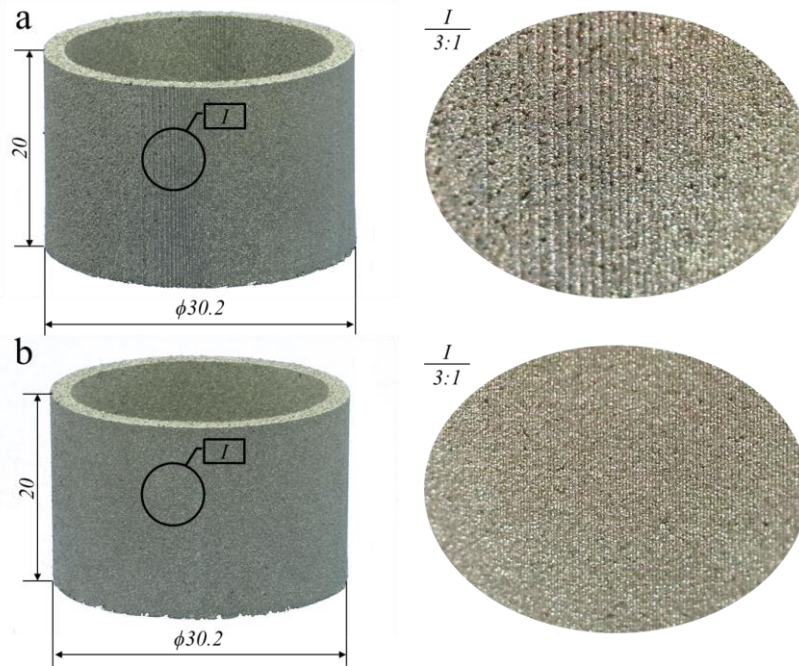


Figure 3.3. (a) Left surface of a permeable tube printed by USV; (b) Front surface of a permeable tube printed by USV.

Fig. 3.4 (a) and (b) show the front and back surface of permeable tubes printed by USV. The front surface is composed of the initial points of the scan vectors and the back surface is composed of the terminal points. Since the position of the scan vectors in every layer is always the same, stripes created by initial points of same position vectors can be seen in Fig. 3.4 (a). During the printing process, powder shrinks with laser scanning. Therefore, there is less power at terminal points than at the initial points of the vectors. As shown in Figs. 3.4 (a) and (b), the back surface shows more defects than the front surface resulting from a lack of powder. Figs. 3.4 (c) and (d) show the left and right surfaces, respectively, of the permeable tube printed by USV. Both left and right surface are composed of the sides of the scan vectors. During laser scanning, not fully melted powder in the laser tracks caused the defects on the left and right surfaces, while the porous structures in the front surface are composed of gaps between individual tracks. The morphology of the two kinds of porous structures in parts with curved surfaces are similar to those in parts with flat surfaces in chapter 2. As shown in Fig. 3.4, with USV, porous structures on a permeable tube are anisotropic. Moreover, the precision of the left and right surface is limited by laser track thickness, which means there are step structures on these surfaces.

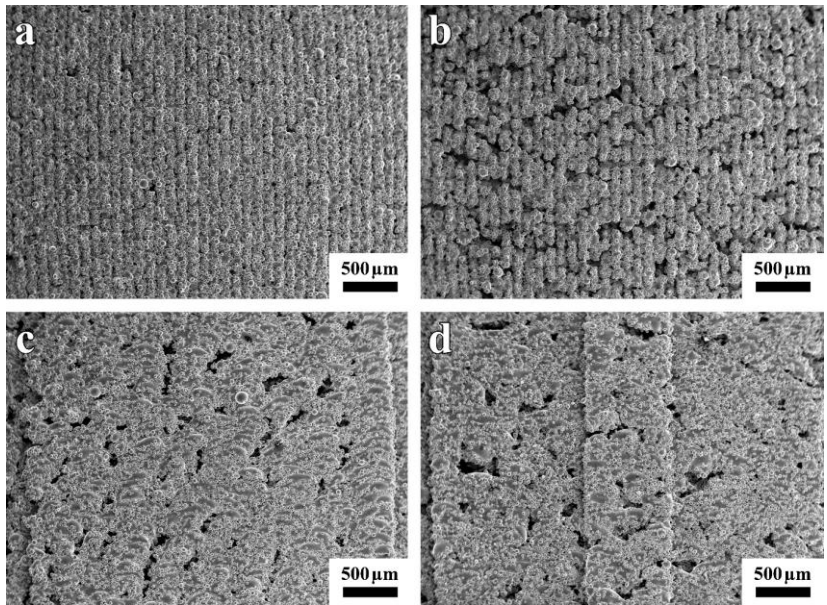


Figure 3.4. Different surfaces of a tubular sample printed by USV. (a) Front surface; (b) Back surface; (c) Left surface ; (d) Right surface.

The integral porosity of the permeable tube printed by USV is 25.3%. As shown in Table 3.1, the roughness of the tube is also anisotropic. The roughness of the front surface is lowest compared to the other surfaces. Owing to defects and staircase structures on the surface, the roughness of the left and right surfaces is higher compared to the other surfaces.

Table. 3.1. Roughness of different surfaces of permeable tubes printed by USV.

Surface	Front	Back	Left	Right
Roughness (μm)	27.3±4.2	35.4±1.6	33.4±2.5	33.8±2.1

### 3.2.2 Permeable tubes printed by rotation scan vectors (RSV).

To obtain a permeable tube with isotropic permeable structures, a permeable tube with 10° RSV was printed. Fig. 3.5 shows the schematic of a permeable tube printed by RSV. Different rotation angles between adjacent layers can be set in the ReaLizer SLM125 operating system.

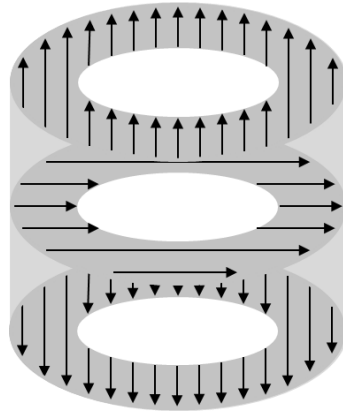


Figure. 3.5. Schematic of permeable tube printed by RSV.

Fig. 3.6 (a) shows a permeable tube printed by  $10^\circ$  RSV. The tube surface is combined of two spirals. As shown in Fig. 3.6 (b), the thicknesses of both spirals are around  $900\ \mu\text{m}$ . Since the layer thickness is  $50\ \mu\text{m}$ , every  $1800\ \mu\text{m}$ , the scan vector will come back to the initial scanning direction. This distance is equal to the thickness of two superimposed spirals. The thickness of the spirals is highly related to the rotation angle. One possible reason of spiral structures is that one spiral is composed of the initial points and the other one by the terminal points of the scan vectors. Therefore, the thicknesses of the two spirals are the same.

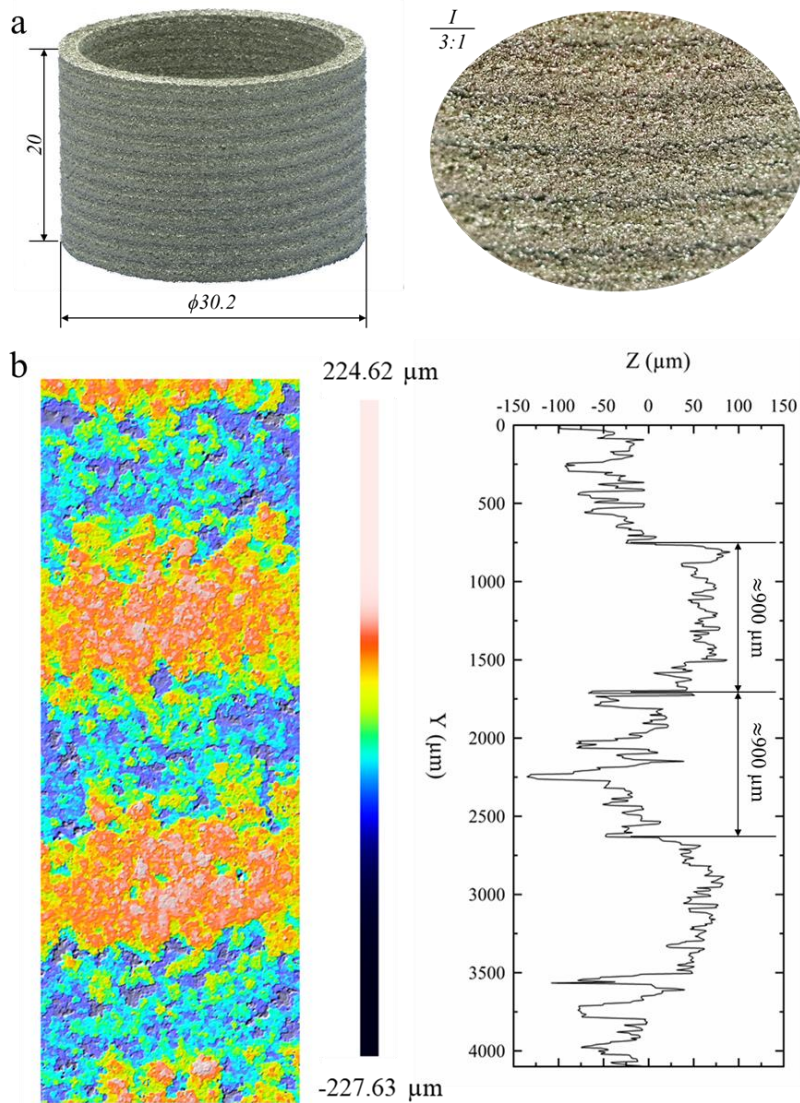


Figure 3.6. Permeable tube printed by  $10^\circ$  RSV; (b) 3D profile of a permeable tube printed by  $10^\circ$  RSV.

Fig. 3.7 (a)(b)(c)(d) show the front, back, left and right surfaces of permeable tube, respectively. The morphology of a permeable tube printed by RSV is isotropic. Melting pools can be seen on the boundary of the two spirals. As shown in Fig. 3.4 (c) and (d), when the scan vectors are parallel to the surface, melting pools can be seen on the surface. Therefore, the boundary of two spirals is also the boundary of the initial and terminal points of the vectors. This phenomenon is consistent with the explanation of the spirals discussed in the context of Fig. 3.6.

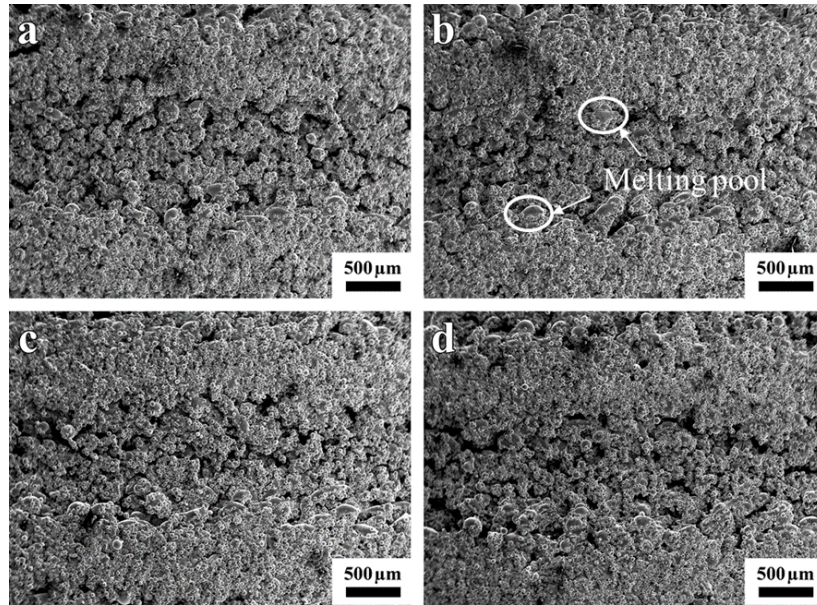


Figure 3.7. (a) Front, (b) back, (c) left, and (d) right surface of a tube printed by 10° RSV.

The integral porosity of the permeable tube printed by 10° RSV is 22.8%. With the same laser power, a permeable tube printed by RSV has a lower porosity compared to a permeable tube printed by USV. Table 3.2 shows the roughness of the surfaces at different sides of a permeable tube printed by 10° RSV. Due to the spiral structure, the surface roughness of a permeable tube printed by 10° RSV is higher than that of a permeable tube printed by USV.

Table 3.2. Surface roughness at different sides of a permeable tube printed by 10° RSV.

Surface	Front	Back	Left	Right
Roughness (μm)	47.6±0.9	44.7±0.8	44.0±1.6	45.2±1.7

Fig. 3.8 (a)(b)(c)(d) shows permeable tubes printed by different RSV. All samples have spiral structures on the surfaces. When the rotation angle is 12°, 20°, 30°, 60°, every 1500 μm, 900 μm, 600 μm, 300 μm the scan vectors will come back to the initial position, respectively. Therefore, as shown in Fig. 3.8 (a)(b)(c)(d), with increasing rotation angle, the pitch of the spirals is decreasing.

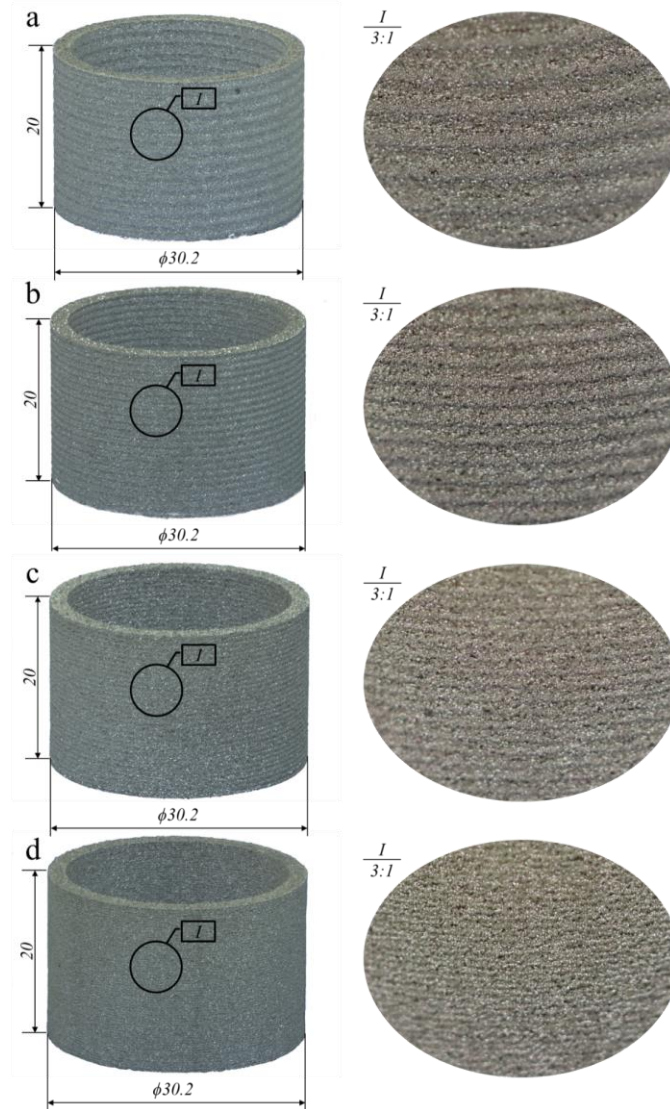


Figure 3.8. Permeable tubes printed by (a) 12° RSV, (b) 20° RSV, (c) 30° RSV, and (d) 60° RSV.

Fig. 3.9 (a)(b)(c)(d) show the micrographs of permeable tubes printed by 12° RSV, 20° RSV, 30° RSV, and 60° RSV respectively. The pitch of the spirals meets the previous expectations, which indicates that the spiral structure can be controlled by the rotation angle of the scan vectors. Moreover, melting pools were found on the outside of all samples. This demonstrates the morphology of these samples can be explained in the proposed way: The two spiral structures on the tube's surface are composed of the initial and terminal points of the scan vectors.

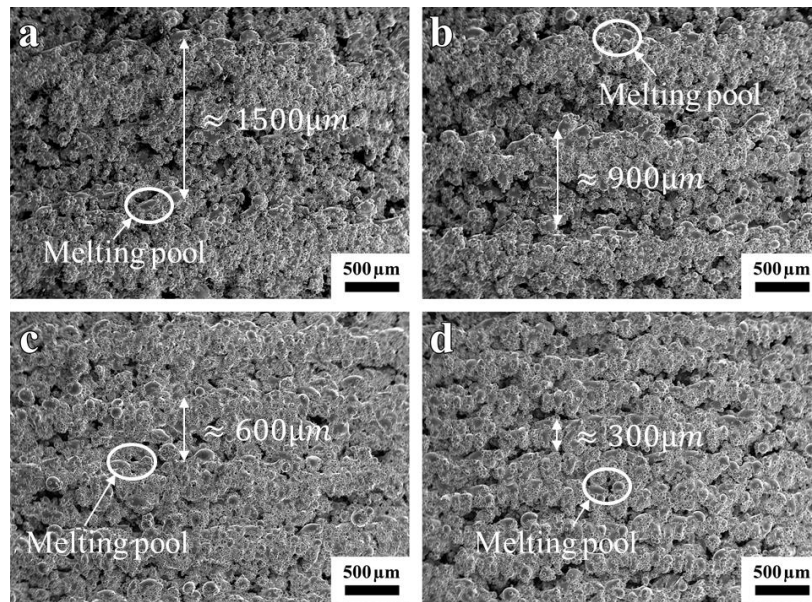


Figure 3.9. (a) Micrographs of permeable tubes printed by 12° RSV, (b) 20° RSV, (c) 30° RSV, and (d) 60° RSV.

As shown in Table 3.3, the permeable tube printed by 60° RSV shows the lowest porosity compared to all other samples. In order to get a lower roughness, all samples printed by RSV have a lower integral porosity compared to the front surface of permeable tubes printed by USV (the lowest roughness we got). The roughness of the permeable tubes printed by RSV is higher than the roughness of the front surface of a permeable tube printed by USV. As shown in Table 3.1, the surface composed of terminal points of the scan vectors has a higher roughness than the surface composed of the initial points of the scan vectors.

Table. 3.3. The porosity and roughness of permeable tubes printed by different angle of RSV.

Rotation angle	12°	20°	30°	60°
Porosity	21.9%	22.0%	22.0%	20.6%
Roughness (μm)	45.4±4.2	44.9±2.8	44.7±1.1	38.7±2.2

### 3.2.3 Permeable tubes printed by four direction scan vectors (FDSV).

Fig. 3.10 (a) shows the schematic of a permeable tube printed by FDSV. The angles of FDSV are 45°, 135°, 225°, and 315°, respectively. Fig. 3.10 (b) shows the schematic of a permeable tube printed by four direction vectors and connection scan vectors (FDCSV). This scan strategy uses four direction vectors, and the scan

vectors in different direction are connected by 1mm long connection vectors. Fig. 3.10 (c) shows the schematic of a permeable tube printed by four direction overlap scan vectors (FDOSV). This scan strategy is composed of FDSV, and there is 0.5 mm overlap between the scan vectors in different direction.

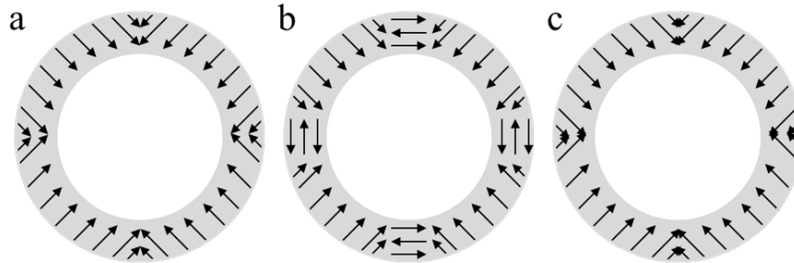


Figure 3.10. (a) Schematic of a permeable tube printed by FDSV; (b) Schematic of a permeable tube printed by FDCSV; (c) Schematic of a permeable tube printed by FDOSV.

Fig. 3.11 (a) shows the permeable tube printed by FDSV. There is a gap between scan vectors in different direction. As shown in Fig. 3.11 (a), the area near the gap is composed of the terminal points of the scan vectors. The lack of powder at the terminal points is one reason for gap formation. Another reason is that the position of the terminal points of the scan vectors in different direction did not match perfectly. As shown in Fig. 3.11 (b), the parts printed by different scan vectors are not combined with each other. The permeable tube printed by this scan strategy cannot be exist on its own without supporting structures.

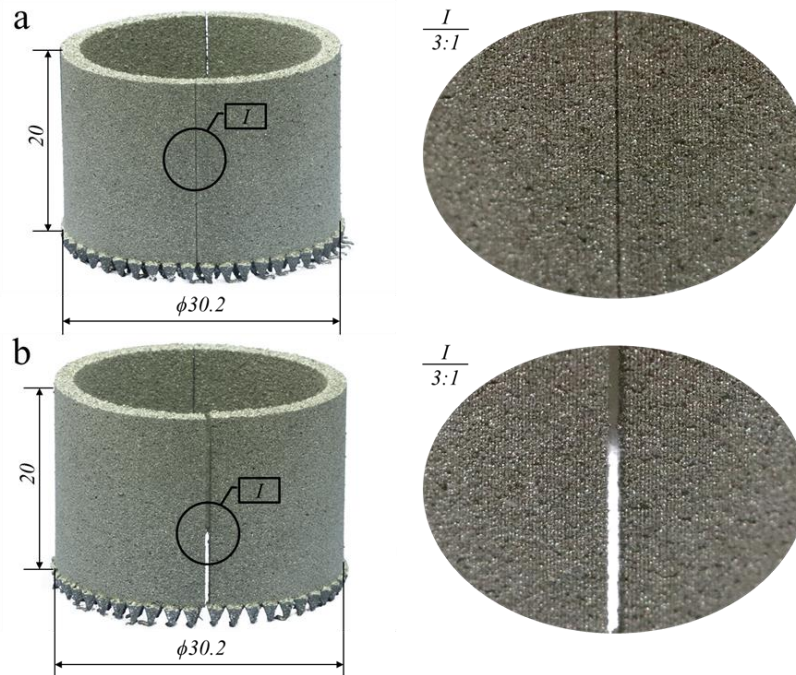


Figure 3.11. (a) Permeable tube printed by FDSV; (b) Gap between scan vectors in different direction.

Fig. 3.12 (a) shows the permeable tube printed by FDCSV. A groove created by the connection vectors can be observed between the individual permeable parts printed by scan vectors in different directions. As shown in Fig. 3.12 (b), the width of this groove is around  $100\ \mu\text{m}$ . There is a  $200\ \mu\text{m}$  gap at the right side of the groove. One possible reason is that the connection vectors are alternating opposite vectors. The first vector on the surface is printed from left to right. Since the terminal point experiences a lack of powder and the positions may not match perfectly, a gap was created on the right side of the groove. While the second vector was printed from right to left and the hatch distance was  $100\ \mu\text{m}$ . Therefore, the thickness of the gap is  $200\ \mu\text{m}$ .

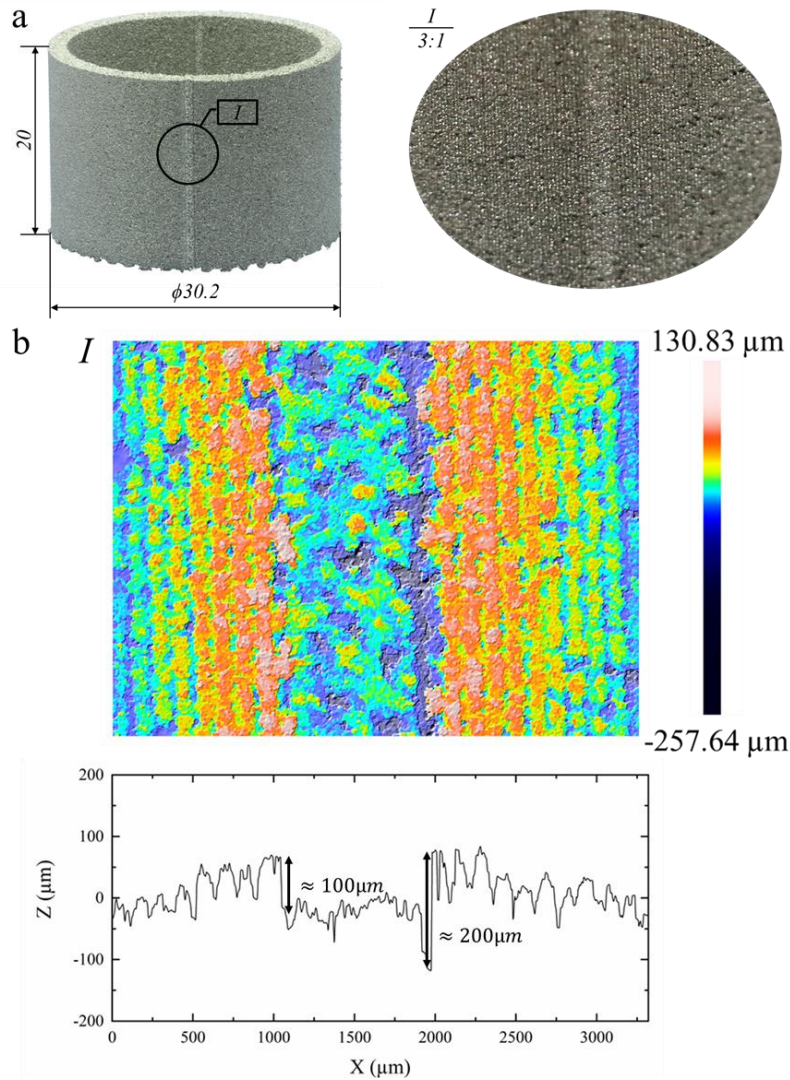


Figure 3.12. (a) Permeable tube printed by FDCSV; (b) 3D profile of the groove on the surface of the permeable tube.

Fig. 3.13 (a) shows the permeable tube printed by FDOSV. There is an overlap area between the scan vectors in different directions. Since the overlap area is composed of more initial points of scan vectors, the stripe structures in the overlap area cannot be seen in Fig. 3.13 (b). It can be observed from the height of the 3D profile that there is no convex or concave structure in the overlap area.

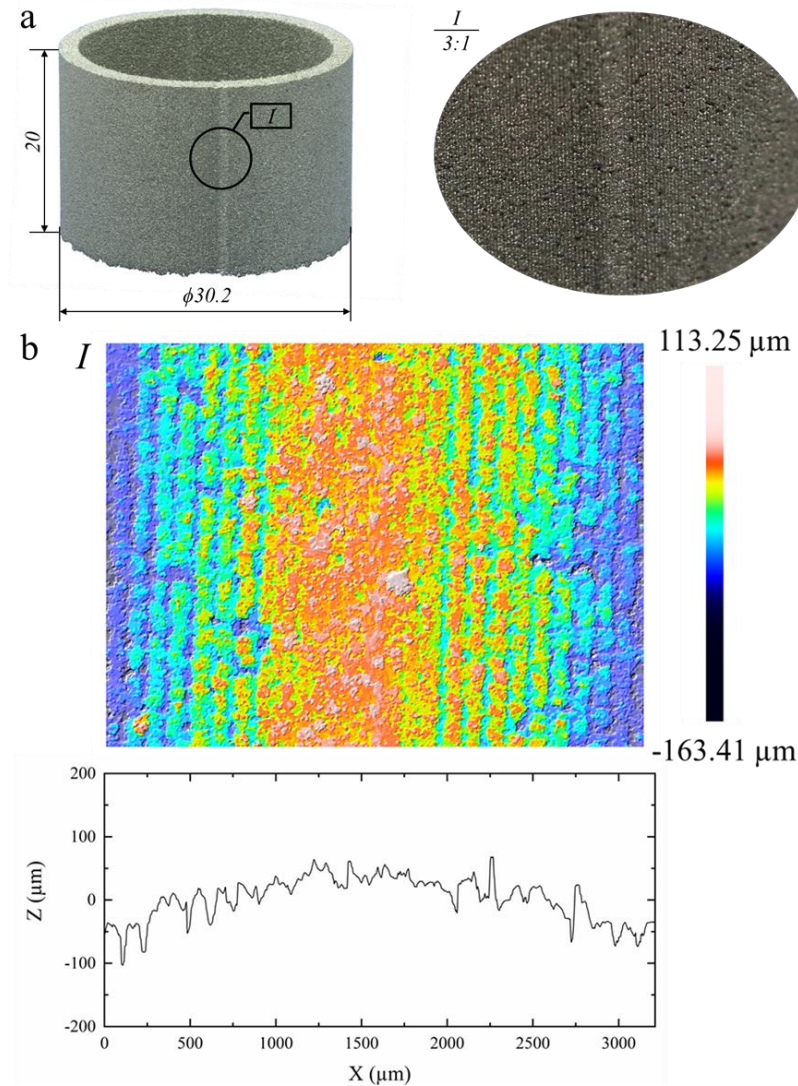


Figure 3.13. (a) Permeable tube printed by FDOSV; (b) 3D profile of a permeable tube printed by FDOSV.

The roughness of the permeable tube printed by FDOSV was measured from four directions. As shown in Table 3.4, the roughness from all four directions is lower than 18  $\mu\text{m}$ . Compared to the permeable tubes printed by RSV, the roughness of a permeable tube printed by FDOSV is lower. Compared to a permeable tube printed by USV, the roughness of a permeable tube printed by FDOSV is isotropic.

Table 3.4. Roughness of different surfaces of a permeable tube printed by four direction overlap vectors.

Surface	Front	Back	Left	Right
Roughness ( $\mu\text{m}$ )	$27.6 \pm 0.9$	$28.9 \pm 1.4$	$27.4 \pm 1.2$	$27.9 \pm 1.1$

### 3.3 Laser parameters

#### 3.3.1 Hatch distance

Fig. 3.14 shows the front surfaces of curved permeable samples printed by different hatch distance. Except the hatch distance, the other scan parameters were the same as for the samples discussed in chapter 3.1. With an increase of the hatch distance, the gaps between the laser tracks in Fig. 3.14 (d)(e)(f) are more obvious than those in Fig. 3.14 (a)(b)(c). The balling phenomenon is observed in all figures. However, due to the small gap width, balling promotes covering of the defects by particles and the formation of smaller pores as shown in Figs. 3.14 (a), (b), and (c). Whereas in Figs. 3.14 (e), (f) and (g), the effect of balling is not so obvious. This phenomenon is similar to the flat samples discussed in chapter 2.4.2.

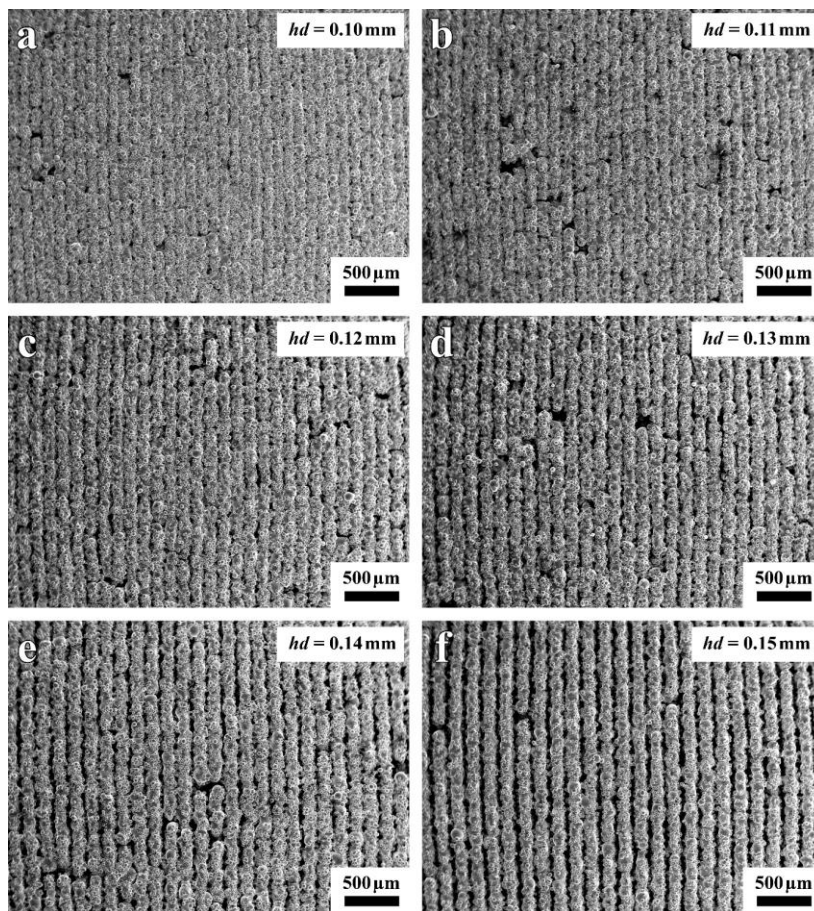


Figure 3.14. Front surface of curved permeable samples printed by different hatch distance; (a) 0.1 mm; (b) 0.11 mm; (c) 0.12 mm; (d) 0.13 mm; (e) 0.14 mm; (f) 0.15 mm.

Table 3.5 shows the porosity of samples obtained with different hatch distance.

From this table, it is clear that with increasing hatch distance porosity are increasing. The porosity of samples with hatch distances of 0.1 mm, 0.11 mm, and 0.12 mm are closer to each other than for the other samples. As discussed, balling covering the defects on the surface could be the reason, which is same as for the flat samples discussed in chapter 2.4.2.

Table 3.5. Porosity of permeable tubes printed by different hatch distance.

Hatch distance (mm)	0.1	0.11	0.12	0.13	0.14	0.15
Porosity	25%	29%	30%	35%	42%	-

### 3.3.2 Laser spot size

Fig. 3.15 shows the front surfaces of curved permeable samples printed by different laser spot size. Except the laser spot size, all other scan parameters were the same as for the samples discussed in chapter 3.1.

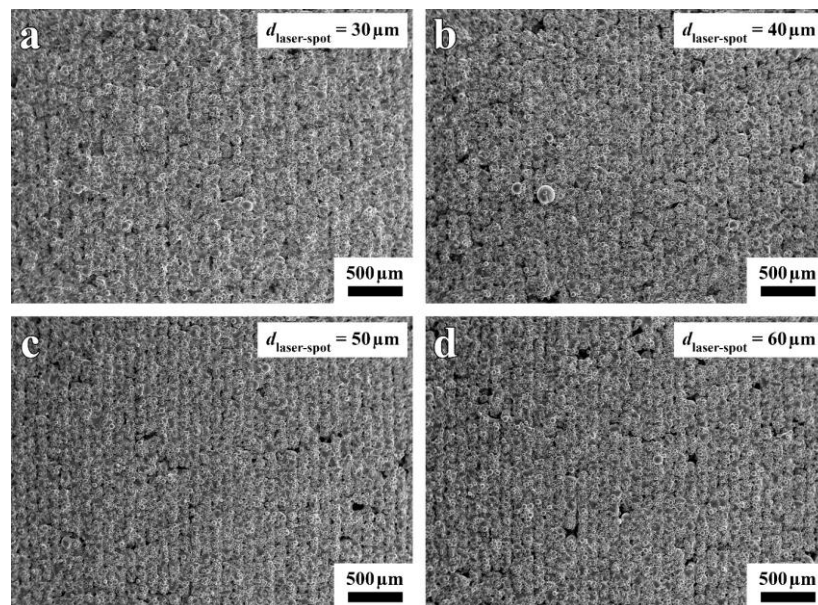


Figure 3.15. Front surface of curved permeable samples printed by different laser spot size; (a) 30 μm; (b) 40 μm; (c) 50 μm; (d) 60 μm.

As shown in Fig. 3.15 (a), when the laser spot size is 30 μm, the defects on the surface are covered by sintered powder. With an increase of the laser spot size,

balling effects in Fig. 3.15 become more and more similar. This is different from what was observed for flat samples in chapter 2.4.2. One possible reason is that the powder size for the curved samples was smaller than for the flat samples (see chapter 2.2 and 3.1).

Table 3.6 shows the roughness and porosity of samples obtained with different laser spot size. With increasing laser spot size, compare with samples prepared by different hatch distance, the porosity do not show significant changes. The laser spot size has no influence on the laser energy density. This is one reason why the porosity does not show significant changes.

Table. 3.6. Porosity of permeable tubes printed by different laser spot size.

Laser spot size ( $\mu\text{m}$ )	30	40	50	60
Porosity	21%	25%	25%	23%

### 3.4 Permeable-dense composite with bending surface

Fig. 3.16 (a) shows permeable-dense tubes with 30 mm, 20 mm, 10 mm outer diameters were printed by FDOSV. The height of the permeable part is 2 mm and the wall thickness of all tubes is 2 mm. On the bottom and top of the permeable tube, 5 mm dense structures were printed. A permeable-dense tube with 0.5 mm, 1 mm, 1.5 mm, and 2 mm wall thickness in different angular position was printed by FDOSV and is shown in Fig. 3.16 (b). The outer diameter of the permeable part is 30 mm, and the height of the permeable part is 20 mm. On the bottom and top of the permeable tube, 5 mm dense structures were printed. As shown in Fig. 3.16 (a) and (b), with FDOSV scanning strategy, permeable parts with curved surface can be printed with different diameter and thickness. Permeable parts and dense parts can be combined freely.

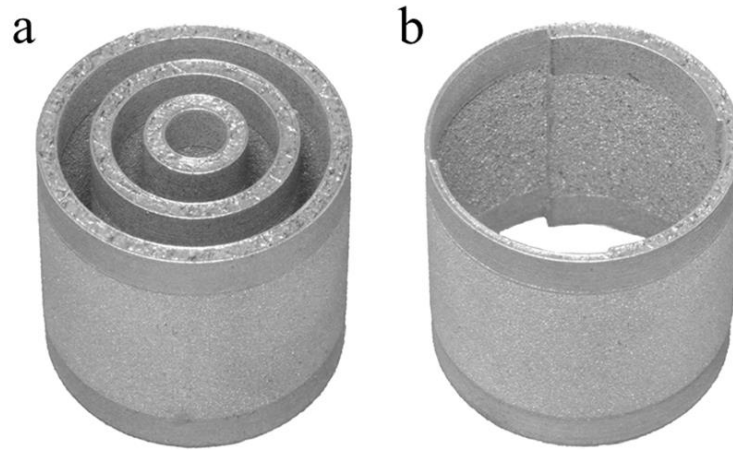


Figure 3.16. Different diameter permeable-dense tubular samples printed by FDOSV; (b) Different thickness permeable tube printed by FDOSV.

### 3.5 Summary and Conclusion

In this study, three types of scanning strategies were discussed for printing of permeable parts with tubular geometry. The permeable tube printed by USV shows anisotropy of the surface morphology. The front surface made up of the initial points of the scan vectors has the lowest roughness compared to the other surfaces. The back surface composed of the terminal points of the scan vectors shows defects. The left and right surfaces created by the sides of the scan vectors have staircase structures. Permeable tubes printed by rotation scan vectors show isotropy of the surface morphology. Two spiral structures composed of the initial and terminal points of the scan vectors can be observed on the tube surface. The pitch of the spirals is highly related to the scan vector rotation angle. Permeable tubes printed by  $60^\circ$  RSV have the smallest pitch size and lowest surface roughness among all permeable tubes printed by RSV. Permeable tubes printed by FDSV show gaps between the scan vectors in different direction. Permeable tubes printed by FDCSV show grooves between the scan vectors in different directions. Permeable tubes printed by FDOSV show lower surface roughness compared to permeable tubes printed by RSV, and the surface roughness is isotropic.

The relation between hatch distance, laser spot size and surface morphology, porosity, and roughness was studied. With increasing hatch distance, porosity and roughness are both increasing, and the gaps between the laser tracks become more obvious. This phenomenon is similar to flat samples discussed in chapter 2.3.2.

Compare with different hatch distance, with increasing laser spot size, porosity and roughness do not show significant changes. However, the roughness of permeable material with flat surface is increasing with increasing laser spot size. From the micrographs of flat and curved samples, the morphologies of two kinds of samples are similar with each other. One possible reason for the difference is that the powder size used for printing of samples with curved surface was smaller than for the flat samples. The powder attached on the surface is easier to fill into the space between the powders.

Based on this research, permeable-dense tubes with different outer diameter and wall thickness can be printed by FDOSV.

## 4. Preliminary research on additively manufactured components for a microstructured membrane steam reformer

### 4.1 Palladium membrane substrate

#### 4.1.1 Test module preparation

The quality of the palladium membrane directly determines the effectiveness of the membrane reactor for delivering pure hydrogen [8]. Therefore, test specimen based on different concepts were prepared for palladium membrane coating tests. Fig. 4.1 shows the geometry of the test specimen.

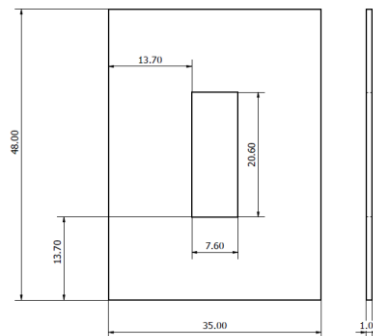


Figure 4.1. Geometry of the test specimen. Dimensions are given in mm.

Fig. 4.2 (a) shows a conventional test specimen. A porous sintered metal plate (*Crofer 22 APU*) is combined with a dense frame (*Crofer 22 APU*) by laser welding (*TruCell 3010 Trumpf*). A welding seam between the porous substrate and the dense frame can be seen in Fig. 4.2 (a). Fig. 4.2 (b) shows an additively manufactured test specimen. In order to get a low surface roughness and small pore size, the scan strategy and laser parameters were chosen the same as for sample T-50 in chapter 2.2.3. Since the additively manufactured test specimen can be printed in one step, an extra welding step is not necessary. Therefore, there is no welding seam on the additively manufactured test specimen.

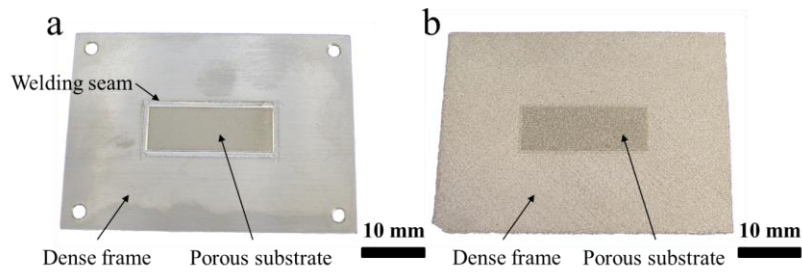


Figure 4.2. (a) Conventional test specimen; (b) Additively manufactured test specimen.

Fig. 4.3 shows the 3D profile of the connection area of the test specimens. The welding seam between the porous and dense parts can be seen in Fig. 4.3. The area left of the welding seam is the dense frame. The right area of the welding seam is the porous substrate. From the height measurement results, the thickness of the welding seam is around  $50\ \mu\text{m}$ . The porous substrate is not exactly parallel to the dense frame. The interior stress caused by the laser welding may be one reason for that. The roughness of the porous substrate is  $2.72\ \mu\text{m}$ .

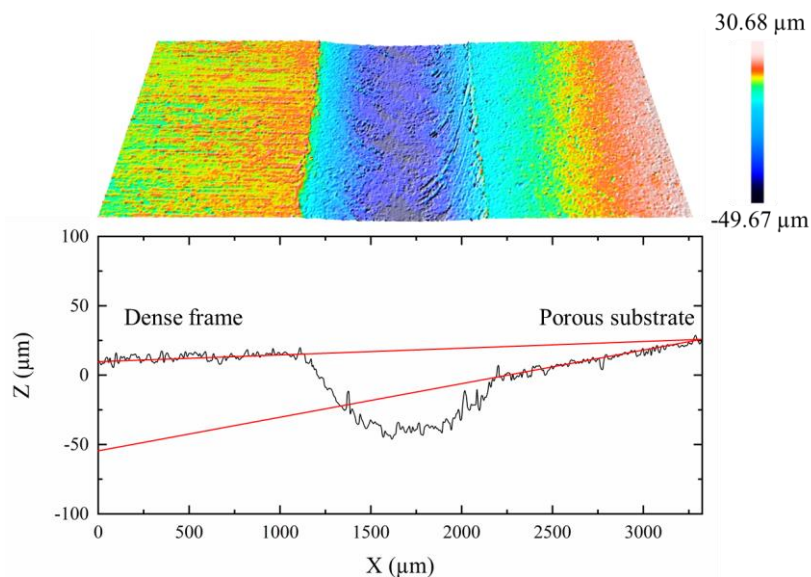


Figure 4.3. Connection area of porous substrate and dense frame in a conventional test specimen.

Fig. 4.4 shows the connection area of permeable and dense structures for the additively manufactured test specimen. Again, the area left is the dense frame, and the area right is the permeable substrate. The roughness of the permeable substrate is  $20.10\ \mu\text{m}$ . As seen in the height measurement, there is no extra weld seam between

permeable substrate and dense frame, and the two parts stands in the same height.

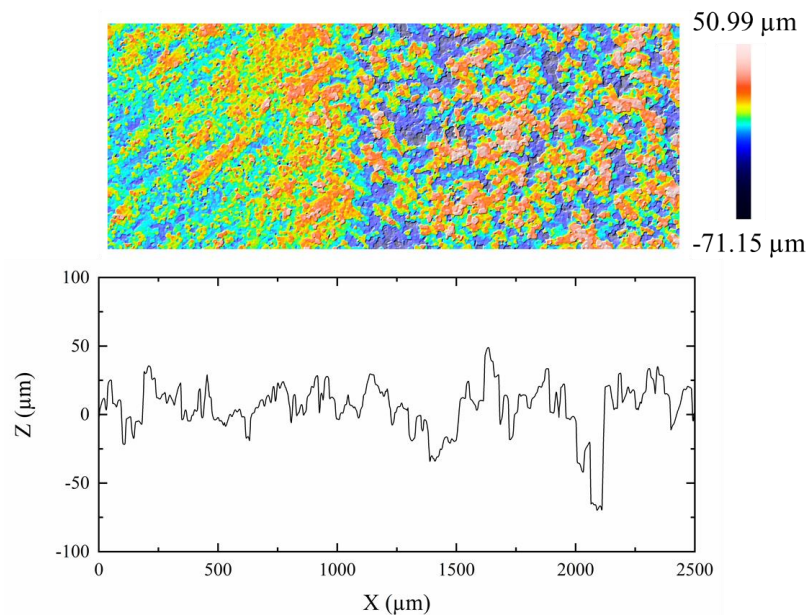


Figure 4.4. Connection area of permeable and dense structures of an additively manufactured test specimen.

#### 4.1.2 Ceramic coating

In order to avoid metal diffusion from the metallic substrate to the palladium membrane which would downgrade membrane performance, a diffusion barrier layer (DBL) made of Ytria Stabilized Zirconia (8YSZ) between the metallic substrate and the palladium membrane was fabricated [9]. The experiments for ceramic coating were carried out in the Institute for Energy and Climate Research 1 at the Research Center Jülich (*IEK-1 at FZJ*) by Masoud Mahmoudizadeh and Dongxu Xie. The experimental procedures refer to the master thesis of Paul Kant [186]. Many coating parameters will influence the membrane quality, e.g., sintering time, surface roughness of the substrate, sintering temperature, etc. [187]. This work focused on the impact of different membrane substrates on the membrane quality rather than on the other parameters. Therefore, the coating procedure and the sintering parameters for both additively manufactured and conventional test specimen were the same. However, due to the roughness of additively manufactured test specimen has a higher roughness than conventional test specimen, a new coating procedure adapted additively manufactured test specimen need to be developed in future.

The suspension for ceramic dip coating contains 8YSZ-nanoparticles (*Tosoh*),

dibasic ester (*LEMRO GmbH & Co. KG*), ethylcellulose (*Sigma Aldrich*), Nuospere FX9086 (*Elementis Specialties*) and Tego Airex 931 (*Evonik Industries*). For the ceramic coating of the test specimen shown in Fig. 4.2, 100g of 8YSZ-nanoparticles was sufficient. The exact mass of the different components is listed in Table 4.1. After mixing in a tumble mixer, the suspension was ready for dip coating.

Table 4.1 Mass of components for the dip coating slurry

Component	Mass (g)	Mass fraction (%)
8YSZ-nanoparticles	100.0	38.2
Dibasic ester	148.9	56.9
Nuospere FX9086	5.0	1.9
Ethylcellulose	5.1	1.9
Tego Airex 931	2.6	1.0

Before the coating process, the welding seam area of the conventional test module was smoothed by sand blasting (2.5 bar, F150 corundum grit). The additively manufactured test module did not undergo any smoothing process. Then the area of the test specimen not to be coated was masked by adhesive tape.

A DX2S-500 dip coater (*KSV NIMA*) was used for the ceramic coating process. The coating process was carried out in a clean room. Fig. 4.5 shows the additively manufactured test specimen after dip coating.

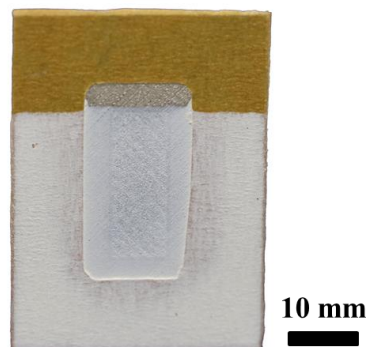


Figure 4.5. Additively manufactured test specimen after dip coating.

The parameters of the dip coating are listed in Table 4.2.

Table. 4.2 Parameters of the dip coating.

Parameter	value
Immersion speed	100 <i>mm/min</i>
Hold time (down)	10 <i>s</i>
Withdrawal speed	100 <i>mm/min</i>
Immersion depth	~42 <i>mm</i>

The test specimen were dried after dip coating drying at room temperature for 12 hours, then they were placed at 40 °C in a drying oven for another 6 hours. After the drying process, the adhesive tapes were peeled off and the coated specimens were placed into a sinter oven under argon atmosphere (*Thermal Technology GmbH*) for heat treatment. The oven was heated up to 600 °C with 5 K/min and the temperature was held for 30 min. Then the oven was further heated up to 1100 °C with 5 K/min and held at that temperature for 180 min. Finally, the oven was cooled down to room temperature with 5 K/min.

The conventional and additively manufactured test specimens before and after ceramic coating are shown in Fig. 4.6. Fig. 4.6 (a) shows the welding seam of the conventional specimen. Here, the left area is the permeable substrate and the right area is the dense frame. The weld seam is around 1.17 mm wide and can be seen between the permeable substrate and the dense frame. Fig. 4.6 (b) shows the additively manufactured specimen before ceramic coating. Here, the left area is the permeable substrate and the right area is the dense frame. After the ceramic coating, a defect on the welding seam area can be seen in Fig. 4.6 (c). The main reason for such defects is the height gap between the welding seam and the other area. As shown in Fig. 4.6 (d), there are no such defects visible on the additively manufactured test specimen. However, the ceramic layer is not thick enough to cover the permeable surface. Parameters for thicker ceramic layers should be investigated for additively manufactured test specimen in the future. After ceramic coating, the roughness of the conventional test specimen got decreased from 1.36  $\mu\text{m}$  to 0.83  $\mu\text{m}$  while the roughness of the additively manufactured test specimen got reduced from 11.53  $\mu\text{m}$  to 9.96  $\mu\text{m}$ . Hence, both test specimen were smoothed

by the ceramic layer, and this may influence the quality the of palladium membrane.

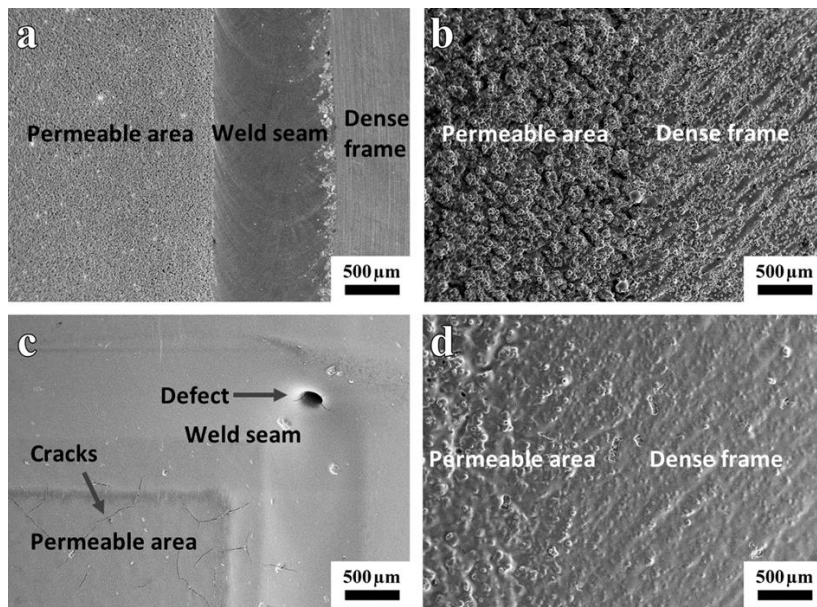


Figure 4.6. (a) Conventional test specimen before ceramic coating; (b) Additively manufactured test specimen before ceramic coating; (c) Conventional test specimen after ceramic coating; (d) Additively manufactured test specimen after ceramic coating.

From the above experimental results, high surface roughness leads to many small cracks on the surface after sintering. To obtain a better surface quality, a feasible way is to decrease the surface roughness. A *Deckel Fp3a* milling machine with *Dialog11 System* was used to smooth the surface of additively manufactured test specimen. An endmill with 16 mm diameter operated at 1400 rpm and a feed of 60 mm/min was used in the milling procedure. For easy clamping, a test specimen with 2 mm thickness was used in this smoothing treatment.

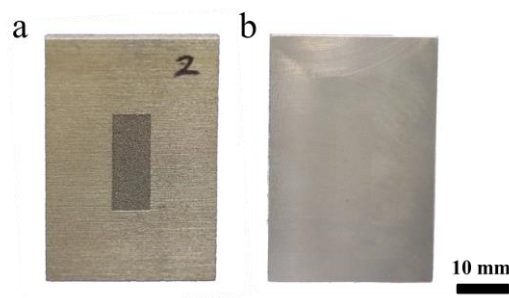


Figure 4.7. (a) Additively manufactured test specimen before (a) and after (b) smoothing treatment.

Fig. 4.7 (a) shows the test specimen before the treatment. Permeable substrate and dense frame can be seen clearly in the figure. Fig. 4.7 (b) shows the specimen after smoothing treatment. The permeable substrate became blurry in the figure.

Fig. 4.8 shows the 3D profile of the additively manufactured test specimen after the smoothing treatment. The left area is the dense frame, and the right area is the permeable substrate. Gaps between the laser tracks can be seen in the figure. The pores have not been closed by the milling procedure. From the height measurement, both dense frame and permeable substrate stand in the same height. The roughness of the additively manufactured test specimen after this smoothing treatment was  $1.36\ \mu\text{m}$ , which is even lower than for the conventional test specimen. From this, a better ceramic layer on the additively manufactured test specimen could be expected after the smoothing treatment. Further research about the ceramic coating and the palladium coating on additively manufactured test specimen after smoothing treatment will be carried out in the future.

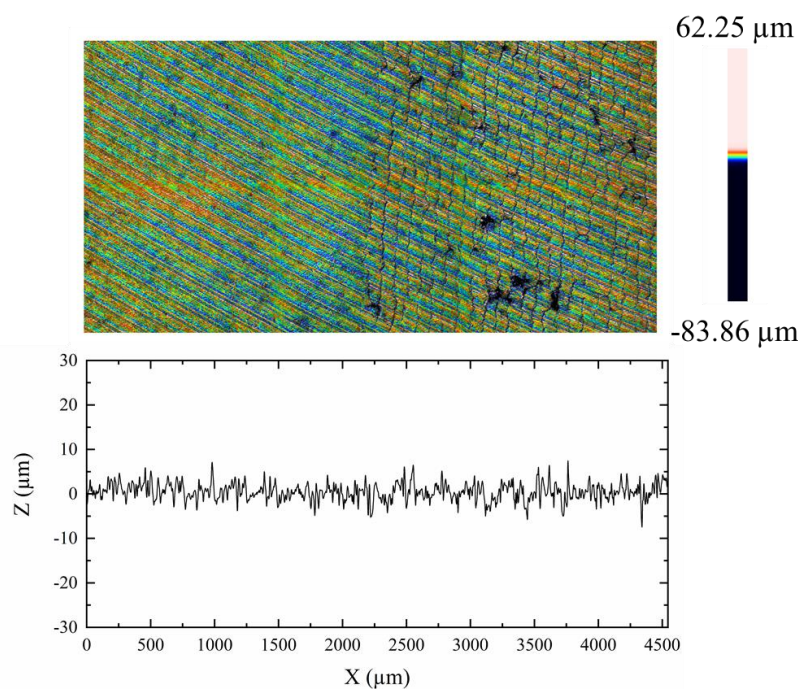


Figure. 4.8. 3D profile of test module after smooth treatment.

#### 4.1.3 Palladium membrane substrate plate (PMS plate)

The additively manufactured test specimens showed the potential of additively manufactured permeable-dense composites as a membrane substrate. Boeltken et al. in IMVT presented a compact modular microstructured membrane reactor for

methane steam reforming [9]. The development of an additively manufactured membrane substrate for this reactor design could be a good option for further application. On the one hand, an additively manufactured membrane substrate could improve the quality of the ceramic interlayer and the palladium membrane. On the other hand, an additively manufactured membrane substrate with internal channels could make the microreactor even more compact and improve its efficiency. However, the required size of the membrane substrate is much bigger than for the former test specimen. The residual stresses in an additively manufactured permeable-dense composite may cause membrane substrate bending [188]. Therefore, the scan strategy of an additively manufactured PMS plate needed to be studied.

Fig. 4.9 shows the schematic of the dense frame of the PMS plate. The centered empty area will be filled with permeable material. The steam reformer is composed of three modules: combustion module, reforming module and hydrogen separation module. Each module consists of several metal plates [189]. In a first step, the microstructured plates are fabricated by etching, micromachining and lamination [190]. Only the palladium membrane substrate is fabricated by 3D printing. This combination of different manufacturing techniques allows to utilise the advantages of different techniques to develop the next generation of the steam membrane reformer.

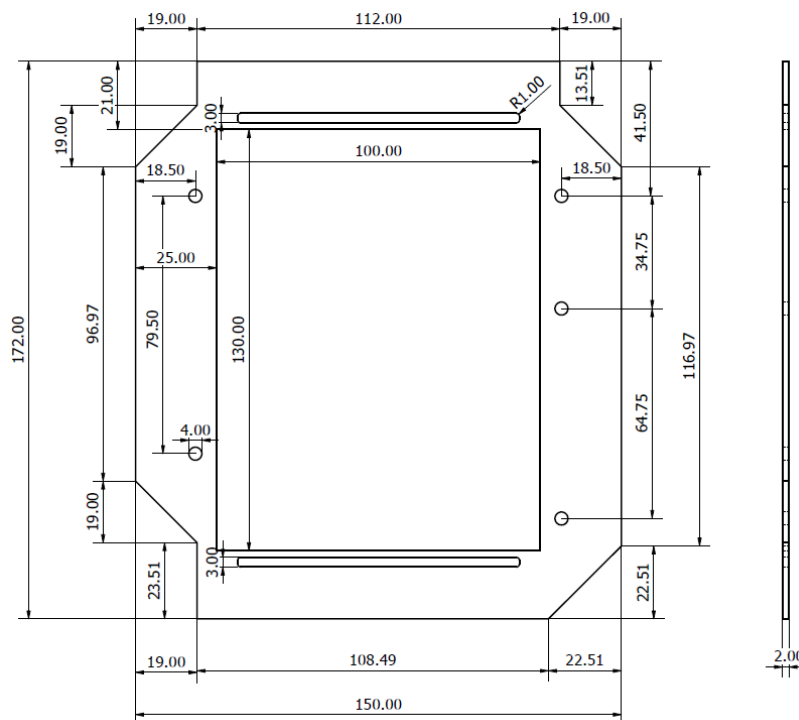


Figure 4.9. Schematic of the PMS plate.

Fig. 4.10 shows the printing job of a PMS plate in the ReaLizer SLM125 operating system. Since the length of the build plate of the ReaLizer SLM 125 is 125 mm, as shown in Fig. 4.10, a PMS plate with 150 mm width must be placed diagonally on the build plate. There is a 5 mm distance between the PMS plate and the build plate for support structures. The green centered area is the permeable part acting as a membrane substrate, and the red boundary area is the dense part acting as a sealing structure of the hydrogen separation module.

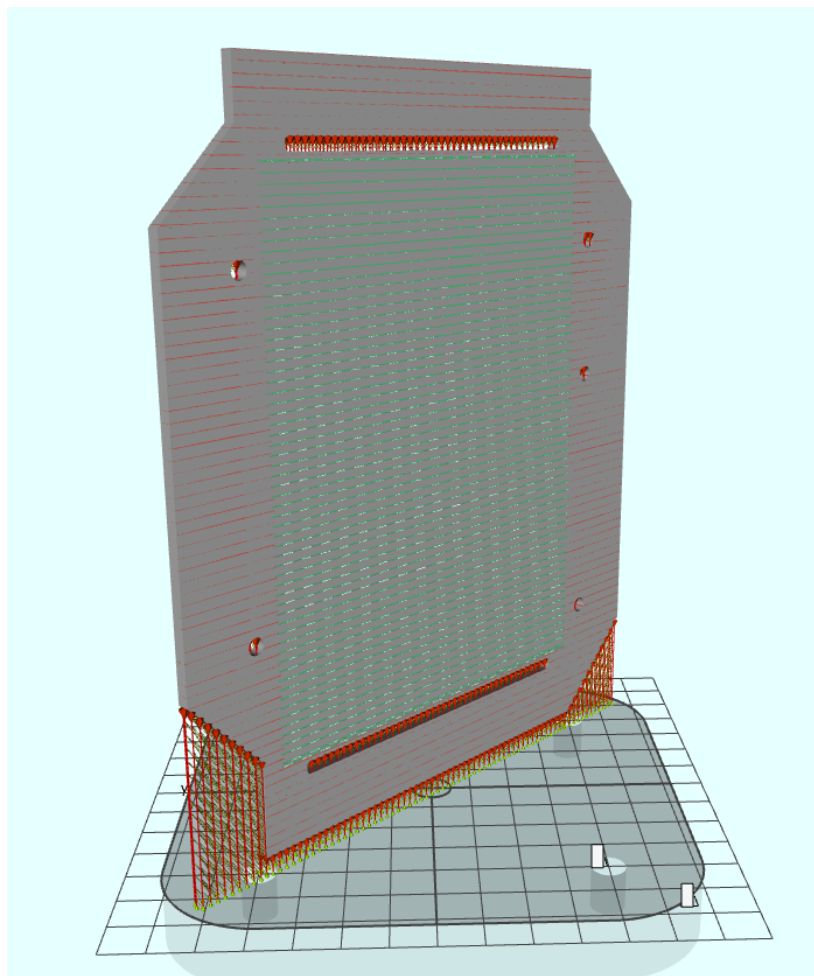


Figure 4.10. The printing job of a PMS plate in the ReaLizer SLM125 operating system.

Fig. 4.11 shows an additively manufactured 2 mm thick PMS plate. The residual stress caused thermal warping of the PMS plate. Its left area is out of shape, and one possible reason is that the support structures are not strong enough. However, the test specimen with similar structures did not show warp. Liu et al. indicates that longer laser track create larger residual stress [191]. This is the reason why the same

laser parameters and scan strategy in case of the test specimen created no warp.



Figure 4.11. Additively manufactured 2 mm thick PMS plate created with the same laser parameters and scan strategy like the test specimen in figure 4.2.

In order to avoid the thermal warping of the PMS plate, a 5 mm thick PMS plate was printed. As shown in Fig. 4.12, the 5 mm thick PMS plate did not show obvious thermal warping. This result shows that increasing the thickness of the plate is an effective way to avoid thermal warping of planar samples in LB-PBF.



Figure 4.12. Additively manufactured 5 mm thick PMS plate.

Fig. 4.13 shows the 3D profile of additively manufactured 5 mm thick PMS plate. The left area is the dense frame, and the right area is the permeable substrate. The gaps between the laser tracks can be seen in the permeable area. From the height measurement, since the permeable scan strategy has no boundary scan vectors, the height of the permeable surface is lower than that of the dense surface. This step between permeable and dense structure may degrade the ceramic interlayer or palladium membrane quality. Therefore, the scan strategy for a permeable-dense composite needs to be optimized. The successful preparation of a 5 mm thick PMS plate shows that it is feasible to fabricate a PMS plate with LB-PBF. However, a thinner PMS plate is more suitable for the microreactor for reasons of material use, resistance against gas transport and compactness. With this in mind, a PMS plate with internal channels was developed where the wall between the external surface

and the internal channels would be minimised without compromising the bending strength of the structure.

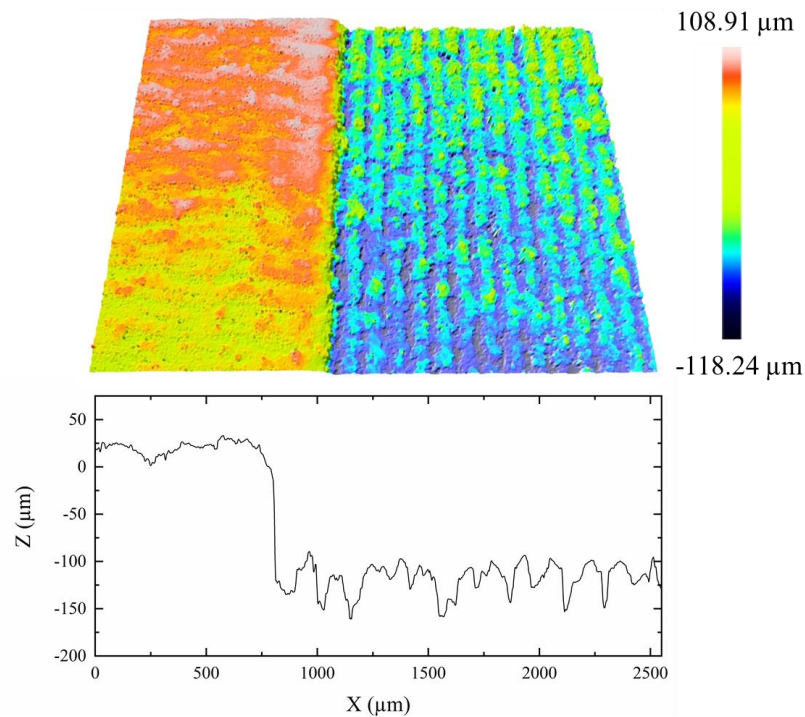


Figure 4.13. 3D profile of an additively manufactured 5 mm thick PMS plate.

Fig. 4.14 shows the schematic of the dense frame for a 3 mm thick PMS plate after geometry optimization. The additively manufactured test specimen and the 5 mm thick PMS plate show two methods to avoid the influence of residual stress: decrease the sample size and increase the thickness. During the laser melting process, periodic thermal expansion and contraction that exceed the maximum elastic strain of the material will cause heterogeneous plastic strain and generate internal stress, which can reach the yield stress of the material and may cause bending due to internal stress [188]. Both methods avoid that the material reaches its maximum elastic strain. A 3 mm thick PMS plate based on this idea was designed and is shown in Fig. 4.14. Several 2 mm holes are included in the dense frame. Different from the 5 mm thick PMS plate, the permeable substrate is not fully filled with permeable material. Instead a 1 mm thick dense base with 2 mm  $\times$  2 mm quadratic channels was designed as the base of the permeable substrate. During the printing process, a 1 mm thick permeable wall will cover this area. There is 0.5 mm overlap between the permeable material and the internal channels. This overlap was designed for enhancing the connection between the permeable substrate and the

dense frame. However, this overlap may not be necessary for a permeable-dense composite. Therefore, a PMS plate with 0.5 mm thick permeable material could also be possible in the future.

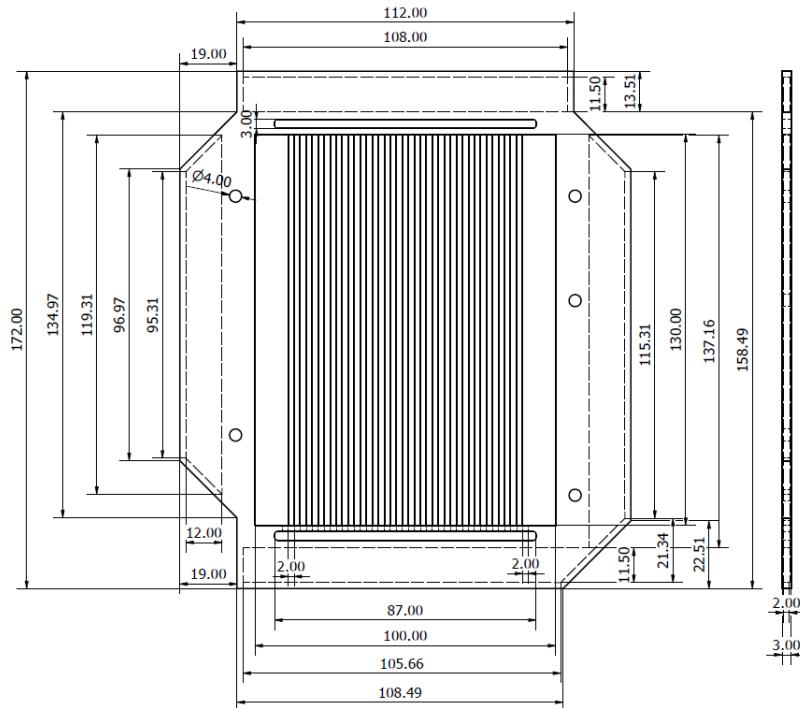


Figure 4.14. Schematic of a 3 mm thick PMS plate after geometry optimization.

Fig. 4.15 shows the print job of the dense frame for the 3 mm thick PMS plate. The dense frame was sliced into many pieces. The yellow part in the printing job is the support structures designed by the ReaLizer SLM 125 operating system. Wang et al. indicated that the support structure can prevent the deformation of material by residual stress [192]. All the holes and channels of the dense frame are filled with these support structures.

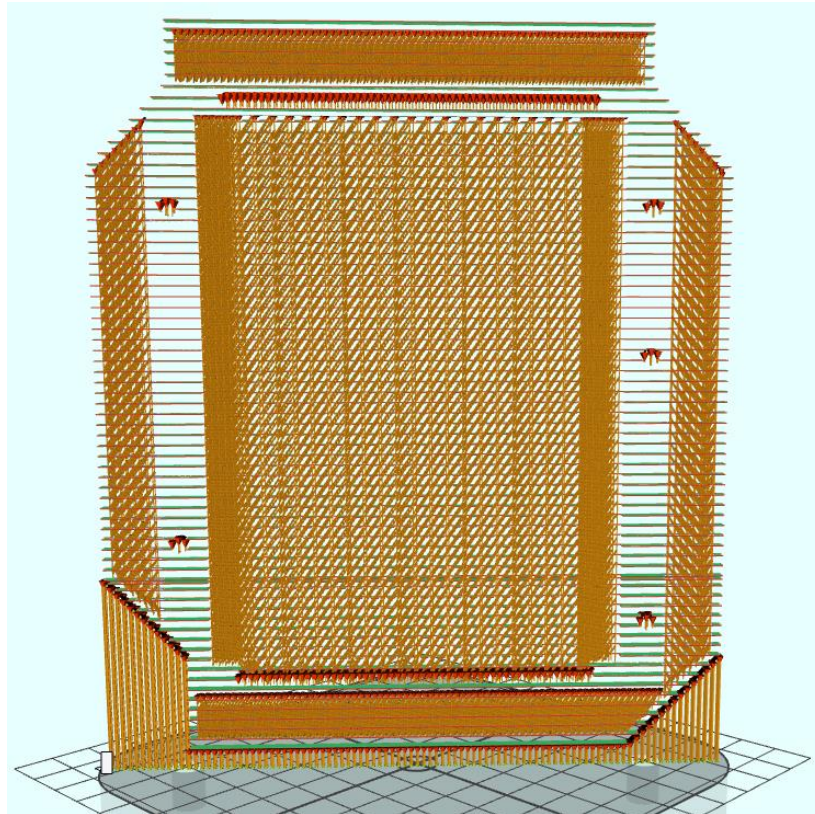


Figure 4.15. The printing job of the dense frame for the 3 mm thick PMS plate after geometry optimization in the ReaLizer SLM125 operating system.

Fig. 4.16 (a) shows the additively manufactured 3 mm thick PMS plate. After geometry optimization, the surface of the 3 mm thick PMS plate keeps flat. One possible reason is that the holes and channel structures reduce the residual stress. Another possible reason is that the support structures improve the resistance against deformation. The internal channels and the support structures in the internal channels can be seen in the Fig. 4.16 (b). With these internal channels, the membrane reformer could be more compact. The support structures in the internal channels on the one hand prevent the deformation of the PMS plate: On the other hand, these support structures may also hinder the flow of hydrogen and cause a larger pressure drop. Therefore, a PMS plate without support structures in the internal channels could be pursued in future research.

Fig. 4.16 (c) shows the back side of the PMS plate. All the back surface is fabricated by dense material. The hydrogen flow won't pass this wall and get to the other side of the PMS plate. After passing through the palladium membrane, the ceramic interlayer and the permeable wall underneath, the hydrogen flow will flow along the

internal channels and leave the module at the open side. With this design, fewer structured plates are needed to collect the produced hydrogen compared to the original design.

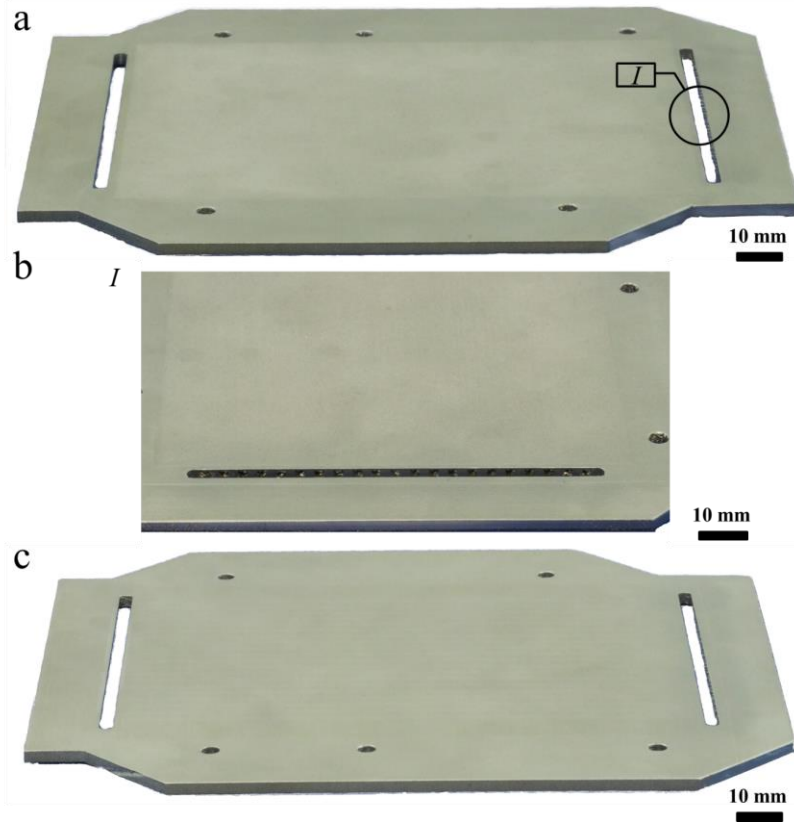


Figure 4.16. (a) 3 mm thick PMS plate after geometry optimization; (b) Internal channels of the PMS plate; (c) Back side of the PMS plate.

Fig. 4.17 shows the 3D profile of the 3 mm thick PMS plate. The left area is the dense frame, and the right area is the permeable substrate. As shown in the height measurement, the dense frame and the permeable substrate stand in same height. Compared to the 5 mm thick PMS plate, not only the structure of the PMS plate was optimized but also the hatch offset of the permeable material was optimized as discussed in chapter 2.5. With the flat surface between the dense frame and the permeable substrate, a better ceramic layer quality could be expected.

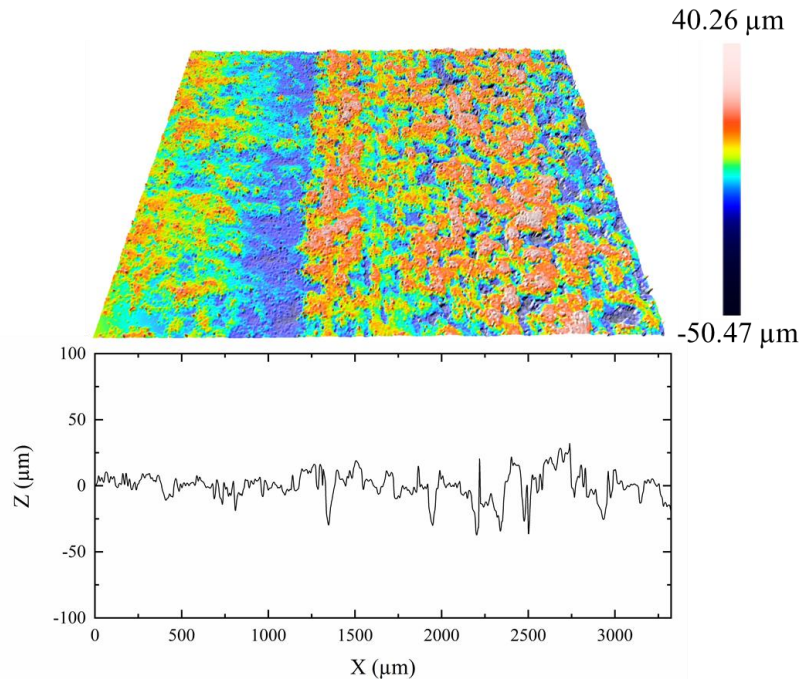


Figure 4.17. 3D profile of a 3 mm thick PMS plate after structure optimization.

#### 4.1.4 Tubular palladium membrane substrates (PMS pipe)

In addition to planar systems, tubular designs are likewise often used in palladium membrane reactors. Straczewski et al. presented a palladium membrane based on large porous 310L tubes [193]. Tong et al. developed a thin Pd-Ag membrane on an asymmetric porous stainless steel tube for hydrogen production from methane steam reforming. 80.72% methane conversion were achieved at lower temperature of 773 K and a pressure of 500 kPa [194].

Fig. 4.18 shows the cross section of different potential PMS pipes. The ends of all PMS pipes are composed of a 20 mm long dense sealing structure, and the middle parts is composed of a 100 mm long permeable structure acting as membrane substrate. The outer diameter of the PMS pipes is 10 mm, the inner diameter is 6 mm. 4 kinds of PMS pipes with different cross section were prepared for coating with a ceramic interlayer and the palladium membrane. In order to increase the specific surface area, PMS pipes with gear shaped cross section were designed considering that the angle of the gear teeth may influence the quality of the interlayer and membrane coatings. Therefore, PMS pipes with  $140^\circ$ ,  $160^\circ$ , and  $180^\circ$  gear teeth angle were designed.

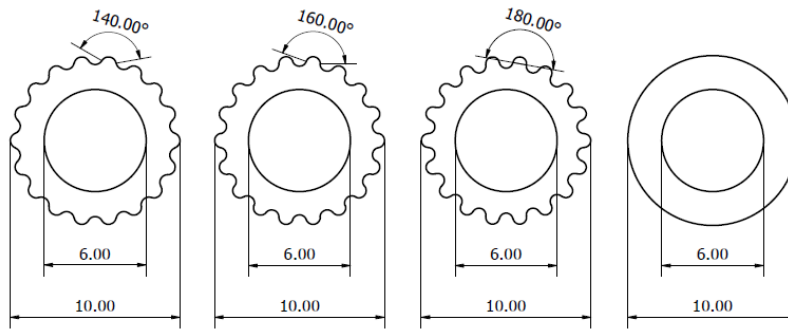


Figure 4.18. Schematic of different tubular palladium membrane substrates.

As discussed in chapter 3.1.3, permeable tubes printed by FDOSV show the best surface quality compared to other scan strategies. However, FDOSV cannot be designed in the ReaLizer SLM 125 operating system directly. The parts printed by FDOSV should be divided into four pieces in the CAD model, and each part has 0.5 mm to 1 mm overlap with the adjacent parts. Then, these four parts will be filled by unidirectional scan vectors in the ReaLizer SLM 125 operating system. However, components with complex structures are difficult to divide. Feasible scan strategies are RSV and FDCSV. As discussed in section 3.1.2  $60^\circ$  RSV shows the lowest roughness compared to other rotation angles. Therefore,  $60^\circ$  RSV and FDCSV were used for PMS pipe printing.

Fig. 4.19 shows the PMS pipes printed by  $60^\circ$  RSV. The dense sealing structures can be seen at the end of the PMS pipes. The permeable substrates have the same cross section geometry as the dense sealing structure. From left to right, the gear teeth angle is  $140^\circ$ ,  $160^\circ$ , and  $180^\circ$ , respectively. The magnified figures show the connection areas of the dense sealing structures and the permeable substrates. From the magnified figures, the dense sealing structures show a smoother surface than the permeable substrates. The step structures can be seen on the permeable substrates.

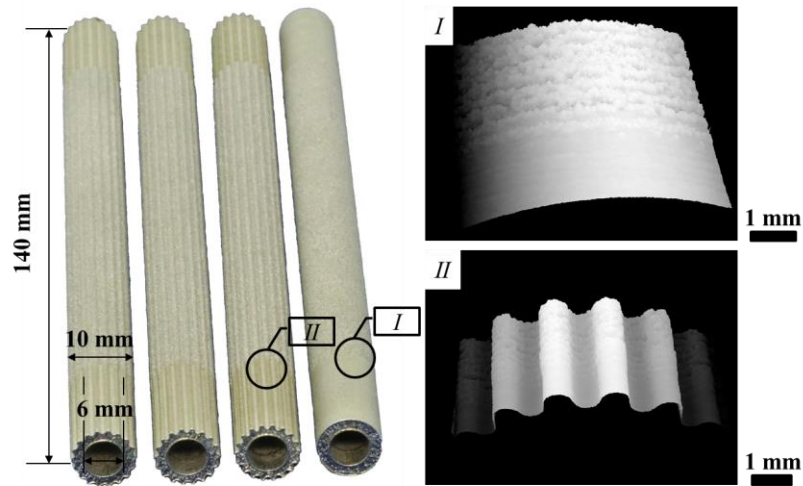


Figure 4.19. PMS pipes printed by 60° RSV.

Fig. 4.20 shows the 3D profile of the PMS pipes printed by 60° RSV. From the height measurement, the length of each step is around 300  $\mu\text{m}$  which fits the prediction of chapter 3.1.2. This measurement results implies the previous conclusion is correct that the step structures are composed of the initial points and terminal points of the scan vectors.

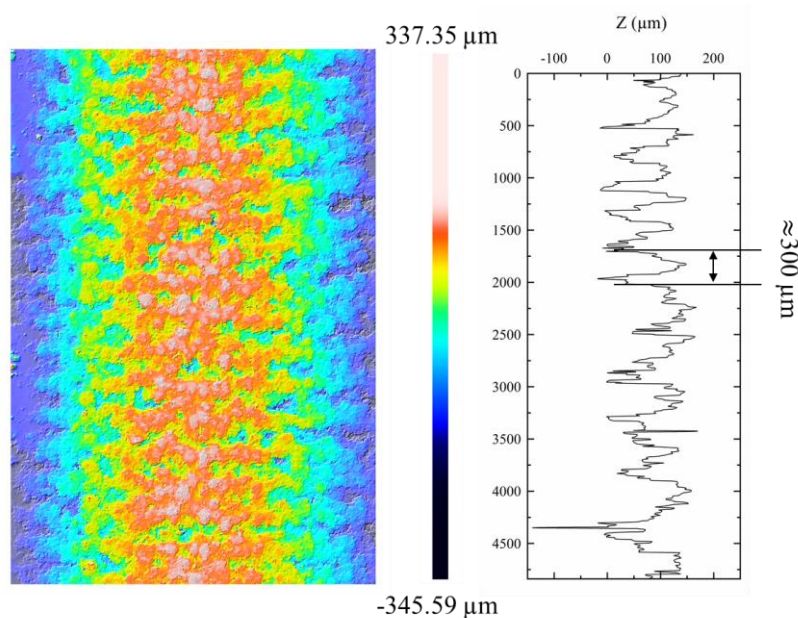


Figure 4.20. 3D profile of PMS pipe printed by 60° RSV.

Fig. 4.21 shows the PMS pipes printed by PDCSV. The dimensions of these PMS pipes are the same as for the PMS pipes printed by RSV. Grooves on the permeable

substrate between the scan vectors in different directions can be seen in Fig. 4.21. From the magnified figures, both gear shaped PMS pipes and normal PMS pipes have these grooves structures.

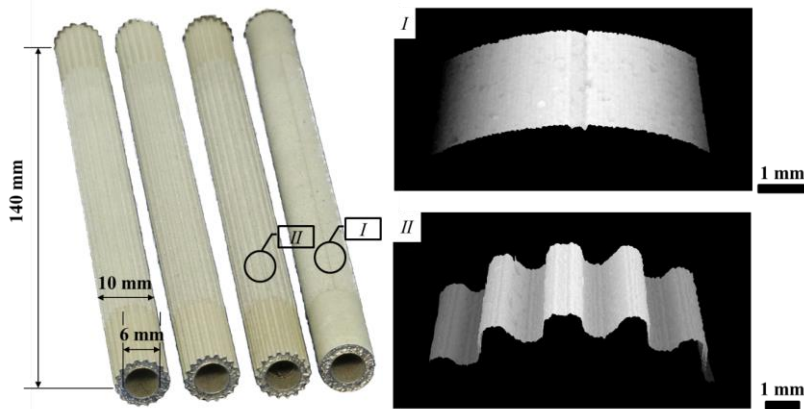


Figure 4.21. PMS pipes printed by FDCSV.

Fig. 4.22 shows the 3D profile of the PMS pipes printed by FDCSV. The height measurement of the grooves shows the depth is around  $100\ \mu\text{m}$ . There is a  $200\ \mu\text{m}$  gap at the right side of the grooves. This measurement result agrees with the results in chapter 3.1.3. It shows that the previous conclusion is correct that the gap is composed of the terminal points of the scan vectors. Since the terminal point is affected by lack of powder and imprecise positioning, the gap composed of the terminal points of the scan vectors appears on the right hand side of the groove. The connection vectors are arranged alternately opposite, so that the direction of the second scan vector is always opposite to that of the first. Due to the hatch distance of  $100\ \mu\text{m}$ , the gap width is  $200\ \mu\text{m}$ .

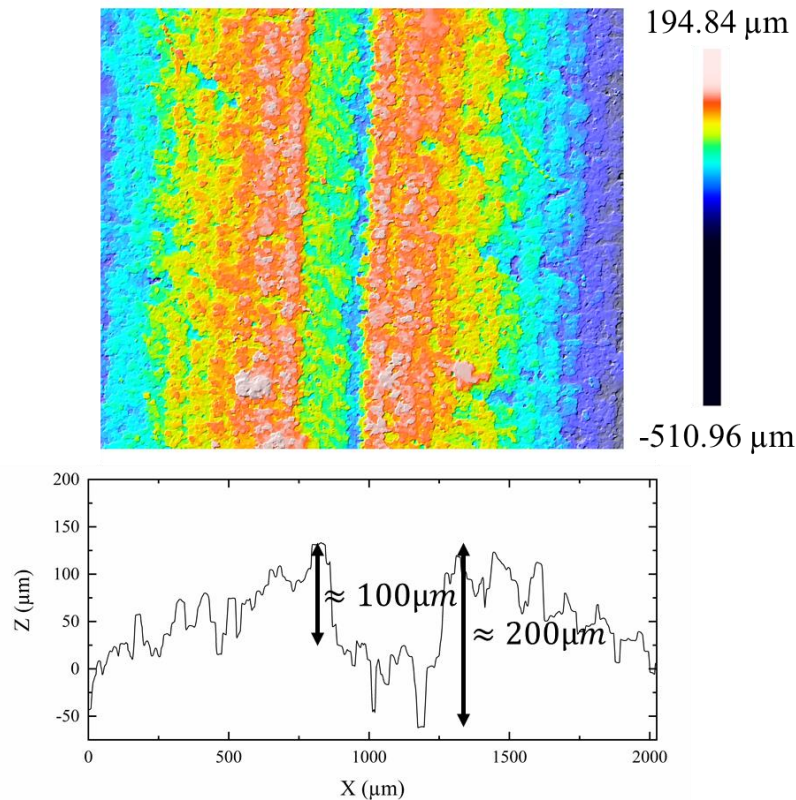


Figure 4.22. 3D profile of a PMS pipe printed by FDCSV.

## 4.2 Additively manufactured microstructured reactor

### 4.2.1 Additively manufactured micro channels

The term microchannels with a view to a microreactor refers to flow structures enabling the use of so called microeffects arising whenever the lateral dimensions of a channel are in the range or smaller than the boundary layer thickness of the fluid flow[195]. IMVT presented an ultra-compact microreactor where the microchannels were fabricated by wet chemical etching. The dimension of these channels were  $500\ \mu\text{m}$  (width)  $\times$   $300\ \mu\text{m}$  (depth)  $\times$   $50\ \text{mm}$  (length) [9]. In principle, LB-PBF could also be used to manufacture in one step an entire microreactor body. For this it is important to know whether the resolution of LB-PBF is good enough to obtain sufficiently precise microchannels of the required size. A plate with microchannels was therefore prepared for dimension measurements. Fig. 4.23 shows the schematic of this microstructured plate. As shown, width and depth of the microchannels is the same as for the previous microreactor presented by IMVT.

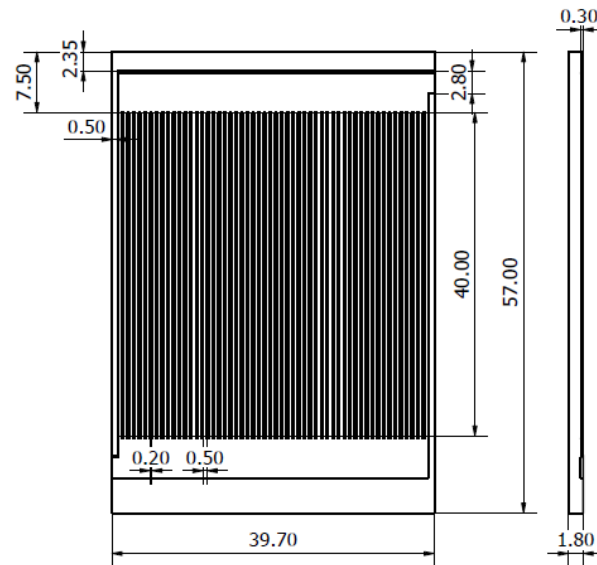


Figure 4.23. Schematic of an additively manufactured microchannel plate.

Fig. 4.24 shows the additively manufactured plate with microchannels. The thickness of the plate is 1.8 mm. The residual stress didn't cause a deformation of the plate.

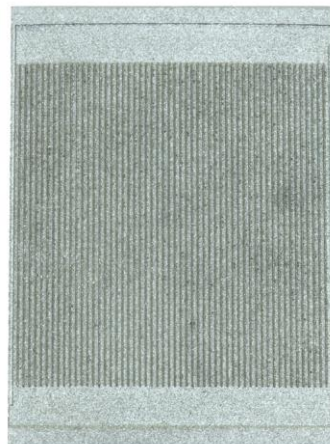


Figure 4.24. Additively manufactured plate with microchannels.

Fig. 4.25 shows the 3D profile of the microchannels. From the height measurement, the width of the microchannels is around 500  $\mu\text{m}$  and the depth is around 300  $\mu\text{m}$ . The obtained dimensions of the microchannels fit the CAD model well and satisfy the requirements of the microreactor design.

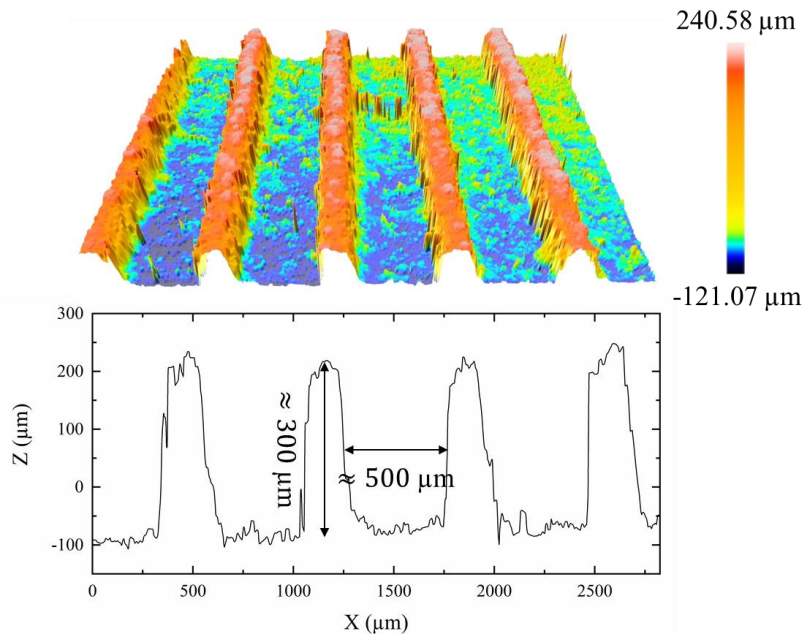


Figure 4.25. 3D profile of the additively manufactured microchannel plate.

3D printing of microchannels with porous walls is a new research direction in microreactors. Zheng et al. developed a novel additive manufacturing method for a porous catalyst support for methanol steam reforming which reached a high catalyst loading [196]. Properly designed porous structures may enable even higher catalyst loadings. Fig. 4.26 shows an additively manufactured microstructured plate where bottom and side walls were made by dense material, the microchannel were made by porous material. The width of the microchannels is  $1000\ \mu\text{m}$ , the depth is  $500\ \mu\text{m}$ . The porous microchannels are covered by a dense body. The handle structures at the left and right were designed to clamp the additively manufactured reactor. From Fig. 4.26, the plate shows no deformation.

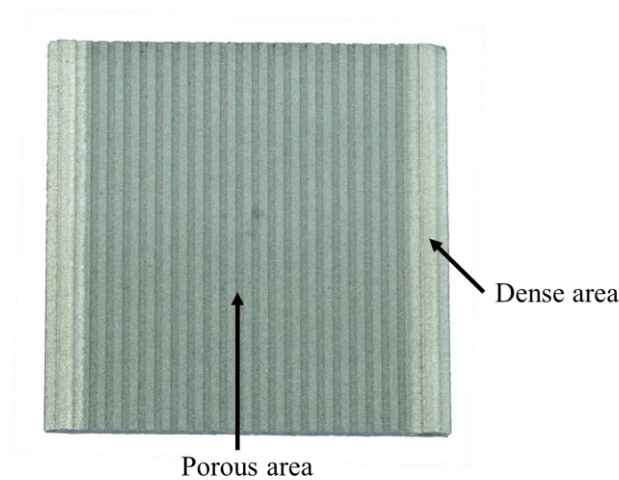


Figure 4.26. Additively manufactured plate with porous microchannels.

Fig. 4.27 shows the 3D profile of the additively manufactured porous microchannels. As shown in the height measurement, the dimensions of the porous microchannel fit the design.

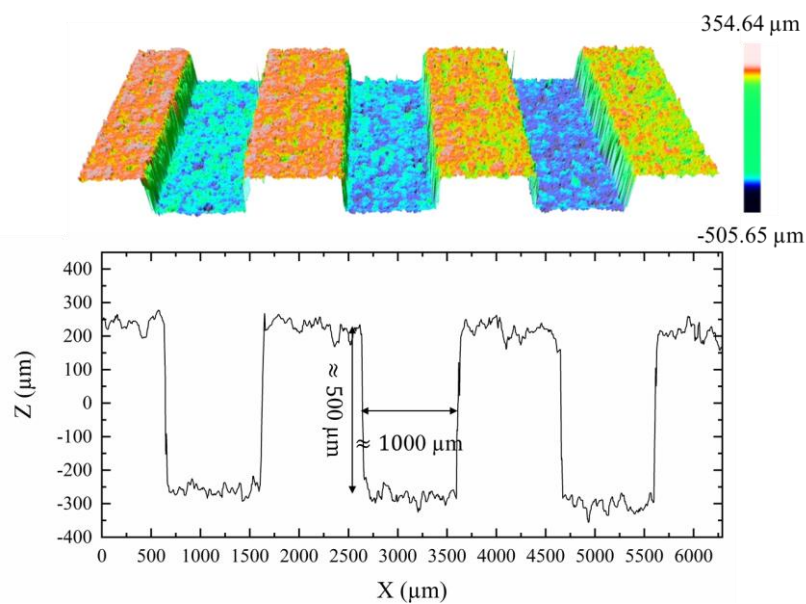


Figure 4.27. 3D profile of the additively manufactured porous microchannel.

#### 4.2.2 Additively manufactured microstructured reactor design

Additively manufactured reactors are receiving increasing attention in flow chemistry and chemical process engineering. Scotti presented a miniaturised polypropylene reactor by fused deposition modeling [197]. Kazenwadel et al. developed an additively manufactured modular reactor system in KIT. PH controlling modules and enzyme transformation modules were printed for enzyme

cascades testing [198]. However, most of reactors so far were prepared by Stereolithography (SLA) and Fused Deposition Modeling (FDM). The working temperature of a reactor is obviously limited by the material choice, e.g., the melting temperature of polypropylene, which is one of the suitable materials for FDM is 208 °C [199]. Compared to FDM and SLA, reactors printed by LB-PBF enable larger working temperature ranges and also chemically more aggressive media. Former research developed the additively manufactured permeable material as palladium membrane substrate and microchannels made by porous-dense material. Based on these, an additively manufactured steam reformer can be developed in future. Due to the feature of additive manufacturing, many advantages can be expected from additively manufactured reactor e.g., reducing the investigate time of new reactor, high efficiency with optimization of reactor structure. However, up to now, far too little attention has been paid to additively manufactured metallic reactors. The feasibility of additively manufactured metallic reactors needs to be verified. Hence, the primary aim of this final section is develop a method of design and fabricate an additively manufactured reactor.

Fig. 4.28 shows the schematic of an additively manufactured test reactor. Channels with different cross section shape and dimension were designed in the test reactor. A temperature barrier layer with temperature barrier structures and cooling water was designed to separate the temperature in different parts of the reactor. The temperature at different positions of the reactor can be detected by thermocouples. With temperature barrier structures, the temperature of the reactants will drop after flowing out of the reaction zone, which prevents the reaction from continuing, thereby improving safety performance [200].

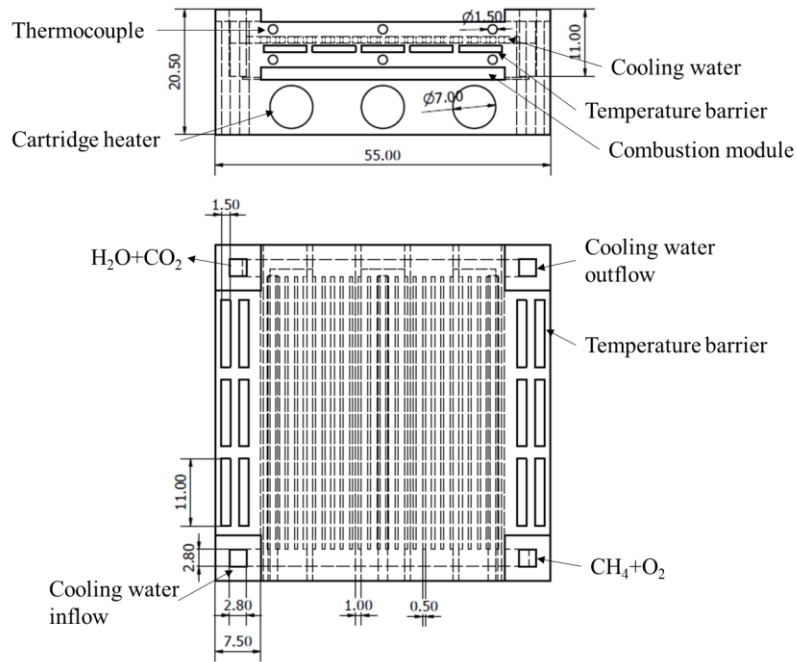


Figure 4.28. Schematic of an additively manufactured test reactor.

There are a lot of internal microchannels in this temperature barrier test reactor. The support structures inside the microchannels may impede the flow through them. To avoid the influence of support structures, a  $90^\circ$  design strategy and a  $45^\circ$  printing strategy is proposed here.  $90^\circ$  design strategy means the structures are always parallel or vertical to the build plate. When the CAD model is transported into the ReaLizer operating system, the model is rotated by  $45^\circ$ . This is the  $45^\circ$  printing strategy. With this design and printing strategy, all the structures are inclined by  $45^\circ$  relative to the build plate. In that case there are no internal support structures necessary inside the reactor. Fig. 4.29 shows the cross section of the  $90^\circ$  designed temperature barrier test reactor printed by  $45^\circ$  printing strategy. The cooling water channels and temperature barrier layer without support structures can be seen in Fig. 4.29. During the printing process, the laser energy was too high so that the wiper broke. The deformation caused by the broken wiper can be seen in Fig.4.29. The laser parameters for achieving dense material need further research.

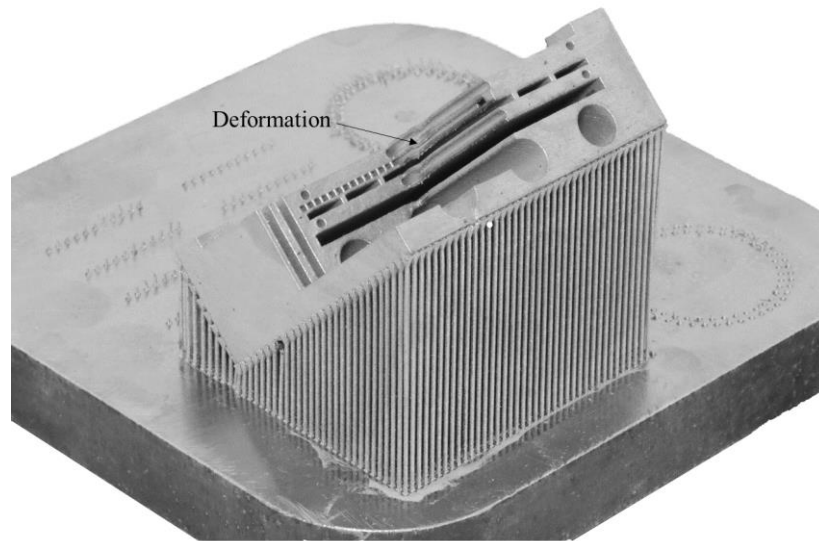


Figure 4.29. Temperature barrier test reactor printed by 45° printing strategy.

Fig. 4.30 shows the 3D profile of a thermocouple hole. When the angle between overhanging surface and build plate is too low, the surface roughness will increase massively [201]. With 45° printing strategy, the angle between the overhanging surface and the build plate is always 45°. Therefore, the thermocouple hole shows a well defined circular shape.

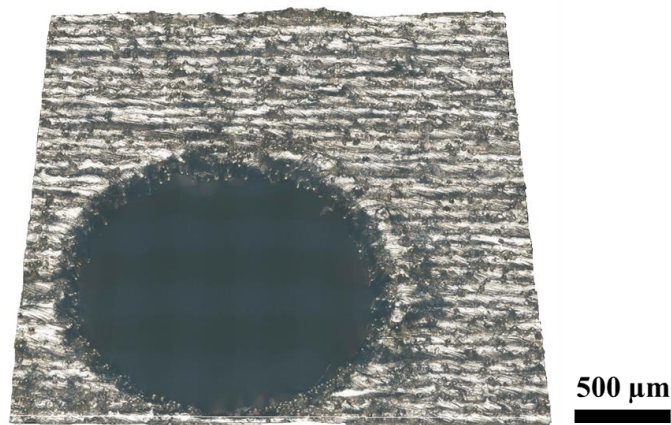


Figure 4.30. 3D profile of a thermocouple hole in the additively manufactured reactor.

Fig. 4.31 shows the additively manufactured temperature barrier test reactor with a microchannel plate. The microchannel plate coated with combustion catalyst and the reactor can be easily assembled. Then, the boundary between plate and reactor

should be sealed by laser welding.



Figure 4.31. Additively manufactured temperature barrier test reactor with microchannel plate.

As shown in Fig. 4.32, based on the 90° design strategy, a reactor for methane steam reforming was designed. The combustion module, reaction module and hydrogen module can be printed in one step. There are internal channels between different modules. The exhaust gas of the combustion reaction could cross the reactor with these internal channels and the temperature distribution of the reactor may be more homogenous.

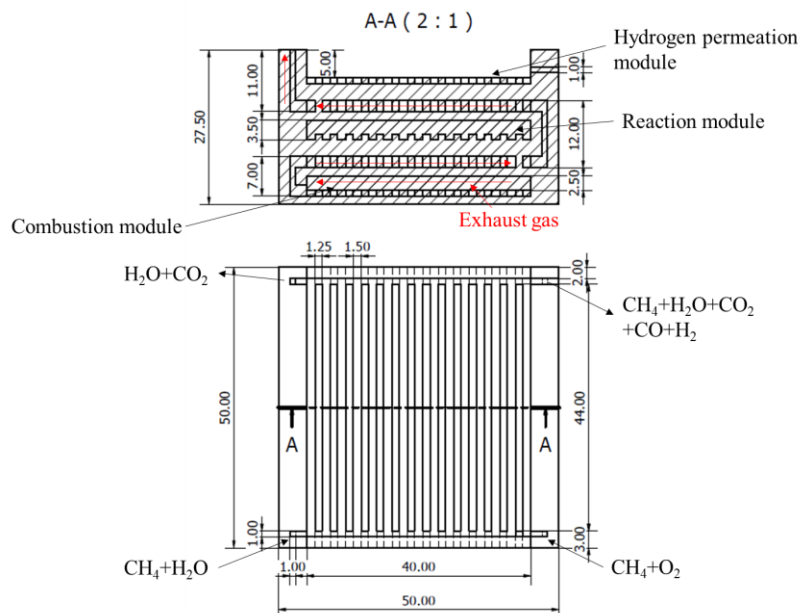


Figure 4.32. Schematic of an additively manufactured reactor for methane steaming reforming.

Fig. 4.33 shows the additively manufactured reactor for steam reforming. The

reactor was printed by 45° printing strategy. The microchannels for the combustion and methane steam reforming reactions can be seen. It can be seen from the 3D profile that the reaction module was formed well by the 45° printing strategy.

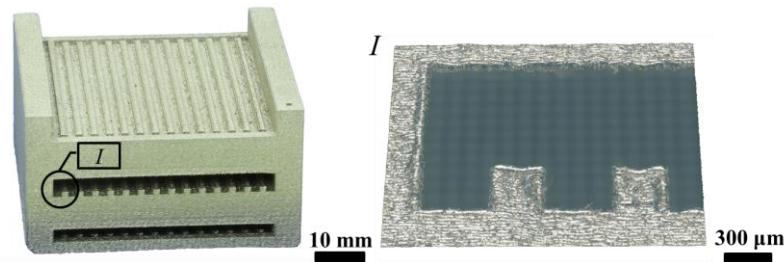


Figure 4.33. Additively manufactured reactor for steam reforming.

### 4.3 Summary and Conclusion

In this chapter, additively manufactured as well as conventionally made test specimens for use as membrane substrates were prepared. The surface morphology of two test specimens before and after coating with a ceramic interlayer was characterized. The morphology of the conventional test specimen has shown that defects can be found on the welding seam between the permeable part and the dense frame. Since there is no welding step for the additively manufactured test specimen, no defects on the boundary of permeable substrate and dense frame could be observed. However, the roughness of the additively manufactured test specimen is much bigger than that of the conventional one. Hence the ceramic layer could not cover the additively manufactured test specimen perfectly. To decrease the roughness of the additively manufactured test specimen, the surface was smoothed by a milling machine. After the smoothing process, the roughness of the additively manufactured test specimen got decreased to 1.36  $\mu\text{m}$  which is similar to that of the conventional test specimen. The coating of smoothed additively manufactured test specimens should be studied in the future.

Additively manufactured PMS plates and pipes for coating with a ceramic interlayer and then a palladium membrane were designed and printed. After structure optimization, a 3 mm thick PMS plate with internal channels was prepared. The 3D PMS plate may increase the performance of the membrane reformer and make it even more compact.

Additively manufactured plates with microchannels were prepared. The dimension of the microchannels were 500  $\mu\text{m}$  (width)  $\times$  300  $\mu\text{m}$  (depth). This result shows that

LB-PBF is a potential method to manufacture microstructured devices.

Based on PMS plates and pipes, a 3D printed steam reformer could be expected in future. In order to verify the feasibility of 3D printing microreactors, A 90° design strategy and a 45° printing strategy were proposed for additive manufacturing of an entire reactor body. Based on this strategy, a temperature barrier reactor was designed and printed. With the temperature barrier structure, the safety performance could be improved. A reactor for steam reforming was designed and printed. The exhaust gas crosses the reactor via internal channels, and the distribution of temperature may be more homogenous.

## 5. Summary and Outlook

This dissertation focused on the development of additively manufactured permeable-dense material and its applications in microreactors. The PMS plates and pipes made by permeable-dense material shows potential as the palladium membrane substrate in steam reformer.

The main achievement of the research on permeable material is the systematic study of the correlation between laser scanning parameters and the pore structure of porous material. Samples with different scanning parameters were prepared for pore size measurement, surface roughness measurement, permeability measurement, and morphology characterization. The hatch distance of permeable samples ranges from 0.1 mm to 0.15 mm. With increasing hatch distance, the pore size, porosity, permeability, and surface roughness increase. The laser spot size used for producing permeable samples ranged from 30  $\mu\text{m}$  to 60  $\mu\text{m}$ . With increasing the laser spot size, more not fully molten powder sintered on the surface of the permeable material. There are no significant changes in porosity, the pore size and permeability are decreasing, and the surface roughness is increasing. Different scan strategies were evaluated including scan vectors parallel to the surface and scan vectors vertical to the surface. Two kinds of pores can be seen in the micrographs of samples printed by different scan strategies. The pores within scan tracks are unstable and sensitive to the scan parameters. The pores between tracks are highly related to the hatch distance and laser spot size. The key point of this method is the control of the balling effect. When the hatch distance is smaller than 0.13 mm, a larger laser spot size leads to more not fully molten powder sintering on the surface of the permeable material, and this powder covers the defects of the surface. Therefore, the permeability and pore size decrease as the laser spot size increases. With this method, materials with different pore size and porosity can be printed in one step.

In this dissertation, besides the flat permeable material, the correlation between laser parameter and porous structure of curved permeable material is also studied. Some applications of additively manufactured porous materials may have complex geometry, e.g., injection molds. Therefore, porous samples with curved surface were prepared by different scan strategies. Permeable tubes printed by USV are anisotropic. The front surface has the lowest roughness. The left and right hand

sides show step structures on the surface. Due to the lack of powder, there are many defects on the back surface. There are two spirals on the surface of permeable tubes printed by RSV. One spiral is composed of the initial points of the scan vectors and the other one of the terminal points. There is a gap on permeable tubes printed by FDSV. One reason is the lack of powder at the terminal points of the scan vectors, and another reason is that the positions of the terminal points of the scan vectors are not matched perfectly. A groove created by connection scan vectors can be seen on the permeable tube printed by FDOSV. Compared to other scan strategies, permeable tubes printed by FDOSV have the lowest surface roughness and are isotropic.

The applications of permeable-dense material in microreactor were investigated in this dissertation. An additively manufactured and conventionally made test specimens were produced and evaluated for coating with a permeable ceramic interlayer. The porous substrate of a conventional test specimen was combined with the dense frame by laser welding. The welding seam leads to defects in the ceramic layer. The permeable substrate and dense frame of additively manufactured test specimen are printed in one step. There is no extra welding step here. However, the thin ceramic layer could not cover the rough surface completely. To reduce the roughness, a 2 mm thick test module was printed and smoothed by a milling machine. The roughness after the smoothing treatment was 1.36  $\mu\text{m}$  which is even lower than that of the conventional test specimen. Ceramic coating on the smoothed additively manufactured test specimen should be studied in the future. Further, PMS plates and PMS pipes were printed for different types of microreactors. Based on PMS plates and pipes and porous microchannels, the feasibility of additively manufactured microreactor was preliminarily investigated. A 90° design strategy and a 45° printing strategy were proposed for additive manufacturing of entire microreactors. Based on this design and printing strategy, microreactors with microchannels and internal channels were designed and printed.

Future extension of permeable-dense material will focus on the membrane reactor with PMS plates or pipes membrane substrate. Based on the previous research of IMVT, new ceramic membrane coating and palladium membrane coating on additively manufactured permeable material should be developed. A compact microreactor for steam reforming with additively permeable material as palladium membrane substrate could be expected in future.

## References

- [1] W. Jiejun, L. Chenggong, W. Dianbin, G. Manchang, Damping and sound absorption properties of particle reinforced Al matrix composite foams, *Composites Science and Technology* 63 (2003) 569–574. [https://doi.org/10.1016/S0266-3538\(02\)00215-4](https://doi.org/10.1016/S0266-3538(02)00215-4).
- [2] B. Zhao, A.K. Gain, W. Ding, L. Zhang, X. Li, Y. Fu, A review on metallic porous materials: pore formation, mechanical properties, and their applications, *Int J Adv Manuf Technol* 95 (2018) 2641–2659. <https://doi.org/10.1007/s00170-017-1415-6>.
- [3] X. Wang, S. Xu, S. Zhou, W. Xu, M. Leary, P. Choong, M. Qian, M. Brandt, Y.M. Xie, Topological design and additive manufacturing of porous metals for bone scaffolds and orthopaedic implants: A review, *Biomaterials* 83 (2016) 127–141. <https://doi.org/10.1016/j.biomaterials.2016.01.012>.
- [4] Z. Xie, M. Tane, S. Hyun, Y. Okuda, H. Nakajima, Vibration–damping capacity of lotus-type porous magnesium, *Materials Science and Engineering: A* 417 (2006) 129–133. <https://doi.org/10.1016/j.msea.2005.10.061>.
- [5] P. Bai, T. Tang, B. Tang, Enhanced flow boiling in parallel microchannels with metallic porous coating, *Applied Thermal Engineering* 58 (2013) 291–297. <https://doi.org/10.1016/j.applthermaleng.2013.04.067>.
- [6] T.J. Phelps, A.V. Palumbo, B.L. Bischoff, C.J. Miller, L.A. Fagan, M.S. McNeilly, R.R. Judkins, Micron-pore-sized metallic filter tube membranes for filtration of particulates and water purification, *Journal of Microbiological Methods* 74 (2008) 10–16. <https://doi.org/10.1016/j.mimet.2007.08.005>.
- [7] H. Arora, R. Singh, G.S. Brar, Thermal and structural modelling of arc welding processes: A literature review, *Measurement and Control* 52 (2019) 955–969. <https://doi.org/10.1177/0020294019857747>.
- [8] T. Boeltken, D. Soysal, S. Lee, G. Straczewski, U. Gerhards, P. Peifer, J. Arnold, R. Dittmeyer, Perspectives of suspension plasma spraying of palladium nanoparticles for preparation of thin palladium composite membranes, *Journal of Membrane Science* 468 (2014) 233–241. <https://doi.org/10.1016/j.memsci.2014.06.003>.
- [9] T. Boeltken, A. Wunsch, T. Gietzelt, P. Pfeifer, R. Dittmeyer, Ultra-compact microstructured methane steam reformer with integrated Palladium membrane for on-site production of pure hydrogen: Experimental demonstration, *International*

- Journal of Hydrogen Energy 39 (2014) 18058–18068.  
<https://doi.org/10.1016/j.ijhydene.2014.06.091>.
- [10] C. Klahn, F. Bechmann, S. Hofmann, M. Dinkel, C. Emmelmann, Laser Additive Manufacturing of Gas Permeable Structures, *Physics Procedia* 41 (2013) 873–880. <https://doi.org/10.1016/j.phpro.2013.03.161>.
- [11] J. van der Stok, O.P. van der Jagt, S. Amin Yavari, M.F.P. de Haas, J.H. Waarsing, H. Jahr, E.M.M. van Lieshout, P. Patka, J.A.N. Verhaar, A.A. Zadpoor, H. Weinans, Selective laser melting-produced porous titanium scaffolds regenerate bone in critical size cortical bone defects, *J. Orthop. Res.* 31 (2013) 792–799. <https://doi.org/10.1002/jor.22293>.
- [12] Stoffregen H, Fischer J, Siedelhofer C, Abele E, Selective laser melting of porous structures, *Solid Freeform Fabrication Proceedings* (2011) 680–695.
- [13] S.L. Sing, J. An, W.Y. Yeong, F.E. Wiria, Laser and electron-beam powder-bed additive manufacturing of metallic implants: A review on processes, materials and designs, *Journal of Orthopaedic Research* 34 (2016) 369–385. <https://doi.org/10.1002/jor.23075>.
- [14] E. Abele, H.A. Stoffregen, M. Kniepkamp, S. Lang, M. Hampe, Selective laser melting for manufacturing of thin-walled porous elements, *Journal of Materials Processing Technology* 215 (2015) 114–122. <https://doi.org/10.1016/j.jmatprotec.2014.07.017>.
- [15] J.A. Cherry, H.M. Davies, S. Mehmood, N.P. Lavery, S.G.R. Brown, J. Sienz, Investigation into the effect of process parameters on microstructural and physical properties of 316L stainless steel parts by selective laser melting, *Int J Adv Manuf Technol* 76 (2015) 869–879. <https://doi.org/10.1007/s00170-014-6297-2>.
- [16] R. Li, J. Liu, Y. Shi, M. Du, Z. Xie, 316L Stainless Steel with Gradient Porosity Fabricated by Selective Laser Melting, *J. of Materi Eng and Perform* 19 (2010) 666–671. <https://doi.org/10.1007/s11665-009-9535-2>.
- [17] B. Verlee, T. Dormal, J. Lecomte-Beckers, Density and porosity control of sintered 316L stainless steel parts produced by additive manufacturing, *Powder Metallurgy* 55 (2012) 260–267. <https://doi.org/10.1179/0032589912Z.00000000082>.
- [18] J. Fischer, M. Kniepkamp, E. Abele, Micro laser melting: analyses of current potentials and restrictions for the additive manufacturing of micro structures, 2014.

- [19] B. Nagarajan, Z. Hu, X. Song, W. Zhai, J. Wei, Development of Micro Selective Laser Melting: The State of the Art and Future Perspectives, *Engineering* 5 (2019) 702–720. <https://doi.org/10.1016/j.eng.2019.07.002>.
- [20] J. Banhart, Manufacture, characterisation and application of cellular metals and metal foams, *Progress in Materials Science* 46 (2001) 559–632. [https://doi.org/10.1016/S0079-6425\(00\)00002-5](https://doi.org/10.1016/S0079-6425(00)00002-5).
- [21] Y. Zhou, Y. Li, J. Yuan, The stability of aluminum foams at accumulation and condensation stages in gas injection foaming process, *Colloids and Surfaces A: Physicochemical and Engineering Aspects* 482 (2015) 468–476. <https://doi.org/10.1016/j.colsurfa.2015.06.043>.
- [22] X.N. Liu, Y.X. Li, X. Chen, Y. Liu, X.L. Fan, Foam stability in gas injection foaming process, *J Mater Sci* 45 (2010) 6481–6493. <https://doi.org/10.1007/s10853-010-4736-5>.
- [23] X. Fang, Z. Fan, A novel approach to produce Al-alloy foams, *J Mater Sci* 42 (2007) 7894–7898. <https://doi.org/10.1007/s10853-007-1729-0>.
- [24] John Banhart, Michael F. Ashby, Norman A. Fleck, *Metal foams and porous metal structures*, 1999.
- [25] F. Baumgärtner, I. Duarte, J. Banhart, Industrialization of Powder Compact Toaming Process, *Advanced Engineering Materials* 2 (2000) 168–174. [https://doi.org/10.1002/\(SICI\)1527-2648\(200004\)2:4<168:AID-ADEM168>3.0.CO;2-O](https://doi.org/10.1002/(SICI)1527-2648(200004)2:4<168:AID-ADEM168>3.0.CO;2-O).
- [26] V. Gergely, B. Clyne, The FORMGRIP Process: Foaming of Reinforced Metals by Gas Release in Precursors, *Advanced Engineering Materials* 2 (2000) 175–178. [https://doi.org/10.1002/\(SICI\)1527-2648\(200004\)2:4<175:AID-ADEM175>3.0.CO;2-W](https://doi.org/10.1002/(SICI)1527-2648(200004)2:4<175:AID-ADEM175>3.0.CO;2-W).
- [27] F von Zeppelin, M Hirscher, H Stanzick, J Banhart, Desorption of hydrogen from blowing agents used for foaming metals, *Composites Science and Technology* 63 (2003) 2293–2300. [https://doi.org/10.1016/S0266-3538\(03\)00262-8](https://doi.org/10.1016/S0266-3538(03)00262-8).
- [28] J. Barode, U. Aravind, S. Bhogi, B. Muduli, M. Mukherjee, Mg and Mg-Based Blowing Agents for Aluminum Foam, *Metall Mater Trans B* 52 (2021) 292–304. <https://doi.org/10.1007/s11663-020-02008-2>.
- [29] L. Drenchev, J. Sobczak, S. Malinov, W. Sha, Gasars: a class of metallic materials with ordered porosity, *Materials Science and Technology* 22 (2006) 1135–1147. <https://doi.org/10.1179/174328406X118302>.

- [30] V.I. Shapovalov, Porous and cellular materials for structural applications, 1998.
- [31] Vladimir I. Shapovalov, Method for manufacturing porous articles, 1993.
- [32] P Neumann, Metal foams and porous metal structures, 1999.
- [33] Y. Torres, S. Lascano, J. Bris, J. Pavón, J.A. Rodriguez, Development of porous titanium for biomedical applications: A comparison between loose sintering and space-holder techniques, *Mater. Sci. Eng. C Mater. Biol. Appl.* 37 (2014) 148–155. <https://doi.org/10.1016/j.msec.2013.11.036>.
- [34] Z. Esen, E. T. Bor, A. Ş. BOR, Characterization of loose powder sintered porous titanium and Ti6Al4V alloy, *Turkish J Eng Env Sci* 33 (2010) 207–219.
- [35] N. Nomura, T. Kohama, I.H. Oh, S. Hanada, A. Chiba, M. Kanehira, K. Sasaki, Mechanical properties of porous Ti–15Mo–5Zr–3Al compacts prepared by powder sintering, *Materials Science and Engineering: C* 25 (2005) 330–335. <https://doi.org/10.1016/j.msec.2005.04.001>.
- [36] M.A. Atwater, L.N. Guevara, K.A. Darling, M.A. Tschopp, Solid State Porous Metal Production: A Review of the Capabilities, Characteristics, and Challenges, *Adv. Eng. Mater.* 20 (2018) 1700766. <https://doi.org/10.1002/adem.201700766>.
- [37] P.J. Kwok, S.M. Oppenheimer, D.C. Dunand, Porous Titanium by Electro-chemical Dissolution of Steel Space-holders, *Advanced Engineering Materials* 10 (2008) 820–825. <https://doi.org/10.1002/adem.200800072>.
- [38] Y. Hangai, K. Zushida, H. Fujii, R. Ueji, O. Kuwazuru, N. Yoshikawa, Friction powder compaction process for fabricating open-celled Cu foam by sintering-dissolution process route using NaCl space holder, *Materials Science and Engineering: A* 585 (2013) 468–474. <https://doi.org/10.1016/j.msea.2013.08.004>.
- [39] C. Wen, M. Mabuchi, Y. Yamada, K. Shimojima, Y. Chino, T. Asahina, Processing of biocompatible porous Ti and Mg, *Scripta Materialia* 45 (2001) 1147–1153. [https://doi.org/10.1016/S1359-6462\(01\)01132-0](https://doi.org/10.1016/S1359-6462(01)01132-0).
- [40] C.E. Wen, Y. Yamada, K. Shimojima, Y. Chino, H. Hosokawa, M. Mabuchi, Novel titanium foam for bone tissue engineering, *Journal of Materials Research* 17 (2002) 2633–2639. <https://doi.org/10.1557/JMR.2002.0382>.
- [41] D. Kupp, D. Claar and K. Flemmig, Processing of controlled porosity titanium-based materials, 2002.
- [42] Vladimir Paserin, Jun Shu and Sam Marcuson, Superior Nickel Foam Production: Starting from Raw Materials Quality Control, 2005.
- [43] A. Bansiddhi, T.D. Sargeant, S.I. Stupp, D.C. Dunand, Porous NiTi for bone implants: a review, *Acta Biomater.* 4 (2008) 773–782.

- <https://doi.org/10.1016/j.actbio.2008.02.009>.
- [44] Y. Zhou, Y. Zhu, Three-dimensional Ta foams produced by replication of NaCl space-holders, *Materials Letters* 99 (2013) 8–10.  
<https://doi.org/10.1016/j.matlet.2013.02.068>.
- [45] A. Bansiddhi, D.C. Dunand, Shape-memory NiTi foams produced by solid-state replication with NaF, *Intermetallics* 15 (2007) 1612–1622.  
<https://doi.org/10.1016/j.intermet.2007.06.013>.
- [46] D.P. Mondal, H. Jain, S. Das, A.K. Jha, Stainless steel foams made through powder metallurgy route using NH<sub>4</sub>HCO<sub>3</sub> as space holder, *Materials & Design* 88 (2015) 430–437. <https://doi.org/10.1016/j.matdes.2015.09.020>.
- [47] W.E. Frazier, Metal Additive Manufacturing: A Review, *J. of Materi Eng and Perform* 23 (2014) 1917–1928. <https://doi.org/10.1007/s11665-014-0958-z>.
- [48] H. Bikas, P. Stavropoulos, G. Chryssolouris, Additive manufacturing methods and modelling approaches: a critical review, *Int J Adv Manuf Technol* 83 (2016) 389–405. <https://doi.org/10.1007/s00170-015-7576-2>.
- [49] J. Banhart, Metal Foams: Production and Stability, *Advanced Engineering Materials* 8 (2006) 781–794. <https://doi.org/10.1002/adem.200600071>.
- [50] J. Banhart, Light-Metal Foams-History of Innovation and Technological Challenges, *Adv. Eng. Mater.* 15 (2013) 82–111.  
<https://doi.org/10.1002/adem.201200217>.
- [51] J. Banhart, H.-W. Seeliger, Recent Trends in Aluminum Foam Sandwich Technology, *Adv. Eng. Mater.* 14 (2012) 1082–1087.  
<https://doi.org/10.1002/adem.201100333>.
- [52] J. Baumeister, J. Banhart, M. Weber, Aluminium foams for transport industry, *Materials & Design* 18 (1997) 217–220. [https://doi.org/10.1016/s0261-3069\(97\)00050-2](https://doi.org/10.1016/s0261-3069(97)00050-2).
- [53] L.-Y. Chen, J.-S. Yu, T. Fujita, M.-W. Chen, Nanoporous Copper with Tunable Nanoporosity for SERS Applications, *Adv. Funct. Mater.* 19 (2009) 1221–1226. <https://doi.org/10.1002/adfm.200801239>.
- [54] H.-B. Lu, Y. Li, F.-H. Wang, Synthesis of porous copper from nanocrystalline two-phase Cu–Zr film by dealloying, *Scripta Materialia* 56 (2007) 165–168.  
<https://doi.org/10.1016/j.scriptamat.2006.09.009>.
- [55] H.-C. Shin, M. Liu, Copper Foam Structures with Highly Porous Nanostructured Walls, *Chem. Mater.* 16 (2004) 5460–5464.  
<https://doi.org/10.1021/cm048887b>.

- [56] S. Xie, J.R.G. Evans, High porosity copper foam, *Journal of Materials Science* 39 (2004) 5877–5880. <https://doi.org/10.1023/b:jmsc.0000040107.04387.b7>.
- [57] J. Biener, A. Wittstock, L.A. Zepeda-Ruiz, M.M. Biener, V. Zielasek, D. Kramer, R.N. Viswanath, J. Weissmüller, M. Bäumer, A.V. Hamza, Surface-chemistry-driven actuation in nanoporous gold, *Nature Mater* 8 (2009) 47–51. <https://doi.org/10.1038/nmat2335>.
- [58] S. Cherevko, C.-H. Chung, Direct electrodeposition of nanoporous gold with controlled multimodal pore size distribution, *Electrochemistry Communications* 13 (2011) 16–19. <https://doi.org/10.1016/j.elecom.2010.11.001>.
- [59] F. Jia, C. Yu, Z. Ai, L. Zhang, Fabrication of Nanoporous Gold Film Electrodes with Ultrahigh Surface Area and Electrochemical Activity, *Chem. Mater.* 19 (2007) 3648–3653. <https://doi.org/10.1021/cm070425l>.
- [60] E. Seker, M. Reed, M. Begley, Nanoporous Gold: Fabrication, Characterization, and Applications, *Materials (Basel)* 2 (2009) 2188–2215. <https://doi.org/10.3390/ma2042188>.
- [61] N. Bekoz, E. Oktay, High temperature mechanical properties of low alloy steel foams produced by powder metallurgy, *Materials & Design* 53 (2014) 482–489. <https://doi.org/10.1016/j.matdes.2013.07.050>.
- [62] T. Murakami, K. Ohara, T. Narushima, C. Ouchi, Development of a New Method for Manufacturing Iron Foam Using Gases Generated by Reduction of Iron Oxide, *Mater. Trans.* 48 (2007) 2937–2944. <https://doi.org/10.2320/matertrans.MRA2007127>.
- [63] A.A. Plunk, D.C. Dunand, Iron foams created by directional freeze casting of iron oxide, reduction and sintering, *Materials Letters* 191 (2017) 112–115. <https://doi.org/10.1016/j.matlet.2016.12.104>.
- [64] B.H. Smith, S. Szyniszewski, J.F. Hajjar, B.W. Schafer, S.R. Arwade, Steel foam for structures: A review of applications, manufacturing and material properties, *Journal of Constructional Steel Research* 71 (2012) 1–10. <https://doi.org/10.1016/j.jcsr.2011.10.028>.
- [65] J. Weise, J. Baumeister, O. Yezerska, N. Salk, G.B.D. Silva, Syntactic Iron Foams with Integrated Microglass Bubbles Produced by Means of Metal Powder Injection Moulding, *Adv. Eng. Mater.* 12 (2010) 604–608. <https://doi.org/10.1002/adem.200900297>.
- [66] S.F. Aida, H. Zuhailawati, A.S. Anasyida, The Effect of Space Holder Content and Sintering Temperature of Magnesium Foam on Microstructural and

- Properties Prepared by Sintering Dissolution Process (SDP) Using Carbamide Space Holder, *Procedia Engineering* 184 (2017) 290–297.  
<https://doi.org/10.1016/j.proeng.2017.04.097>.
- [67] G.L. Hao, F.S. Han, W.D. Li, Processing and mechanical properties of magnesium foams, *J Porous Mater* 16 (2009) 251–256.  
<https://doi.org/10.1007/s10934-008-9194-y>.
- [68] Hartmann M, Reindel K, Singer R F, Microstructure and mechanical properties of cellular magnesium matrix composites, 1999.
- [69] A. Kucharczyk, K. Naplocha, J.W. Kaczmar, H. Dieringa, K.U. Kainer, Current Status and Recent Developments in Porous Magnesium Fabrication, *Adv. Eng. Mater.* 20 (2018) 1700562. <https://doi.org/10.1002/adem.201700562>.
- [70] J. Liu, S. Shi, Z. Zheng, K. Huang, Y. Yan, Characterization and compressive properties of Ni/Mg hybrid foams, *Materials Science and Engineering: A* 708 (2017) 329–335. <https://doi.org/10.1016/j.msea.2017.09.130>.
- [71] K. Renger, H. Kaufmann, Vacuum Foaming of Magnesium Slurries, *Advanced Engineering Materials* 7 (2005) 117–123.  
<https://doi.org/10.1002/adem.200400191>.
- [72] Babjak, Juraj, Victor A. Ettl, and Vladimir Paserin, Method of forming nickel foam U.S. Patent No. 4,957,543, 1990.
- [73] H. Choe, Synthesis, structure, and mechanical properties of Ni–Al and Ni–Cr–Al superalloy foams, *Acta Materialia* 52 (2004) 1283–1295.  
<https://doi.org/10.1016/j.actamat.2003.11.012>.
- [74] P.S. Liu, K.M. Liang, Preparation and corresponding structure of nickel foam, *Materials Science and Technology* 16 (2000) 575–578.  
<https://doi.org/10.1179/026708300101508108>.
- [75] V. Paserin, S. Marcuson, J. Shu, D.S. Wilkinson, CVD Technique for Inco Nickel Foam Production, *Advanced Engineering Materials* 6 (2004) 454–459.  
<https://doi.org/10.1002/adem.200405142>.
- [76] S.S. Sundarram, W. Jiang, W. Li, 2014. Fabrication of Small Pore-Size Nickel Foams Using Electroless Plating of Solid-State Foamed Immiscible Polymer Blends. *J. Manuf. Sci. Eng* 136, 021002. <https://doi.org/10.1115/1.4025418>.
- [77] Y. Chino, D.C. Dunand, Directionally freeze-cast titanium foam with aligned, elongated pores, *Acta Materialia* 56 (2008) 105–113.  
<https://doi.org/10.1016/j.actamat.2007.09.002>.
- [78] N.G. Davis, J. Teisen, C. Schuh, D.C. Dunand, Solid-state foaming of titanium

- by superplastic expansion of argon-filled pores, *Journal of Materials Research* 16 (2001) 1508–1519. <https://doi.org/10.1557/JMR.2001.0210>.
- [79] D.C. Dunand, Processing of Titanium Foams, *Advanced Engineering Materials* 6 (2004) 369–376. <https://doi.org/10.1002/adem.200405576>.
- [80] D.C. Dunand, J. Teisen, Superplastic Foaming of Titanium and Ti-6Al-4V, *MRS Online Proceeding Library Archive* 521 (1998). <https://doi.org/10.1557/proc-521-231>.
- [81] Z. Esen, Ş. Bor, Processing of titanium foams using magnesium spacer particles, *Scripta Materialia* 56 (2007) 341–344. <https://doi.org/10.1016/j.scriptamat.2006.11.010>.
- [82] X. Jian, C. Hao, Q. Guibao, Y. Yang, L. Xuwei, Investigation on relationship between porosity and spacer content of titanium foams, *Materials & Design* 88 (2015) 132–137. <https://doi.org/10.1016/j.matdes.2015.08.125>.
- [83] R. Singh, P.D. Lee, J.R. Jones, G. Poologasundarampillai, T. Post, T.C. Lindley, R.J. Dashwood, Hierarchically structured titanium foams for tissue scaffold applications, *Acta Biomater.* 6 (2010) 4596–4604. <https://doi.org/10.1016/j.actbio.2010.06.027>.
- [84] M. Chamoun, B.J. Hertzberg, T. Gupta, D. Davies, S. Bhadra, B. van Tassell, C. Erdonmez, D.A. Steingart, Hyper-dendritic nanoporous zinc foam anodes, *NPG Asia Mater* 7 (2015) e178-e178. <https://doi.org/10.1038/am.2015.32>.
- [85] S. Hossein Elahi, R. Arabi Jeshvaghani, H.R. Shahverdi, Influence of calcium addition and stirring on the cellular structure and foaming behavior of molten zinc, *Appl. Phys. A* 119 (2015) 533–538. <https://doi.org/10.1007/s00339-015-8985-7>.
- [86] P.-C. Hsu, S.-K. Seol, T.-N. Lo, C.-J. Liu, C.-L. Wang, C.-S. Lin, Y. Hwu, C.H. Chen, L.-W. Chang, J.H. Je, G. Margaritondo, Hydrogen Bubbles and the Growth Morphology of Ramified Zinc by Electrodeposition, *J. Electrochem. Soc.* 155 (2008) D400. <https://doi.org/10.1149/1.2894189>.
- [87] D.P. Mondal, M.D. Goel, N. Bagde, N. Jha, S. Sahu, A.K. Barnwal, Closed cell ZA27–SiC foam made through stir-casting technique, *Materials & Design* 57 (2014) 315–324. <https://doi.org/10.1016/j.matdes.2013.12.026>.
- [88] J. Banhart, J. Baumeister, O. Irretier, J. Jöbstl, Fabricating-Cost-effective production techniques for the manufacture of aluminium foams, 2000.
- [89] S. Arabnejad, B. Johnston, M. Tanzer, D. Pasini, Fully porous 3D printed titanium femoral stem to reduce stress-shielding following total hip arthroplasty,

- J. Orthop. Res. 35 (2017) 1774–1783. <https://doi.org/10.1002/jor.23445>.
- [90] B. Dittmar, A. Behrens, N. Schödel, M. Rüttinger, T. Franco, G. Straczewski, R. Dittmeyer, Methane steam reforming operation and thermal stability of new porous metal supported tubular palladium composite membranes, *International Journal of Hydrogen Energy* 38 (2013) 8759–8771. <https://doi.org/10.1016/j.ijhydene.2013.05.030>.
- [91] K.M. Au, K.M. Yu, A scaffolding architecture for conformal cooling design in rapid plastic injection moulding, *Int J Adv Manuf Technol* 34 (2007) 496–515. <https://doi.org/10.1007/s00170-006-0628-x>.
- [92] J.C. Ferreira, A. Mateus, Studies of rapid soft tooling with conformal cooling channels for plastic injection moulding, *Journal of Materials Processing Technology* 142 (2003) 508–516. [https://doi.org/10.1016/S0924-0136\(03\)00650-2](https://doi.org/10.1016/S0924-0136(03)00650-2).
- [93] D. Chantzis, X. Liu, D.J. Politis, O. El Fakir, T.Y. Chua, Z. Shi, L. Wang, Review on additive manufacturing of tooling for hot stamping, *Int J Adv Manuf Technol* 109 (2020) 87–107. <https://doi.org/10.1007/s00170-020-05622-1>.
- [94] Antonio Armillotta, Raffaello Baraggi & Simone Fasoli, SLM tooling for die casting with conformal cooling channels, 2014.
- [95] T.Y. Chan, D.X. Wang, H.J. Chang, C.L. Chen, Fabrication of Gas-Permeable Die Materials Having Orthogonally Arrayed Pore Channels, *Progress in Powder Metallurgy* 534-536 (2007) 961–964. <https://doi.org/10.4028/www.scientific.net/MSF.534-536.961>.
- [96] G.H. Zeng, T. Song, Y.H. Dai, H.P. Tang, M. Yan, 3D printed breathable mould steel: Small micrometer-sized, interconnected pores by creatively introducing foaming agent to additive manufacturing, *Materials & Design* 169 (2019) 107693. <https://doi.org/10.1016/j.matdes.2019.107693>.
- [97] A. Evans, Multifunctionality of cellular metal systems, *Progress in Materials Science* 43 (1998) 171–221. [https://doi.org/10.1016/S0079-6425\(98\)00004-8](https://doi.org/10.1016/S0079-6425(98)00004-8).
- [98] S. Bellekom, R. Benders, S. Pelgröm, H. Moll, Electric cars and wind energy: Two problems, one solution? A study to combine wind energy and electric cars in 2020 in The Netherlands, *Energy* 45 (2012) 859–866. <https://doi.org/10.1016/j.energy.2012.07.003>.
- [99] F. García-Moreno, Commercial Applications of Metal Foams: Their Properties and Production, *Materials (Basel)* 9 (2016). <https://doi.org/10.3390/ma9020085>.
- [100] Graichen A, Larfeldt J, Lörst ad D, Munktell E, Porous rotating machine

- component, combustor and manufacturing method: U.S. Patent 10,753,609[P]. 2020-8-25.
- [101] D.-G. Ahn, Direct metal additive manufacturing processes and their sustainable applications for green technology: A review, *Int. J. of Precis. Eng. and Manuf.-Green Tech.* 3 (2016) 381–395. <https://doi.org/10.1007/s40684-016-0048-9>.
- [102] D. Ding, Z. Pan, D. Cuiuri, H. Li, Wire-feed additive manufacturing of metal components: technologies, developments and future interests, *Int J Adv Manuf Technol* 81 (2015) 465–481. <https://doi.org/10.1007/s00170-015-7077-3>.
- [103] A. Simchi, F. Petzoldt, H. Pohl, On the development of direct metal laser sintering for rapid tooling, *Journal of Materials Processing Technology* 141 (2003) 319–328. [https://doi.org/10.1016/s0924-0136\(03\)00283-8](https://doi.org/10.1016/s0924-0136(03)00283-8).
- [104] P. Heinl, L. Müller, C. Körner, R.F. Singer, F.A. Müller, Cellular Ti-6Al-4V structures with interconnected macro porosity for bone implants fabricated by selective electron beam melting, *Acta Biomater.* 4 (2008) 1536–1544. <https://doi.org/10.1016/j.actbio.2008.03.013>.
- [105] M. Agarwala, D. Bourell, J. Beaman, H. Marcus, J. Barlow, Direct selective laser sintering of metals, *Rapid Prototyping Journal* 1 (1995) 26–36. <https://doi.org/10.1108/13552549510078113>.
- [106] J.P. Kruth, L. Froyen, J. van Vaerenbergh, P. Mercelis, M. Rombouts, B. Lauwers, Selective laser melting of iron-based powder, *Journal of Materials Processing Technology* 149 (2004) 616–622. <https://doi.org/10.1016/j.jmatprotec.2003.11.051>.
- [107] Taminger, Karen, and Robert A. Hafley, *Electron beam freeform fabrication: a rapid metal deposition process*, 2003.
- [108] C. Atwood, M. Griffith, L. Harwell, E. Schlienger, M. Ensz, J. Smugeresky, T. Romero, D. Greene, D. Reckaway, Laser engineered net shaping (LENS™): A tool for direct fabrication of metal parts, *International Congress on Applications of Lasers & Electro-Optics 1998* (2018) E1-E7. <https://doi.org/10.2351/1.5059147>.
- [109] T. Furumoto, T. Ueda, N. Kobayashi, A. Yassin, A. Hosokawa, S. Abe, Study on laser consolidation of metal powder with Yb: fiber laser—Evaluation of line consolidation structure, *Journal of Materials Processing Technology* 209 (2009) 5973–5980. <https://doi.org/10.1016/j.jmatprotec.2009.07.017>.
- [110] J. Milewski, G. Lewis, D. Thoma, G. Keel, R. Nemeč, R. Reinert, Directed light fabrication of a solid metal hemisphere using 5-axis powder deposition,

- Journal of Materials Processing Technology 75 (1998) 165–172.  
[https://doi.org/10.1016/s0924-0136\(97\)00321-x](https://doi.org/10.1016/s0924-0136(97)00321-x).
- [111] F. Wang, S. Williams, P. Colegrove, A.A. Antonysamy, Microstructure and Mechanical Properties of Wire and Arc Additive Manufactured Ti-6Al-4V, Metall and Mat Trans A 44 (2013) 968–977. <https://doi.org/10.1007/s11661-012-1444-6>.
- [112] B. Utela, D. Storti, R. Anderson, M. Ganter, A review of process development steps for new material systems in three dimensional printing (3DP), Journal of Manufacturing Processes 10 (2008) 96–104.  
<https://doi.org/10.1016/j.jmapro.2009.03.002>.
- [113] B. Mueller, D. Kochan, Laminated object manufacturing for rapid tooling and patternmaking in foundry industry, Computers in Industry 39 (1999) 47–53.  
[https://doi.org/10.1016/s0166-3615\(98\)00127-4](https://doi.org/10.1016/s0166-3615(98)00127-4).
- [114] C.Y. Kong, R.C. Soar, Fabrication of metal–matrix composites and adaptive composites using ultrasonic consolidation process, Materials Science and Engineering: A 412 (2005) 12–18. <https://doi.org/10.1016/j.msea.2005.08.041>.
- [115] S. Yi, F. Liu, J. Zhang, S. Xiong, Study of the key technologies of LOM for functional metal parts, Journal of Materials Processing Technology 150 (2004) 175–181. <https://doi.org/10.1016/j.jmatprotec.2004.01.035>.
- [116] D.-G. Ahn, Direct metal additive manufacturing processes and their sustainable applications for green technology: A review, Int. J. of Precis. Eng. and Manuf.-Green Tech. 3 (2016) 381–395. <https://doi.org/10.1007/s40684-016-0048-9>.
- [117] T. Obikawa, Rapid Manufacturing System by Sheet Steel Lamination, Proc.14<sup>th</sup> International Conference on Computer aided Production Engineering (1998) 265–270.
- [118] T. Obikawa, Development of rapid manufacturing system with thick steel sheet as modeling materials [J], 1998.
- [119] Applying laminated die to manufacture automobile part in large size, 2000.
- [120] Connect technique of laminated object manufacturing using metallic materials as modeling materials, 2002.
- [121] Study on the key technology of laminated object manufacturing for metal parts, 2002.
- [122] T. Gietzelt, V. Toth, A. Huell, Challenges of Diffusion Bonding of Different Classes of Stainless Steels, Adv. Eng. Mater. 20 (2018) 1700367.  
<https://doi.org/10.1002/adem.201700367>.

- [123] T. Gietzelt, M. Walter, V. Toth, F. Messerschmidt, M. Blem, Comprehensive Study of the Influence of the Bonding Temperature and Contact Pressure Regimes during Diffusion Bonding on the Deformation and Mechanical Properties of AISI 304, *Advanced Engineering Materials* 23 (2021) 2100188. <https://doi.org/10.1002/adem.202100188>.
- [124] M. Belimov, D. Metzger, P. Pfeifer, On the temperature control in a microstructured packed bed reactor for methanation of CO/CO<sub>2</sub> mixtures, *AIChE J.* 63 (2017) 120–129. <https://doi.org/10.1002/aic.15461>.
- [125] R. Dittmeyer, T. Boeltken, P. Piermartini, M. Selinsek, M. Loewert, F. Dallmann, H. Kreuder, M. Cholewa, A. Wunsch, M. Belimov, S. Farsi, P. Pfeifer, Micro and micro membrane reactors for advanced applications in chemical energy conversion, *Current Opinion in Chemical Engineering* 17 (2017) 108–125. <https://doi.org/10.1016/j.coche.2017.08.001>.
- [126] E. Sachs, M. Cima, J. Cornie, Three-Dimensional Printing: Rapid Tooling and Prototypes Directly from a CAD Model, *CIRP Annals* 39 (1990) 201–204. [https://doi.org/10.1016/S0007-8506\(07\)61035-X](https://doi.org/10.1016/S0007-8506(07)61035-X).
- [127] M. Ziaee, N.B. Crane, Binder jetting: A review of process, materials, and methods, *Additive Manufacturing* 28 (2019) 781–801. <https://doi.org/10.1016/j.addma.2019.05.031>.
- [128] T. Dahmen, C.G. Klingaa, S. Baier-Stegmaier, A. Lapina, D.B. Pedersen, J.H. Hattel, Characterization of channels made by laser powder bed fusion and binder jetting using X-ray CT and image analysis, *Additive Manufacturing* 36 (2020) 101445. <https://doi.org/10.1016/j.addma.2020.101445>.
- [129] A. Lores, N. Azurmendi, I. Agote, E. Zuza, A review on recent developments in binder jetting metal additive manufacturing: materials and process characteristics, *Powder Metallurgy* 62 (2019) 267–296. <https://doi.org/10.1080/00325899.2019.1669299>.
- [130] An experimental study of ceramic dental porcelain materials using a 3D print (3DP) process, 2014.
- [131] Impact of laser power and build orientation on the mechanical properties of selectively laser sintered parts, 2013.
- [132] J.P. Kruth, Material Incess Manufacturing by Rapid Prototyping Techniques, *CIRP Annals* 40 (1991) 603–614. [https://doi.org/10.1016/S0007-8506\(07\)61136-6](https://doi.org/10.1016/S0007-8506(07)61136-6).
- [133] H. Bikas, P. Stavropoulos, G. Chryssolouris, Additive manufacturing methods

- and modelling approaches: a critical review, *Int J Adv Manuf Technol* 83 (2016) 389–405. <https://doi.org/10.1007/s00170-015-7576-2>.
- [134] H. Bikas, P. Stavropoulos, G. Chryssolouris, Additive manufacturing methods and modelling approaches: a critical review, *Int J Adv Manuf Technol* 83 (2016) 389–405. <https://doi.org/10.1007/s00170-015-7576-2>.
- [135] R. Berger, *Additive manufacturing: A game changer for the manufacturing industry*, 2013.
- [136] T.G. Spears, S.A. Gold, In-process sensing in selective laser melting (SLM) additive manufacturing, *Integr Mater Manuf Innov* 5 (2016) 16–40. <https://doi.org/10.1186/s40192-016-0045-4>.
- [137] J.-P. Kruth, G. Levy, F. Klocke, T. Childs, Consolidation phenomena in laser and powder-bed based layered manufacturing, *CIRP Annals* 56 (2007) 730–759. <https://doi.org/10.1016/j.cirp.2007.10.004>.
- [138] S.F.S. Shirazi, S. Gharehkhani, M. Mehrali, H. Yarmand, H.S.C. Metselaar, N. Adib Kadri, N.A.A. Osman, A review on powder-based additive manufacturing for tissue engineering: selective laser sintering and inkjet 3D printing, *Sci. Technol. Adv. Mater.* 16 (2015) 33502. <https://doi.org/10.1088/1468-6996/16/3/033502>.
- [139] A.S.K. Kiran, J.B. Veluru, S. Merum, A.V. Radhamani, M. Doble, T.S.S. Kumar, S. Ramakrishna, Additive manufacturing technologies: an overview of challenges and perspective of using electrospraying, *Nanocomposites* 4 (2018) 190–214. <https://doi.org/10.1080/20550324.2018.1558499>.
- [140] A. Gasser, G. Backes, I. Kelbassa, A. Weisheit, K. Wissenbach, *Laser Additive Manufacturing*, *L TJ* 7 (2010) 58–63. <https://doi.org/10.1002/latj.201090029>.
- [141] V.K. Balla, P.D. DeVasConCellos, W. Xue, S. Bose, A. Bandyopadhyay, Fabrication of compositionally and structurally graded Ti-TiO<sub>2</sub> structures using laser engineered net shaping (LENS), *Acta Biomater.* 5 (2009) 1831–1837. <https://doi.org/10.1016/j.actbio.2009.01.011>.
- [142] G.K. Lewis, E. Schlienger, Practical considerations and capabilities for laser assisted direct metal deposition, *Materials & Design* 21 (2000) 417–423. [https://doi.org/10.1016/s0261-3069\(99\)00078-3](https://doi.org/10.1016/s0261-3069(99)00078-3).
- [143] K. Zhang, W. Liu, X. Shang, Research on the processing experiments of laser metal deposition shaping, *Optics & Laser Technology* 39 (2007) 549–557. <https://doi.org/10.1016/j.optlastec.2005.10.009>.
- [144] G. Lewis, *Direct Laser Metal Deposition Process Fabricates Near-Net-Shape*

- Components Rapidly, *Materials Technology* 10 (1995) 51–54.  
<https://doi.org/10.1080/10667857.1995.11752590>.
- [145] W. Hofmeister, M. Griffith, Solidification in direct metal deposition by LENS processing, *JOM* 53 (2001) 30–34. <https://doi.org/10.1007/s11837-001-0066-z>.
- [146] N. Guo, M.C. Leu, Additive manufacturing: technology, applications and research needs, *Front. Mech. Eng.* 8 (2013) 215–243.  
<https://doi.org/10.1007/s11465-013-0248-8>.
- [147] D.-G. Ahn, Hardfacing technologies for improvement of wear characteristics of hot working tools: A Review, *Int. J. Precis. Eng. Manuf.* 14 (2013) 1271–1283.  
<https://doi.org/10.1007/s12541-013-0174-z>.
- [148] A review of hybrid manufacturing, 2015.
- [149] A. Gasser, G. Backes, I. Kelbassa, A. Weisheit, K. Wissenbach, Laser Additive Manufacturing, *Laser Technik Journal* 7 (2010) 58–63.  
<https://doi.org/10.1002/latj.201090029>.
- [150] D. Ding, Z. Pan, D. Cuiuri, H. Li, Wire-feed additive manufacturing of metal components: technologies, developments and future interests, *Int J Adv Manuf Technol* 81 (2015) 465–481. <https://doi.org/10.1007/s00170-015-7077-3>.
- [151] W.E. Frazier, Metal Additive Manufacturing: A Review, *J. of Materi Eng and Perform* 23 (2014) 1917–1928. <https://doi.org/10.1007/s11665-014-0958-z>.
- [152] D. Ding, Z. Pan, D. Cuiuri, H. Li, Wire-feed additive manufacturing of metal components: technologies, developments and future interests, *Int J Adv Manuf Technol* 81 (2015) 465–481. <https://doi.org/10.1007/s00170-015-7077-3>.
- [153] B. Graf, S. Ammer, A. Gumenyuk, M. Rethmeier, Design of Experiments for Laser Metal Deposition in Maintenance, Repair and Overhaul Applications, *Procedia CIRP* 11 (2013) 245–248. <https://doi.org/10.1016/j.procir.2013.07.031>.
- [154] K. Mumtaz, N. Hopkinson, Top surface and side roughness of Inconel 625 parts processed using selective laser melting, *Rapid Prototyping Journal* 15 (2009) 96–103. <https://doi.org/10.1108/13552540910943397>.
- [155] K.A. Mumtaz, N. Hopkinson, Selective Laser Melting of thin wall parts using pulse shaping, *Journal of Materials Processing Technology* 210 (2010) 279–287.  
<https://doi.org/10.1016/j.jmatprotec.2009.09.011>.
- [156] H.H. Zhu, L. Lu, J. Fuh, Development and characterisation of direct laser sintering Cu-based metal powder, *Journal of Materials Processing Technology* 140 (2003) 314–317. [https://doi.org/10.1016/s0924-0136\(03\)00755-6](https://doi.org/10.1016/s0924-0136(03)00755-6).
- [157] J. Milewski, G. Lewis, D. Thoma, G. Keel, R. Nemeč, R. Reinert, Directed

- light fabrication of a solid metal hemisphere using 5-axis powder deposition, *Journal of Materials Processing Technology* 75 (1998) 165–172.  
[https://doi.org/10.1016/s0924-0136\(97\)00321-x](https://doi.org/10.1016/s0924-0136(97)00321-x).
- [158] R. KM.Taminger, *Electron beam freeform fabrication for cost effective near-net shape manufacturing*, 2006.
- [159] H. Löwe, W. Ehrfeld, State-of-the-art in microreaction technology: concepts, manufacturing and applications, *Electrochimica Acta* 44 (1999) 3679–3689.  
[https://doi.org/10.1016/S0013-4686\(99\)00071-7](https://doi.org/10.1016/S0013-4686(99)00071-7).
- [160] V. Hessel, *Micro process engineering: A comprehensive handbook / edited by Volker Hessel ... [et al.]*, Wiley-VCH; [Chichester John Wiley, Weinheim, 2009.
- [161] T. Zheng, W. Zhou, W. Yu, Y. Ke, Y. Liu, R. Liu, K. San Hui, Methanol steam reforming performance optimisation of cylindrical microreactor for hydrogen production utilising error backpropagation and genetic algorithm, *Chemical Engineering Journal* 357 (2019) 641–654.  
<https://doi.org/10.1016/j.cej.2018.09.129>.
- [162] A. Pohar, I. Plazl, Process Intensification through Microreactor Application, *Chemical and Biochemical Engineering Quarterly* 23 (2009) 537–544.
- [163] A. Madhawan, A. Arora, J. Das, A. Kuila, V. Sharma, Microreactor technology for biodiesel production: a review, *Biomass Conv. Bioref.* 8 (2018) 485–496.  
<https://doi.org/10.1007/s13399-017-0296-0>.
- [164] B.P. Mason, K.E. Price, J.L. Steinbacher, A.R. Bogdan, D.T. McQuade, Greener approaches to organic synthesis using microreactor technology, *Chem. Rev.* 107 (2007) 2300–2318. <https://doi.org/10.1021/cr050944c>.
- [165] N. Akkarawatkhoosith, A. Srichai, A. Kaewchada, C. Ngamcharussrivichai, A. Jaree, Evaluation on safety and energy requirement of biodiesel production: Conventional system and microreactors, *Process Safety and Environmental Protection* 132 (2019) 294–302. <https://doi.org/10.1016/j.psep.2019.10.018>.
- [166] K. Raoufi, S. Manoharan, T. Etheridge, B.K. Paul, K.R. Haapala, Cost and Environmental Impact Assessment of Stainless Steel Microreactor Plates using Binder Jetting and Metal Injection Molding Processes, *Procedia Manufacturing* 48 (2020) 311–319. <https://doi.org/10.1016/j.promfg.2020.05.052>.
- [167] P.L. Mills, D.J. Quiram, J.F. Ryley, Microreactor technology and process miniaturization for catalytic reactions—A perspective on recent developments and emerging technologies, *Chemical Engineering Science* 62 (2007) 6992–7010.  
<https://doi.org/10.1016/j.ces.2007.09.021>.

- [168] Y. Qin, Overview of micro-manufacturing, 2010.
- [169] Yi Qin, Advances in micro-manufacturing research and technological development, and challenges/opportunities for micro-mechanical-machining: keynote paper, Cutting Tool Congress 2007 (2007).
- [170] A.R. Razali, Y. Qin, A Review on Micro-manufacturing, Micro-forming and their Key Issues, *Procedia Engineering* 53 (2013) 665–672. <https://doi.org/10.1016/j.proeng.2013.02.086>.
- [171] R.B. Aronson, *The new world of micromanufacturing*, 2003.
- [172] R.B. Aronson, *Micromanufacturing Is Growing*, 2004.
- [173] Y. Kibe, Y. Okada, K. Mitsui, Machining accuracy for shearing process of thin-sheet metals—Development of initial tool position adjustment system, *International Journal of Machine Tools and Manufacture* 47 (2007) 1728–1737. <https://doi.org/10.1016/j.ijmactools.2006.12.006>.
- [174] Mohammad Vaezi, Hermann Seitz, Shoufeng Yang, *A review on 3D micro-additive manufacturing technologies*, 2013.
- [175] Felip Esteve, Djamila Olivier, Qin Hu, Martin Baumers, *Micro-additive Manufacturing Technology*, in: *Micro-Manufacturing Technologies and Their Applications*, Springer, Cham, 2017, pp. 67–95.
- [176] Ganesa Balamurugan Kannan, Dinesh Kumar Rajendran, *A Review on Status of Research in Metal Additive Manufacturing*, in: *Advances in 3D Printing & Additive Manufacturing Technologies*, Springer, Singapore, 2017, pp. 95–100.
- [177] L.F. Arenas, C. Ponce de León, F.C. Walsh, 3D-printed porous electrodes for advanced electrochemical flow reactors: A Ni/stainless steel electrode and its mass transport characteristics, *Electrochemistry Communications* 77 (2017) 133–137. <https://doi.org/10.1016/j.elecom.2017.03.009>.
- [178] S. Guddati, A.S.K. Kiran, M. Leavy, S. Ramakrishna, Recent advancements in additive manufacturing technologies for porous material applications, *Int J Adv Manuf Technol* 105 (2019) 193–215. <https://doi.org/10.1007/s00170-019-04116-z>.
- [179] Q. Wei, H. Li, G. Liu, Y. He, Y. Wang, Y.E. Tan, D. Wang, X. Peng, G. Yang, N. Tsubaki, Metal 3D printing technology for functional integration of catalytic system, *Nat. Commun.* 11 (2020) 4098. <https://doi.org/10.1038/s41467-020-17941-8>.
- [180] D. Xie, R. Dittmeyer, Correlations of laser scanning parameters and porous structure properties of permeable materials made by laser-beam powder-bed

- fusion, *Additive Manufacturing* (2021) 102261.  
<https://doi.org/10.1016/j.addma.2021.102261>.
- [181] J. Suryawanshi, K.G. Prashanth, U. Ramamurty, Mechanical behavior of selective laser melted 316L stainless steel, *Materials Science and Engineering: A* 696 (2017) 113–121. <https://doi.org/10.1016/j.msea.2017.04.058>.
- [182] J. Yu, X. Hu, Y. Huang, A modification of the bubble-point method to determine the pore-mouth size distribution of porous materials, *Separation and Purification Technology* 70 (2010) 314–319.  
<https://doi.org/10.1016/j.seppur.2009.10.013>.
- [183] I.G. Wenten, K. Khoiruddin, A.N. Hakim, N.F. Himma, The Bubble Gas Transport Method, in: N. Hilal, A.F. Ismail, T. Matsuura, D. Oatley-Radcliffe (Eds.), *Membrane characterization*, Elsevier, Amsterdam, 2017, pp. 199–218.
- [184] I. Yadroitsev, A. Gusarov, I. Yadroitsava, I. Smurov, Single track formation in selective laser melting of metal powders, *Journal of Materials Processing Technology* 210 (2010) 1624–1631.  
<https://doi.org/10.1016/j.jmatprotec.2010.05.010>.
- [185] J.P. Kruth, L. Froyen, J. van Vaerenbergh, P. Mercelis, M. Rombouts, B. Lauwers, Selective laser melting of iron-based powder, *Journal of Materials Processing Technology* 149 (2004) 616–622.  
<https://doi.org/10.1016/j.jmatprotec.2003.11.051>.
- [186] P. Kant, Palladiumkompositmembranen durch Suspensionsplas-maspritzten auf planaren Substraten und deren Integration in kompakte Membranreaktoren, Master Thesis, Karlsruher Institut für Technology (2017).
- [187] P. Lenormand, D. Caravaca, C. Laberty-Robert, F. Ansart, Thick films of YSZ electrolytes by dip-coating process, *Journal of the European Ceramic Society* 25 (2005) 2643–2646. <https://doi.org/10.1016/j.jeurceramsoc.2005.03.212>.
- [188] L. van Belle, G. Vansteenkiste, J.C. Boyer, Investigation of Residual Stresses Induced during the Selective Laser Melting Process, *The Current State-of-the-Art on Material Forming* 554-557 (2013) 1828–1834.  
<https://doi.org/10.4028/www.scientific.net/KEM.554-557.1828>.
- [189] A. Wunsch, P. Kant, M. Mohr, K. Haas-Santo, P. Pfeifer, R. Dittmeyer, Recent Developments in Compact Membrane Reactors with Hydrogen Separation, *Membranes (Basel)* 8 (2018). <https://doi.org/10.3390/membranes8040107>.
- [190] J.D. Holladay, Y. Wang, E. Jones, Review of developments in portable hydrogen production using microreactor technology, *Chem. Rev.* 104 (2004)

- 4767–4789. <https://doi.org/10.1021/cr020721b>.
- [191] Y. Liu, Y. Yang, Di Wang, A study on the residual stress during selective laser melting (SLM) of metallic powder, *Int J Adv Manuf Technol* 87 (2016) 647–656. <https://doi.org/10.1007/s00170-016-8466-y>.
- [192] Di Wang, Y. Yang, Z. Yi, X. Su, Research on the fabricating quality optimization of the overhanging surface in SLM process, *Int J Adv Manuf Technol* 65 (2013) 1471–1484. <https://doi.org/10.1007/s00170-012-4271-4>.
- [193] G. Straczewski, J. Völler-Blumenroth, H. Beyer, P. Pfeifer, M. Steffen, I. Felden, A. Heinzl, M. Wessling, R. Dittmeyer, Development of thin palladium membranes supported on large porous 310L tubes for a steam reformer operated with gas-to-liquid fuel, *Chemical Engineering and Processing: Process Intensification* 81 (2014) 13–23. <https://doi.org/10.1016/j.cep.2014.04.002>.
- [194] J. Tong, L. Su, Y. Kashima, R. Shirai, H. Suda, Y. Matsumura, Simultaneously Depositing Pd–Ag Thin Membrane on Asymmetric Porous Stainless Steel Tube and Application To Produce Hydrogen from Steam Reforming of Methane, *Ind. Eng. Chem. Res.* 45 (2006) 648–655. <https://doi.org/10.1021/ie050935u>.
- [195] X. Yao, Y. Zhang, L. Du, J. Liu, J. Yao, Review of the applications of microreactors, *Renewable and Sustainable Energy Reviews* 47 (2015) 519–539. <https://doi.org/10.1016/j.rser.2015.03.078>.
- [196] T. Zheng, W. Zhou, D. Geng, Y. Li, Y. Liu, C. Zhang, Methanol steam reforming microreactor with novel 3D-Printed porous stainless steel support as catalyst support, *International Journal of Hydrogen Energy* 45 (2020) 14006–14016. <https://doi.org/10.1016/j.ijhydene.2020.03.103>.
- [197] G. Scotti, S.M.E. Nilsson, M. Haapala, P. Pöhö, G. Boije af Gennäs, J. Yli-Kauhaluoma, T. Kotiaho, A miniaturised 3D printed polypropylene reactor for online reaction analysis by mass spectrometry, *React. Chem. Eng.* 2 (2017) 299–303. <https://doi.org/10.1039/C7RE00015D>.
- [198] F. Kazenwadel, E. Biegert, J. Wohlgemuth, H. Wagner, M. Franzreb, A 3D-printed modular reactor setup including temperature and pH control for the compartmentalized implementation of enzyme cascades, *Eng. Life Sci.* 16 (2016) 560–567. <https://doi.org/10.1002/elsc.201600007>.
- [199] J.G. Fatou, Melting temperature and enthalpy of isotactic polypropylene, *European Polymer Journal* 7 (1971) 1057–1064. [https://doi.org/10.1016/0014-3057\(71\)90138-8](https://doi.org/10.1016/0014-3057(71)90138-8).
- [200] S. Heinrich, F. Edeling, C. Liebner, H. Hieronymus, T. Lange, E. Klemm,

Catalyst as ignition source of an explosion inside a microreactor, *Chemical Engineering Science* 84 (2012) 540–543.

<https://doi.org/10.1016/j.ces.2012.08.049>.

- [201] W. Shi, P. Wang, Y. Liu, G. Han, Experiment of Process Strategy of Selective Laser Melting Forming Metal Nonhorizontal Overhanging Structure, *Metals* 9 (2019) 385. <https://doi.org/10.3390/met9040385>.

# Appendix

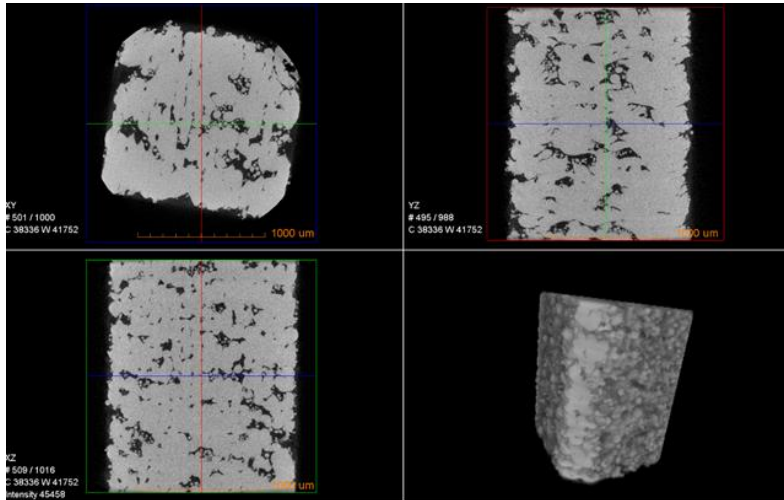


Figure A.1  $\mu$ -CT of sample printed by unidirectional vectors.

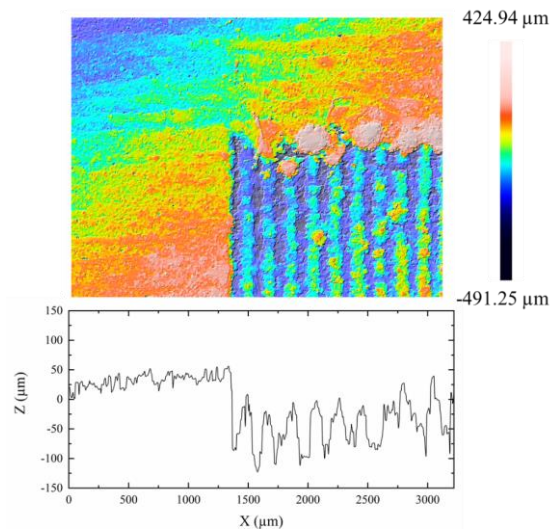


Figure A.2. Surface geometry of samples before hatch offset optimization

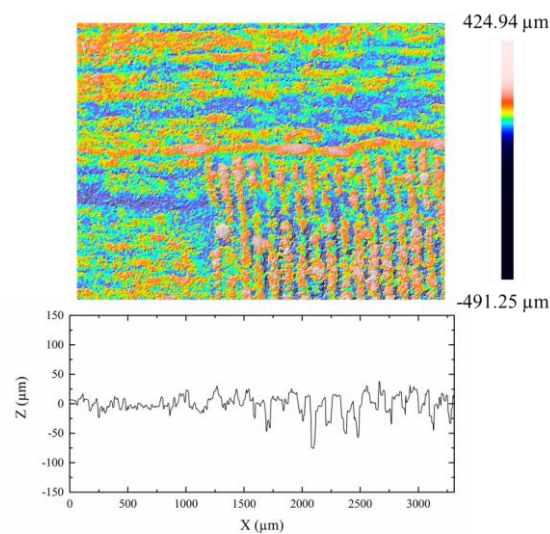


Figure A.3. Surface geometry of samples after hatch offset optimization



Figure A. 4. Samples with internal channels printed by porous-dense composite.

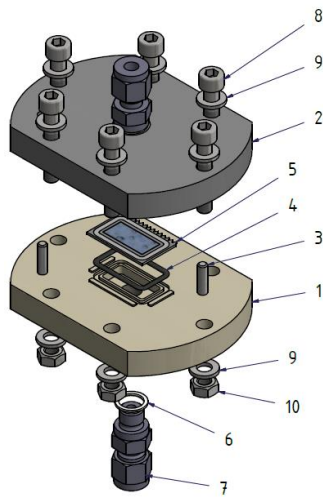


Figure A. 5. Schematic of flow cell fabricated in IMVT.

Part	Piece	designation	Standard abbreviation
1	1	Adapterplatte 1	
2	1	Adapterplatte 2	
3	2	Zylinderstift	$\Phi$ 4 m6 x 20
4	2	O-Ring	$\Phi$ 25 x 1.5
5	1	Poröses Substrat	
6	2	Dichtring	304L-2-RSNB-2
7	2	Einschraubverschraubung	SS-6M0-1-2RS
8	6	Zylinderkopfschraube	DIN 912 - M6 x 35
9	12	Unterlegscheibe	DIN 125-2 - B 6.4
10	6	Sechskantmutter	DIN 934 - M6

# List of figures

Figure. 1.1. Fabrication technologies of macro porous metals [20].	3
Figure. 1.2. Schematic of foaming by gas injection [24].	4
Figure. 1.3. Schematic of an apparatus for fabrication of gasars [31].	5
Figure. 1.4 Porous sintered metals based on a sacrificial template [36].	6
Figure. 1.5. Illustration of the space holder process to fabricate porous metals [36].	7
Figure. 1.6. Classification of additive manufacturing processes [48].	7
Figure 1.7. (a) Implants printed by LB-PBF; (b) Micro CT assessment of the implant [89].	9
Figure 1.8. Die-casting dies with conformal cooling channels manufactured by a LB-PBF printer and a CNC machine [94].	10
Figure 1.9. Optical microscopy graphs and pore size distribution of breathable steel [96].	12
Figure 1.10. Application fields of porous metals in the automotive industry [20].	13
Figure 1.11. Reactor manufactured for methanation of CO/CO <sub>2</sub> mixtures [124].	15
Figure 1.12. Schematic of binder jetting process [17].	16
Figure 1.13. Schematic of the SLS/SLM process [139].	18
Figure 1.14. Schematic of powder-based laser metal deposition [153].	18
Figure 1.15. (a) additively manufactured stainless steel porous electrode after nickel coating; (b) Side view of the electrode; (c) micrograph of the pore structure; (d) nickel EDS mapping of the electrode [177].	21
Figure 1.16. 3D printed self catalytic reactors (SCR) for Fischer–Tropsch (FT) synthesis, CO <sub>2</sub> hydrogenation, and dry reforming of CH <sub>4</sub> (DRM) [179].	22
Figure 2.1. Basic scanning parameters. Coordinates refer to the printer’s coordinate system. Figure reproduced from Ref. [180].	25
Figure 2.2. (a) Dense frame for porosity measurements; (b) Permeable-dense composite sample for permeability and porosity measurements; (c) Disk-shaped permeable sample for pore size distribution measurements; (d) Schematic of Permeable-dense composite sample; (e) Schematic of disk-shaped permeable sample for pore size distribution. Figure reproduced from Ref. [180].	28
Figure 2.3. Flow cell system for permeability measurements. Figure reproduced from Ref. [180].	29
Figure 2.4. Schematic of rotation scan vectors. Coordinates refer to the printer’s coordinate system.	30
Figure 2.5. SEM micrographs of the front surface for different rotation of the scan vectors per layer: (a) Scan vectors rotate 12° each layer; (b) Scan vectors rotate 20° each layer; (c) Scan vectors rotate 30° each layer.	31
Figure 2.6. (a) Schematic of scan vectors shifting position between individual layers; (b) schematic of scan vectors always keeping the same position between individual layers.	31
Figure 2.7. SEM micrographs of the front surface with and without shifting of the	

scan vectors in alternating layers: (a) Scan vectors shifting position between alternating layers; (b) Scan vectors keep the same position for all layers..... 32

Figure 2.8. (a) Schematic of unidirectional scan vectors in X direction; (b) Schematic of unidirectional scan vectors in Y direction. .... 32

Figure 2.9. (a) Front surface of a sample produced by unidirectional scan vectors in Y direction with 50  $\mu\text{m}$  laser spot diameter; (b) The front surface of a sample produced by unidirectional scan vectors in X direction with 50  $\mu\text{m}$  laser spot diameter..... 33

Figure 2.10.  $\mu$ -CT scan model of a sample printed with unidirectional scan vectors with 50  $\mu\text{m}$  laser spot diameter. Note that the front of the sample produced by unidirectional scan vectors in X direction shown in Fig. 2.9 (b) is the same face as the left (or right) side of sample produced by unidirectional scan vectors in Y direction shown in Fig. 2.9 (a). .... 34

Figure 2.11(a) Front surface of a sample produced by unidirectional scan vectors in X direction with 30  $\mu\text{m}$  laser spot diameter; (b) Front surface of a sample produced by unidirectional scan vectors in Y direction with 30  $\mu\text{m}$  laser spot diameter. ... 34

Figure 2.12 (a) Front surface of hatch distance 0.1 mm specimen; (b) Back surface of hatch distance 0.1 mm specimen; (c) Front surface of hatch distance 0.15 mm specimen; (d) Back surface of hatch distance 0.15 mm specimen; (e) Front surface of hatch distance 0.2 mm specimen; (f) Back surface of hatch distance 0.2 mm specimen. .... 35

Figure 2.13. (a) T-50 before sand blasting; (b) T-50 after sand blasting..... 36

Figure 2.14. (a) Front surface of sample printed by laser spot size 30  $\mu\text{m}$ ; (b) Front surface of sample printed by laser spot size 40  $\mu\text{m}$ ; (c) Front surface of sample printed by laser spot size 50  $\mu\text{m}$ ; (d) Front surface of sample printed by laser spot size 60  $\mu\text{m}$ . .... 37

Figure. 2.15. (a) Permeation testing of samples produced with different laser spot size; (b) Pore size distribution of samples with different laser spot size. .... 38

Figure. 2.16. SEM micrograph of the front surface of a sample produced by unidirectional scan vectors arranged alternately opposite. .... 39

Figure. 2.17. (a) Pressure drop during permeation testing of T-A and T-50; Fig. 2.17 (b) Pore size distribution of T-A and T-50 ..... 40

Figure 2.18. (a)(b)(c)(d)(e)(f) Front surface of sample printed by hatch distance 0.1 mm, 0.11mm, 0.12mm, 0.13mm, 0.14mm, 0.15mm; ..... 42

Figure. 2.19. (a) Permeability of samples printed by different hatch distance; (b) Pore size distribution of samples printed by different hatch distance. .... 43

Figure 2.20. (a) additively manufactured KIT logo; (b) additively manufactured QR code ..... 44

Figure 2.21. Schematic of a permeable material with different pore size on different surfaces..... 45

Figure 2.22. Surfaces of a sample printed with different hatch distance. (a) Front surface printed with 0.13 mm hatch distance; (b) Back surface printed with 0.09 mm hatch distance; (c) Cross section of the sample..... 45

Figure 3.1. Scanning parameters of tubular samples. .... 48

Figure 3.2. Schematic of permeable tubes printed by USV.....	48
Figure 3.3. (a) Left surface of a permeable tube printed by USV; (b) Front surface of a permeable tube printed by USV.....	49
Figure 3.4. Different surfaces of a tubular sample printed by USV. (a) Front surface; (b) Back surface; (c) Left surface ; (d) Right surface.....	50
Figure 3.5. Schematic of permeable tube printed by RSV.....	51
Figure 3.6. Permeable tube printed by 10° RSV; (b) 3D profile of a permeable tube printed by 10° RSV.....	52
Figure 3.7. (a) Front, (b) back, (c) left, and (d) right surface of a tube printed by 10° RSV.....	53
Figure 3.8. Permeable tubes printed by (a) 12° RSV, (b) 20° RSV, (c) 30° RSV, and (d) 60° RSV.....	54
Figure 3.9. (a) Micrographs of permeable tubes printed by 12° RSV, (b) 20° RSV, (c) 30° RSV, and (d) 60° RSV.....	55
Figure 3.10. (a) Schematic of a permeable tube printed by FDSV; (b) Schematic of a permeable tube printed by FDCSV; (c) Schematic of a permeable tube printed by FDOSV.....	56
Figure 3.11. (a) Permeable tube printed by FDSV; (b) Gap between scan vectors in different direction.....	57
Figure 3.12. (a) Permeable tube printed by FDCSV; (b) 3D profile of the groove on the surface of the permeable tube.....	58
Figure 3.13. (a) Permeable tube printed by FDOSV; (b) 3D profile of a permeable tube printed by FDOSV.....	59
Figure 3.14. Front surface of curved permeable samples printed by different hatch distance; (a) 0.1 mm; (b) 0.11 mm; (c) 0.12 mm; (d) 0.13 mm; (e) 0.14 mm; (f) 0.15 mm.....	60
Figure 3.15. Front surface of curved permeable samples printed by different laser spot size; (a) 30 μm; (b) 40 μm; (c) 50 μm; (d) 60 μm.....	61
Figure 3.16. Different diameter permeable-dense tubular samples printed by FDOSV; (b) Different thickness permeable tube printed by FDOSV.....	63
Figure 4.1. Geometry of the test specimen. Dimensions are given in mm.....	65
Figure 4.2. (a) Conventional test specimen; (b) Additively manufactured test specimen.....	66
Figure 4.3. Connection area of porous substrate and dense frame in a conventional test specimen.....	66
Figure 4.4. Connection area of permeable and dense structures of an additively manufactured test specimen.....	67
Figure 4.5. Additively manufactured test specimen after dip coating.....	68
Figure 4.6. (a) Conventional test specimen before ceramic coating; (b) Additively manufactured test specimen before ceramic coating; (c) Conventional test specimen after ceramic coating; (d) Additively manufactured test specimen after ceramic coating.....	70
Figure 4.7. (a) Additively manufactured test specimen before (a) and after (b) smoothing treatment.....	70

Figure. 4.8. 3D profile of test module after smooth treatment. ....	71
Figure 4.9. Schematic of the PMS plate.....	72
Figure 4.10. The printing job of a PMS plate in the ReaLizer SLM125 operating system.....	73
Figure 4.11. Additively manufactured 2 mm thick PMS plate created with the same laser parameters and scan strategy like the test specimen in figure 4.2. ....	74
Figure 4.12. Additively manufactured 5 mm thick PMS plate. ....	74
Figure 4.13. 3D profile of an additively manufactured 5 mm thick PMS plate. ....	75
Figure 4.14. Schematic of a 3 mm thick PMS plate after geometry optimization.....	76
Figure 4.15. The printing job of the dense frame for the 3 mm thick PMS plate after geometry optimization in the ReaLizer SLM125 operating system. ....	77
Figure 4.16. (a) 3 mm thick PMS plate after geometry optimization; (b) Internal channels of the PMS plate; (c) Back side of the PMS plate. ....	78
Figure 4.17. 3D profile of a 3 mm thick PMS plate after structure optimization. ....	79
Figure 4.18. Schematic of different tubular palladium membrane substrates. ....	80
Figure 4.19. PMS pipes printed by 60° RSV. ....	81
Figure 4.20. 3D profile of PMS pipe printed by 60° RSV.....	81
Figure 4.21. PMS pipes printed by FDCSV.....	82
Figure 4.22. 3D profile of a PMS pipe printed by FDCSV. ....	83
Figure 4.23. Schematic of an additively manufactured microchannel plate.....	84
Figure 4.24. Additively manufactured plate with microchannels.....	84
Figure 4.25. 3D profile of the additively manufactured microchannel plate.....	85
Figure 4.26. Additively manufactured plate with porous microchannels. ....	86
Figure 4.27. 3D profile of the additively manufactured porous microchannel.....	86
Figure 4.28. Schematic of an additively manufactured test reactor.....	88
Figure 4.29. Temperature barrier test reactor printed by 45° printing strategy. ....	89
Figure 4.30. 3D profile of a thermocouple hole in the additively manufactured reactor. ....	89
Figure 4.31. Additively manufactured temperature barrier test reactor with microchannel plate. ....	90
Figure 4.32. Schematic of an additively manufactured reactor for methane steaming reforming.....	90
Figure 4.33. Additively manufactured reactor for steam reforming.....	91
Figure A.1 $\mu$ -CT of sample printed by unidirectional vectors.....	114
Figure A.2. Surface geometry of samples before hatch offset optimization .....	114
Figure A.3. Surface geometry of samples after hatch offset optimization .....	114
Figure A. 4. Samples with internal channels printed by porous-dense composite... ..	115
Figure A. 5. Schematic of flow cell fabricated in IMVT.....	115

## List of tables

Table 1.1 Properties and applications of porous metals [36].....	8
Table. 1.2 Classification of metal additive manufacturing methods [102].....	14
Table. 1.3 Comparisons of different metal additive manufacturing methods [102]...	19
Table. 1.4 Typical methods/processes in micro-manufacturing [168].....	20
Table. 2.1. Roughness, porosity, permeability and calculated permeability of samples with different laser spot size .....	38
Table. 2.2. Roughness and porosity of samples made by unidirectional scan vectors arranged alternately opposite and unidirectional scan vectors arranged in the same direction.....	41
Table 2.3. Roughness, porosity and permeability of samples with different hatch distance.....	44
Table. 3.1. Roughness of different surfaces of permeable tubes printed by USV.....	50
Table 3.2. Surface roughness at different sides of a permeable tube printed by 10° RSV.....	53
Table. 3.3. The porosity and roughness of permeable tubes printed by different angle of RSV.....	55
Table 3.4. Roughness of different surfaces of a permeable tube printed by four direction overlap vectors.....	59
Table 3.5. Porosity of permeable tubes printed by different hatch distance.....	61
Table. 3.6. Porosity of permeable tubes printed by different laser spot size. ....	62
Table 4.1 Mass of components for the dip coating slurry.....	68
Table. 4.2 Parameters of the dip coating.....	69

# DongxuXie (谢东序)

Karlsruhe Institute of Technology | (+49)015226294044 | dongxu.xie@kit.edu

## Education

---

2017.10-                    **Karlsruhe Institute of Technology**                    **Chemical and Process Engineering**

- Ph.D in Institute for Micro Process Engineering (IMVT) of KIT
- 

2015.9-2017.7            **Harbin Institute of Technology**                    **Material Processing Engineering**

- Master Degree in Material Processing Engineering
- 

2011.9-2015.7            **Harbin Engineering University**                    **Materials Physics**

- Bachelor Degree in Materials Physics
- 

## Project Experiences

---

2017.10-                    **Additively manufactured permeable-dense composites and its applications in microstructured reactors**                    **Ph.D Project**

- The Correlations of laser scanning parameters and porous structure properties of permeable materials made by laser-beam powder-bed fusion was systematically studied
  - A permeable-dense metallic material was developed by laser-beam powder-bed fusion as a new material for palladium membrane substrate
- 

2015.9-2017.7                    **An investigation of hydrogen permeability and the crystal lattice size of V-Ni-Mo-Pd alloys**                    **Master Project**

- Adding alloy elements into vanadium to reduce the solubility of vanadium alloy, at the same time controlling the lattice size of vanadium; Measuring the hydrogen permeability of V alloys
  - Research the relationship between the permeability of V alloys and the size of crystal lattice
-